Aalborg Universitet

Characterization and Diagnostics for Photovoltaic Modules and Arrays

Spataru, Sergiu

Publication date:
2015

Document Version
Publisher's PDF, also known as Version of record

Link to publication from Aalborg University

Citation for published version (APA):
Spataru, S. (2015). *Characterization and Diagnostics for Photovoltaic Modules and Arrays*. Department of Energy Technology, Aalborg University.

General rights
Copyright and moral rights for the publications made accessible in the public portal are retained by the authors and/or other copyright owners and it is a condition of accessing publications that users recognise and abide by the legal requirements associated with these rights.

- Users may download and print one copy of any publication from the public portal for the purpose of private study or research.
- You may not further distribute the material or use it for any profit-making activity or commercial gain
- You may freely distribute the URL identifying the publication in the public portal -

Take down policy
If you believe that this document breaches copyright please contact us at vbn@aub.aau.dk providing details, and we will remove access to the work immediately and investigate your claim.

Downloaded from vbn.aau.dk on: April 19, 2024

CHARACTERIZATION AND DIAGNOSTICS FOR PHOTOVOLTAIC MODULES AND ARRAYS

by

Sergiu Viorel Spătaru

Department of Energy Technology

DEPARTMENT OF ENERGY TECHNOLOGY
AALBORG UNIVERSITY

Dissertation Submitted to
The Faculty of Engineering and Science, Aalborg University in Partial
Fulfilment for the Degree of Doctor of Philosophy

February 2015
Aalborg, Denmark

Thesis submitted:	February 2, 2015
PhD supervisor:	Associate Prof. Dezső Séra, Aalborg University
Assistant PhD supervisors:	Associate Prof. Tamas Kerekes, Aalborg University Prof. Remus Teodorescu, Aalborg University
PhD committee:	Prof. Ernest van Dyk, Nelson Mandela Metropolitan University PhD. Chris Deline, National Renewable Energy Laboratory Prof. Josep M. Guerrero, Aalborg University

PhD Series: Faculty of Engineering and Science, Aalborg University

Published by:
Aalborg University Press
Skjernvej 4A, 2nd floor
DK – 9220 Aalborg Ø
Phone: +45 99407140
aauf@forlag.aau.dk
forlag.aau.dk

© Copyright by author
Printed in Denmark by Rosendahls, 2016

Thesis title: Characterization and Diagnostics for Photovoltaic Modules and Arrays

PhD student: Sergiu Viorel Spătaru

Supervisors: Associate professor Dezső Séra

Professor Remus Teodorescu

Associate professor Tamas Kerekes

List of published papers:

1. S. Spataru, P. Hacke, D. Sera, C. Packard, T. Kerekes and R. Teodorescu. "Temperature-Dependency Analysis and Correction Methods of in-Situ Power-Loss Estimation for Crystalline Silicon Modules Undergoing Potential-Induced Degradation Stress Testing." Progress in Photovoltaics: Research and Applications 23, no. 11 (2015): pp. 1536--1549. DOI: 10.1002/pip.2587.
2. P. Hacke and S. Spataru. "Automated Data Collection for Determining Statistical Distributions of Module Power Undergoing Potential-Induced Degradation." Presented at *24th Workshop on Crystalline Silicon Solar Cells & Modules: Materials and Processes*, Breckenridge, Colorado, United States, 2014.
3. S. Spataru, D. Sera, T. Kerekes, R. Teodorescu, P. A. Cotfas and D. T. Cotfas. "Experiment Based Teaching of Solar Cell Operation and Characterization Using the Solarlab Platform." In proc. of *Proceedings of the 7th International Workshop on Teaching in Photovoltaics*, vol. 7, 2014.
4. S. Spataru, D. Sera, T. Kerekes and R. Teodorescu. "Teaching Photovoltaic Array Modelling and Characterization Using a Graphical User Interface and a Flash Solar Simulator." In proc. of *Proceedings of the 6th International Workshop on Teaching in Photovoltaics*, vol. 6, pp. 36-44, 2012.
5. S. Spataru, P. Cernek and D. Sera. "Characterization of a Crystalline Silicon Photovoltaic System after 15 Years of Operation in Northern Denmark." In proc. of *29th European Photovoltaic Solar Energy Conference and Exhibition*, pp. 2680 - 2688, 2014, DOI: 10.4229/EUPVSEC20142014-5BV.1.31.
6. S. Spataru, D. Sera, P. Hacke, T. Kerekes and R. Teodorescu. "Fault Identification in Crystalline Silicon PV Modules by Complementary Analysis of the Light and Dark Current-Voltage Characteristics." *Progress in Photovoltaics: Research and Applications*, 2015, DOI: 10.1002/pip.2571.
7. C. Kopacz, S. Spataru, D. Sera and T. Kerekes. "Remote and Centralized Monitoring of PV Power Plants." In proc. of *Optimization of Electrical and Electronic Equipment (OPTIM), 2014 International Conference on*, pp. 721-728, 2014, DOI: 10.1109/OPTIM.2014.6851005.
8. S. Spataru, D. Sera, T. Kerekes and T. Teodorescu. "Photovoltaic Array Condition Monitoring Based on Online Regression of Performance

Model." In proc. of *39th IEEE Photovoltaic Specialists Conference* pp. 0815 - 0820, 2013, DOI: 10.1109/PVSC.2013.6744271.

9. D. Sera, S. Spataru, L. Mathe, T. Kerekes and R. Teodorescu. "Sensorless PV Array Diagnostic Method for Residential PV Systems." In proc. of *26th European Photovoltaic Solar Energy Conference and Exhibition*, pp. 3776 - 3782, 2011, DOI: 10.4229/26thEUPVSEC2011-4AV.3.37.
10. S. Spataru, D. Sera, T. Kerekes and R. Teodorescu. "Detection of Increased Series Losses in PV Arrays Using Fuzzy Inference Systems." In proc. of *Photovoltaic Specialists Conference (PVSC), 2012 38th IEEE*, pp. 464-469, 2012, DOI: 10.1109/PVSC.2012.6317658.
11. S. Spataru, D. Sera, T. Kerekes and R. Teodorescu. "Diagnostic Method for Photovoltaic Systems Based on Light I-V Measurements." Solar Energy 119, (2015): pp. 29-44. DOI: 10.1016/j.solener.2015.06.020.
12. S. Spataru, A. Amoiridis, R. N. Beres, C. I. Ciontea, T. Klein and D. Sera. "Development of an Intelligent Maximum Power Point Tracker Using an Advanced PV System Test Platform." In proc. of *Photovoltaic Specialists Conference (PVSC), 2013 IEEE 39th*, pp. 2953-2958, 2013, DOI: 10.1109/PVSC.2013.6745084.

This present report combined with the above listed scientific papers has been submitted for assessment in partial fulfilment of the PhD degree. The scientific papers are not included in this version due to copyright issues. Detailed publication information is provided above and the interested reader is referred to the original published papers. As part of the assessment, co-author statements have been made available to the assessment committee and are also available at the Faculty of Engineering and Science, Aalborg University.

ENGLISH SUMMARY

Photovoltaic energy has become one of the most important renewable energy technologies, reaching a global cumulative installed capacity of about 139 GW at the end of 2013, and at least 174 GW forecasted by the end of 2014 by EPIA. This exponential growth was possible due to favorable policies, as well as decreasing cost of PV modules and balance-of-system components. As these main market drivers reach their limit, the system operating costs and long-term reliability of the PV modules becomes more relevant in reducing the total lifetime cost of the PV system. In this context, characterization and diagnostic methods are increasingly important in identifying and understanding the failures and degradation modes affecting PV modules and arrays, as well as developing relevant tools and tests for assessing the reliability and lifetime of PV modules.

This thesis investigates diagnostic methods for characterizing and detecting degradation modes in crystalline silicon photovoltaic modules and arrays, and is structured into two parts. The first part of this work is focused on developing PV module characterization and diagnostic methods for use in module diagnostics and failure identification, accelerated stress testing, and degradation studies. The second part of this work investigates diagnostic methods for PV arrays that are suitable for implementation in the solar inverter or incorporated in a condition monitoring system.

The PV module diagnostic methods investigated in the first part of this work were developed based on two well-known module characterization techniques, namely current-voltage (I-V) characterization, and electroluminescence imaging.

The I-V based module diagnostic method was developed by combining the strengths of light I-V and dark I-V characterization, for the purpose of identifying degradation modes such as: (i) optical losses; (ii) cell cracks and breaks; (iii) degradation of the external circuit of the PV module; and (iv) potential-induced degradation (PID). This method, which is machine analysis friendly, can identify incipient degradation in modules, which would otherwise be difficult to detect from light I-V measurements alone. The method can be used as a laboratory diagnostic tool, and can also be implemented in future field applications, for example in: (i) in I-V tracers for PV degradation studies; (ii) or as a diagnostic function in module-integrated converters.

A similar approach was used in developing an in-situ power loss estimation method for modules undergoing PID stress testing. This method implies semi-continuous dark I-V characterization of the PV modules under test, at an elevated stress temperature, without interrupting the test. The dark I-V curves are then used to determine the degradation of the module's maximum power, at standard testing conditions (STC 1000 W/m^2 25°C), as a function of time and stress level. This leads

to reduced test duration and cost, avoids stress transients while ramping to and from the stress temperature, eliminates flash testing except at the initial and final data points, and enables significantly faster and more detailed acquisition of statistical data for future application of various statistical reliability models.

The second PV module diagnostic technique investigated is electroluminescence (EL) imaging. EL Imaging is an excellent tool for visually (qualitatively) identifying different types of failures and degradation in PV modules, however, currently there is no standard methodology to quantify them. In this study a method was developed for quantifying the extent of different failures and degradation modes present in crystalline silicon PV modules from EL images. The method relies on identifying specific failure signatures in EL images, by analyzing the luminescence maps and distributions. The method is suitable for automatic analysis and assessment of module quality from EL images, for the purpose of PV module diagnostics and module quality inter-comparison.

The second part of this work was focused on developing diagnostic methods for detecting failures and degradation occurring in PV arrays. This research resulted in two types of diagnostic methods that can be implemented in a PV system, depending on the hardware available.

The first PV array diagnostic method proposed uses a model-based approach, and is suitable for PV systems where irradiance and module temperature sensors are available. The method is based on estimating the power output of the PV generator from in-plane irradiance and module temperature measurements, and using a performance model of the PV array. The novelty of the method comes from its ability to (automatically) self-parameterize the performance model from measurements acquired by the PV inverter after the PV system has been commissioned, and does not require a dedicated system modelling step.

The second type of PV array diagnostic method investigated can operate without ambient sensors, and is based on measuring and analyzing parameters of the light I-V curve of the array. In comparison with yield measurements, I-V curves can provide much more information regarding the condition and electrical properties of the PV array, such as: short-circuit current, open-circuit voltage, fill factor, series and shunt resistance, ideality factor, as well as indicate the presence of shading and soiling. Considering this, the diagnostic method proposes to calculate certain diagnostic parameters from the PV array I-V curve, which can indicate the presence of shading, increased series-resistance losses, or PID. These parameters were then used to design a fault detection algorithm, based on fuzzy inference systems that can be implemented in the PV inverter controller. Experimental results show that the I-V based diagnostic method performs well in identifying both shading and increased series-resistance losses affecting PV arrays. The method requires low computation resources and it uses hardware capabilities that are already present in most PV inverters.

DANSK RESUMÉ

Solcelleenergi er blevet en af de vigtigste teknologier for vedvarende energi og nåede en global akkumuleret installeret kapacitet på omkring 139 GW ved udgangen af 2013 med en forventning om at nå 174 GW ved udgangen af 2014 ifølge EPIA. Denne eksponentielle vækst var mulig på grund af gunstig politik, faldende udgifter til fotovoltaiske moduler og BOS komponenter. Når disse primære markeds drivere når deres grænse så bliver systemets driftsomkostninger samt modulernes langsigtet pålidelighed mere relevant at reducere i forhold til at sænke de samlede levetidsomkostninger for solcelleanlægget. I denne kontekst er karakteriserings og diagnostistiserings metoder vigtige for at identificere og forstå hvordan fejl og nedbrydning påvirker solcelleanlægget, samt udvikling af relevante værktøjer og tests til at vurdere pålidelighed og levetid fotovoltaiske moduler.

Denne afhandling undersøger diagnostiske metoder til karakterisering og detektering af nedbrydning i krystallinsk silicium solcelleanlæg. Afhandlingen er struktureret i to dele, hvor den første del er fokuseret på at udvikle karakteriserings- og diagnosticeringsmetoder til diagnostik af moduler og fejl identifikation, accelereret stresstest samt nedbrydnings studier. Anden del undersøger diagnostiske metoder til solcelleanlæg, der er egnet til implementering i inverteren eller indgår i et overvågningssystem.

Modul diagnosticeringsmetoder undersøgt i første del blev udviklet baseret på to velkendte modul karakterisering teknikker, strøm-spænding (I-V) karakterisering og electroluminescence imaging.

Den I-V baserede modul diagnostiske metode blev udviklet ved at kombinere styrkerne i lys I-V og mørk I-V karakterisering med henblik på at identificere nedbrydnings tilstande såsom: (i) optiske tab; (ii) celle revner og brud; (iii) nedbrydning af modulets ydre kredsløb; (iv) potentiel-induceret degradation (PID). Denne metode er egnet til maskinanalyse og kan identificere begyndende nedbrydning i moduler, som ellers ville være svært at opdage ved kun at bruge lys I-V målinger. Metoden kan bruges som et laboratorisk diagnostisk værktøj men kan også implementeres i fremtidige applikationer, for eksempel i: (i) i I-V sporstoffer for fotovoltaiske nedbrydnings undersøgelser; (ii) eller som en diagnostisk funktion i modul-integrerede omformere.

En lignende fremgangsmåde blev anvendt i udviklingen af en in-situ strømsvigts estimerings metode til moduler der gennemgår PID stresstest. Denne metode gør brug af semi kontinuerlig mørk IV karakterisering af modulerne under test ved en forhøjet stress temperatur uden at afbryde testen. Derefter anvendes de mørke I-V kurver til at bestemme nedbrydningen af modulets maksimale effekt, ved standardprøvningsbetingelser (STC 1000 W/m^2 25°C), som en funktion af tid og

stressniveau. Dette giver en begrænset test varighed og pris, undgår at stresse modulerne og introducere fejl ved temperaturændringer, fjerner flash test på nær de indledende og afsluttende datapunkter, samt betydeligt hurtigere og mere detaljeret erhvervelse af statistiske data til fremtidig anvendelse af forskellige statistiske pålideligheds modeller. Den anden modul diagnostiske teknik der undersøges er electroluminescence (EL) imaging. EL Imaging er et fremragende værktøj til visuel (kvalitativt) identifikation af forskellige fejltyper og nedbrydning af moduler, men i øjeblikket er der ingen standardmetode til at kvantificere dem. I denne undersøgelse er en metode blevet udviklet til kvantificering i et omfang af forskellige fejl og nedbrydnings tilstande til stede i krystallinsk silicium fotovoltaiske moduler fra EL billeder. Metoden bygger på at identificere specifikke fejl signaturer med at analysere EL billeder. Metoden er velegnet til automatisk analyse samt vurdering af modul kvalitet ud fra EL billeder med henblik på modul diagnostik og modul kvalitets inter-sammenligning.

Den anden del er fokuseret på at udvikle diagnostiske metoder til detektion af fejl og nedbrydnings forekommer i strenge. Denne forskning resulterede i to typer af diagnostiske metoder, der kan implementeres i et solcelleanlæg, afhængigt af hvilken hardware der er til rådighed.

Den første diagnostiske metode anvender en model baseret tilgang og er velegnet til solcelleanlæg hvor irradians grænser og modul temperaturfølere er til rådighed. Fremgangsmåden er baseret på at estimere udgangseffekten af generatoren fra in-plane irradians grænser og modul temperaturmålinger, samt ved hjælp af en performance model af generatoren. Det nye ved metoden stammer fra dens evne til at (automatisk) selv at parametrisere performance modellen fra målinger fra inverteren i solcelleanlægget og kræver ikke en dedikeret system modellerings indsats.

Den anden diagnostiske metode der undersøges kan fungere uden sensorer. Metoden er baseret på at måle og analysere den lyse I-V kurve af strengene. Sammenlignet med udbytte målinger giver I-V kurver mere information om tilstande og de elektriske egenskaber af strengene, såsom: kortslutningsstrøm, tomgangsspænding, fyld faktor, serier og shunt modstand, idealitet faktor og angive tilstedeværelsen af skygger og tilsmudsning. I betragtning af dette blev det foreslået at beregne visse diagnostiske parametre fra I-V kurven, der kan indikere tilstedeværelsen af skygger, øgede tab serie-resistens eller PID. Disse parametre blev herefter brugt til at designe en fejl detekterings algoritme, baseret på fuzzy inferens systemer, der kan implementeres i fotovoltaiske inverter kontroller. Eksperimentelle resultater viser at den I-V baserede diagnostiske metode kan identificere både skygge og øget serie-resistens tab som påvirker strenge. Metoden kræver lave beregnings ressourcer og understøttes af hardware kapaciteter, der allerede er til stede i de fleste invertere.

ACKNOWLEDGMENTS

This PhD thesis was realized under the PSO Forskel research project PSO-10648, entitled Smart Photovoltaic Systems, supported by the Danish Government and Energinet.dk, and in collaboration with Danfoss Solar A/S and Gaia Solar A/S. Acknowledgments are given to the above-mentioned institutions.

The research project was carried out under the supervision of Associate Prof. Dezső Séra and co-supervision of Professor Remus Teodorescu, and Associate Prof. Tamás Kerekes from the Department of Energy Technology, Aalborg University. To whom I am deeply grateful for their professional support and guidance, as well as their positive and open-minded attitude, which inspired and helped me to succeed in this challenging life experience.

Also, I want to thank Søren Bækhøj Kjær and Dan Radu Lazăr, from Danfoss Solar A/S for their fruitful participation in the steering meetings and for their valuable and active support.

Moreover, I would like extend my gratitude to Peter Hacke, for the support and consideration he gave me during my study abroad period at the National Renewable Energy Laboratory in Golden, Colorado, USA.

A special thank you goes to all my colleagues at the Department of Energy Technology, and to my fellow PhD students, Daniel, Irina and Bogdan, for their professional discussions, advice and moral support, as well as to Rune, who helped me revise parts of the thesis.

A warm thank you goes to my friends from far away, Cătălin, Patricia, Ionică and Cosmin, for their friendship and support.

And the most important thank you goes to my parents Viorel and Mărioara for teaching me what is important in life. To whom I dedicate this work.

Aalborg, February 2015

Sergiu Viorel Spătaru

TABLE OF CONTENTS

English summary ... **i**
Dansk resumé ... **iii**
Acknowledgments ... **v**
Table of contents ... **vii**
List of figures ... **10**
List of tables ... **15**
Nomenclature ... **16**
Chapter 1 Introduction ... **19**
1.1 Background and project motivation ... 19
1.1.1 Current status of photovoltaic technology ... 19
1.1.2 Competitiveness of the photovoltaic market and outlook ... 20
1.2 Problem formulation ... 23
1.2.1 Overview of the degradation and failure modes investigated ... 23
1.2.2 Module reliability and durability testing for PID ... 28
1.2.3 Module characterization and diagnostic methods ... 30
1.2.4 Plant diagnostic methods and systems ... 34
1.3 Project objectives ... 36
1.4 Project limitations ... 36
1.5 Main contributions ... 36
1.6 Thesis outline ... 38
1.7 List of appended publications ... 39
1.8 Related publications ... 40
Chapter 2 Characterization of module power degradation for PID accelerated lifetime testing ... **43**
2.1 Introduction ... 43
2.2 In-situ characterization of module power degradation for PID accelerated stress testing ... 44
2.2.1 Methodology for in-situ characterization of module power degradation at 25 ºC ... 44
2.2.2 Proposed methodology for in-situ characterization of module power degradation at stress temperature ... 45
2.3 Accelerated life tests and modelling of crystalline silicon PV module undergoing PID ... 51
2.4 Summary and conclusions ... 55

Chapter 3 Module degradation and failure mode identification based on the light and dark I-V characteristics 57
3.1 Introduction 57
3.2 Proposed methodology for identifying degradation and failures in crystalline silicon PV modules 58
3.2.1 Separating optical losses from electrical degradation 59
3.2.2 Characterizing increased series resistance of the PV module 61
3.2.3 Characterizing increased shunting and recombination in the PV module 62
3.3 Experimental validation of the diagnostic parameters 64
3.3.1 Identifying degradation of the electrical circuit 64
3.3.2 Identifying solar cell cracks and breaks 66
3.3.3 Identifying potential-induced degradation 68
3.4 Summary and conclusions 70
Chapter 4 Module degradation and failure diagnosis using electroluminescence imaging 73
4.1 Introduction 73
4.2 Module-level ELI distribution analysis 74
4.3 Cell-level ELI distribution analysis 78
4.4 Quantifying module degradation and failures 81
4.4.1 Mechanical degradation of the solar cells 81
4.4.2 PID of the solar cells 85
4.4.3 Degradation of the cell interconnects 87
4.5 Summary and conclusions 88
Chapter 5 Diagnostic methods and systems for PV plants 91
5.1 Introduction 91
5.2 PV system monitoring platform 92
5.3 Fault detection based on performance modelling 93
5.3.1 Diagnostic method 93
5.3.2 Experimental validation 95
5.4 Fault detection based on I-V characterization 98
5.4.1 Diagnostic method 98
5.4.2 Detection performance 101
5.4.3 Experimental validation 102
5.5 Optimized MPPT operation using partial shading detection and I-V characterization 105
5.5.1 Diagnostic method 105

5.5.2 Experimental validation using the PV monitoring platform 106
5.6 Summary and conclusions 108
Chapter 6 Conclusions 111
6.1 Thesis summary 111
6.2 Future work 113
Bibliography 115
Appendix A 125
Appendix B 131
Appendix C 133

LIST OF FIGURES

Figure 1.1: Evolution of annual PV installations (GW) [3]. 19
Figure 1.2: PV market incentives and enablers for 2013 [3]..................................... 21
Figure 1.3: LCOE of renewable energy technologies and conventional power plants in USA (2014) [10] and Germany (2013) [2]... 21
Figure 1.4: Main cost factors for solar PV, with the some of the most important technology goals to be achieved in order to drive the cost down..................... 22
Figure 1.5: Typical causes for optical losses in fielded PV modules: a) EVA discoloration (reprinted from [16] with permission from IEEE); b) bubbles/delamination (reprinted from [15] with permission from Elsevier); c) front glass soiling (reprinted from [17] with permission from Elsevier); d)glass breakage (reprinted from [18] with permission from Elsevier)........................ 23
Figure 1.6: Example of corrosion in the busbars and interconnect ribbons observed in different modules (reprinted from [33] with permission from IEEE). 25
Figure 1.7: Example electroluminescence image of a multi-crystalline silicon PV module with cell cracks. Module power degraded down to 94.7% of the initial STC P_{max}.. 26
Figure 1.8: Schematic of a PV array connected to the grid by means of a transformerless inverter (redrawn from [63]).. 27
Figure 1.9: PV system affected by PID in Southern Europe (reprinted from [64] with permission from IEEE). Left picture shows no visual symptoms of PID, whereas the IR picture on the right shows heating due to power loss/shunting of the modules. 27
Figure 1.10: Example electroluminescence image of a mono-crystalline silicon PV module affected PID. Module power degraded down to 76.8% of the initial STC P_{max}.. 28
Figure 2.1: Fully automated experiment setup for performing damp-heat with system-voltage stress testing on PV modules.. 46
Figure 2.2: Chamber temperature and relative humidity profiles for performing damp-heat (60ºC/85% RH) with system voltage stress testing (-1000 V). At the start and end of each cycle, the dark I-V characteristic curves of the PV module samples are measured automatically at (60º, 50º, 40º, 30º, and 25ºC). 47
Figure 2.3: Maximum power (P_{max}) degradation curves calculated from the dark I-V measurements at 25ºC, solid lines; and 60ºC, dashed lines, for PV modules undergoing potential-induced degradation stress testing. Each P_{max} on the y axis is normalized to the P_{max} measured before the start of degradation at the same temperature (either 25ºC or 60ºC). The final degradation levels are validated using light I-V measurements at the finish of the experiment, and plotted as star

symbols on the graph (matching the degradation levels estimated from the 25ºC dark I-Vs – full lines). 48
Figure 2.4: Relative power-loss estimation error δP_{deg} (at 60ºC) as a function of degradation level (calculated from the dark I-Vs measured at 25ºC) for all modules considered in the experiment. 48
Figure 2.5: Example of the P_{max} degradation estimation error d, measured at a stress temperature of 60ºC for module D-1. The red curve represents the measured error (relative to the 25ºC reference measurement); the blue curve represents the linear approximation of the error, resulting from fitting the initial and final values of the measured error. 49
Figure 2.6: Example of the error compensation method, for translating P_{max} degradation for module D-1, measured at a stress temperature of 60ºC to 25ºC conditions. 50
Figure 2.7: Power-loss estimation error δP_{deg} (from 60ºC to 25ºC), calculated for all PV modules, after the error compensation. 51
Figure 2.8: Normalized STC power of PV modules undergoing PID at 85% RH, -1000 V bias, and at three temperatures indicated on the plot. The data were obtained semi-continuously at the stress temperature. 53
Figure 2.9: Subset of the normalized STC power of PV modules undergoing PID at 85% RH, -1000 V bias, and at three temperatures indicated on the plot. The data are successfully fit linearly with the time (h) scaled to the power of two, and the intersection in time of the curves at the failure criterion of 0.99 relative power remaining can be seen. 53
Figure 2.10: Three point Arrhenius fit to the lifetime data with activation energy 0.85 eV. 95% confidence intervals are shown to either side of the Arrhenius fit. Lognormal distributions are shown around the data points and the analysis is extended to a hypothetical 25°C use condition as an example. 54
Figure 3.1: Light I-V characteristics of a crystalline silicon PV module with bypass diodes, affected by uniform shading (blue curve) – where the entire module covered with 1 layer of semi-transparent foil; and by partial shading – where only 2 cells were covered once with 2 layers of foil (orange curve), and once with 4 layers of foil (green curve). 59
Figure 3.2: Effects of partial (2 cells covered with 2 layers of semi-transparent foil) and uniform (100% module area covered with 1 layer of foil) shading on the light I-V parameters of a PV module with bypass diodes. The initial STC I-V parameters of the module were FF_0 =0.7, η_0=10.95 %, V_{oc0}=42.87 V, V_{mp0}=33.21 V, I_{sc0} = 3.97 A, I_{mp0}=3.62 A, $R_{s\text{-}ld0}$=1.82 Ωcm^2. 60
Figure 3.3: Method for calculating diagnostic parameters (FF_{dark}, $V_{d\text{-}max}$, V_p) from the high voltage/current region of the dark I-V. 61

Figure 3.4: $J_{Loss}(V)$ characteristic calculated from the dark J-V curve of a crystalline silicon solar cell affected by different power loss mechanisms (simulated through diode parameter changes): red – reference dark J-V (n_1=1, n_2=2, R_s=0.8 Ωcm2, $R_{sh}=10^9$ Ωcm^2, $J_{01}=10^{-13}$ A/cm^2, $J_{02}=10^{-10}$ A/cm^2); blue – increased R_s=4 Ωcm^2; black – decreased $R_{sh}=10^7$ Ωcm^2; green – increased $J_{01}=10^{-12}$ A/cm^2; magenta – increased $J_{02}=10^{-9}$ A/cm^2. 63
Figure 3.5: Electroluminescence image of module R1 taken at STC I_{mp} bias. The module sustained open-circuited cell interconnects, causing 1.7% STC P_{max} loss. 64
Figure 3.6: Semilog plot of the $J_{Loss}(V)$ characteristic of module R4 with open-circuited cell interconnects (full lines – no damage; dashed lines – after damage). 65
Figure 3.7: Electroluminescence image of a crystalline silicon PV module taken at STC I_{mp} bias. The module has sustained three rounds of mechanical damage to its cells. The module's STC P_{max} degraded with: a) initial – no degradation b) -2.8%; c) -6.3%; d) -10.4%. 66
Figure 3.8: Semilog plot of the $J_{Loss}(V)$ characteristic of a PV module with mechanically damaged solar cells (full lines – no damage; dashed lines – after damage during three events). 68
Figure 3.9: STC P_{max} degradation curves of the four modules affected by PID, as a function of stress time. The degradation curves were determined from in-situ dark I-V measurements. 69
Figure 3.10: Semilog plot of the $J_{Loss}(V)$ characteristics of module P2 (cyan – no PID; magenta – after PID) causing 4.6% STC P_{max} loss, calculated from the dark I-V curves were measured in-situ at stress temperature, during the accelerated PID stress test. 70
Figure 4.1: Normalized (L=256) EL intensity histogram of a crystalline silicon PV module which has sustained four rounds of mechanical damage to its cells. The module's STC P_{max} was measured after each round of damage and is shown relative to the initial value. The normalized gray level threshold TH/(L-1)=0.34 was calculated using Otsu's method [114]. 75
Figure 4.2: Standard deviation of the EL intensity distributions and percent or active/inactive module area IMA_{EL}, calculated for each degradation stage of the module. 77
Figure 4.3: Module map of active (blue - 80.4%) and inactive (red – 19.6%) areas, calculated by thresholding (at 0.34 ELI) the EL image of the PV module, taken after the last round of mechanical damage (STC P_{max} = 89.6% of initial value). 77
Figure 4.4: Example of dividing the module EL image into individual cell images for performing ELI distribution analysis on each solar cell. 78

Figure 4.5: EL image of cell (2, 5). The upper images show the solar cell before the degradation, whereas the lower images show the cell after the last round of mechanical stress. 79
Figure 4.6: Normalized (L=256) EL intensity histogram of cell (2, 5). The threshold value used was TH/(L-1)=0.34, calculated from the initial ELI distribution of the PV module. 80
Figure 4.7: Standard deviation of the EL intensity distribution and percent or active/inactive area for cell (2, 5), calculated for each degradation stage. 81
Figure 4.8: Diagnostic matrix of $IMA_{EL-Cell}$ cell-level parameters, calculated before (left) and after (right) the module degradation, for each cell within the module. The threshold value used was 0.34, calculated from the module's initial ELI distribution. 82
Figure 4.9: Distribution of $IMA_{EL-Cell}(k)$ cell-level parameters within the module, calculated for each degradation stage. 83
Figure 4.10: Boxplot of the distribution of $IMA_{EL-Cell}$ cell-level parameters within the module, calculated for each degradation stage. Median and STD are shown in red and blue, in percent units since the $IMA_{EL-Cell}(k)$ is measured in percent. 83
Figure 4.11: Diagnostic matrix of $STD_{Cell}(k)$ parameters, calculated before (left) and after (right) the module degradation, for each cell within the module. 84
Figure 4.12: Distribution of $STD_{Cell}(k)$ parameters within the module, calculated for each degradation stage. 84
Figure 4.13: Diagnostic matrix of $IMA_{EL-Cell}$ cell-level parameters, calculated before (left) and after (right) the PID stress, for each cell within the module. 85
Figure 4.14: Diagnostic matrix of "Median of cell ELI distribution" parameters, calculated before (left) and after (right) the PID stress, for each cell within the module. 86
Figure 4.15: Boxplot of the distribution of the "inactive cell area" $IMA_{EL-Cell}(k)$ (left) and "median of cell ELI distribution" (right) parameters within the module, calculated before and after the PID stress. Median and STD values are shown in red and blue. 86
Figure 4.16: Diagnostic matrix of $IMA_{EL-Cell}$ cell-level parameters, calculated before (left) and after (right) the damage to the cell ribbons, for each cell within the module. 87
Figure 4.17: Distribution of $IMA_{EL-Cell}(k)$ cell-level parameters within the module, calculated before and after the damage to the cell interconnects. 88
Figure 5.1: PV plant remote monitoring system. 92
Figure 5.2: Normal operation phase, when the PV array production data is monitored, together with the ambient conditions. 94

Figure 5.3: Field test setup consisting of a PV string (eight modules) and a commercial string inverter, for performing three test scenarios:(i) the PV string series is increased by +100%;(ii) 20% of one module is shaded;(iii) 50% of all lower cells in the string are shaded. 95
Figure 5.4: I-V curves of a mc-Si PV array affected by different types of shading and increased series resistance: red – normal I-V curve, magenta - +100% increase in the series resistance of the PV array; blue – partial shading affecting 20% of one PV module (8 total); green – uniform type shading similar to dirt accumulation on 50% of the surface of all lower solar cells. All I-V curves were acquired under similar irradiance and temperature................................. 96
Figure 5.5: Predicted vs. measured power for the case when the performance model is trained with MPPT of one minute averaged data, measured with a commercial inverter. 97
Figure 5.6: Predicted vs. measured power for the case when the performance model is trained with data extracted from I-V curves, measured with a commercial inverter. 98
Figure 5.7: Structure of the diagnostic system based on light I-V measurements.. 100
Figure 5.8: Performance curves of the three fuzzy classifiers: red – partial shadow classifier with irradiance sensor – for detecting uniform partial shadow types (shading 6); blue – partial shadow classifier without irradiance sensor; green – classifier for detecting increased series-resistance losses; magenta – classifier for detecting PID. 101
Figure 5.9: Field test setup consisting of a PV string (eight crystalline silicon modules connected in series), a commercial string inverter capable of measuring the I-V curve of the PV string every 10 minutes, and a variable resistor connected in series with the string.. 102
Figure 5.10: Test PV string affected by variable shading, due to an obstacle placed in front of one of the PV modules. 103
Figure 5.11: Test PV string affected increased series resistance (+50%). For some of the lower irradiance cases, the increased series resistance is not detected, since the detection system is at the lower limit of sensitivity................................ 104
Figure 5.12: Intelligent MPPT algorithm. 105
Figure 5.13: Power-voltage characteristic of a PV array in normal operation, and affected by three different partial shadows. 106
Figure 5.14: Comparison P&O and iMPPT operation during variable shading..... 107
Figure 5.15: Comparison of P&O and iMPPT operation during constant shading. 108

LIST OF TABLES

Table 1-1: Common PV module characterization and diagnostic methods for identifying the four degradation modes investigated 31
Table 3-1: Summary of main signatures for the four degradation modes investigated 58
Table 3-2: Relative change in the diagnostic parameters of the four PV modules that have sustained different levels of damage to their cell interconnects. 65
Table 3-3: Relative change in the diagnostic parameters for a PV module in different stages of mechanical degradation... 67
Table 3-4: Relative change in the diagnostic parameters measured for the four modules affected by PID. 69

NOMENCLATURE

List of abbreviations:

AC	–	Alternative Current
ADT	–	Accelerated Degradation Test
ALT	–	Accelerated Life Test
AM	–	Air Mass coefficient
BOS	–	Balance of system
DC	–	Direct Current
EL	–	Electroluminescence
ELI	–	Electroluminescence Intensity
FiT	–	Feed-in-Tariff
IR	–	Infrared
J-BOX	–	Junction box
LCOE	–	Levelized Cost of Energy
LID	–	Light-Induced Degradation
MPP	–	Maximum Power Point
MPPT	–	Maximum Power Point Tracking
MTTF	–	Mean Time to Failure
POA	–	Plane-of-array
PID	–	Potential-Induced Degradation
P-V	–	Power-Voltage characteristic
PS	–	Partial Shadow
P&O	–	Perturb and Observe
RH	–	Air relative humidity
SAPM	–	Sandia Array Performance Model
STC	–	Standard Test Conditions (1000 W/m^2, 25°C, AM 1.5)
STD	–	Standard Deviation
TTF	–	Time to Failure

List of symbols:

α	–	Temperature coefficient of short-circuit current
β	–	Temperature coefficient of open-circuit voltage
γ	–	Temperature coefficient of maximum power
γ_{dark}	–	Temperature coefficient of maximum power estimated from the dark I-V characteristic
δP_{deg}	–	Module power-loss estimation error
A	–	Diode ideality (quality) factor
A_0	–	Scale factor of Arrhenius process

CD_{EL}	–	Percent of damaged/degraded solar cell regions
E_a	–	Activation energy of Arrhenius process
FF	–	Fill factor
FF_{dark}	–	Dark I-V equivalent for the fill factor
G	–	Solar irradiation
I-V	–	Current-voltage characteristic
I_{dark}	–	Current component of the dark I-V characteristic
I_0	–	Dark saturation current of a PV cell
I_{01}	–	Dark saturation current of the first diode in the double-diode model, responsible for the diffusion current component
I_{02}	–	Dark saturation current of the second diode in the double-diode model, responsible for the recombination in the space charge region
IMA_{EL}	–	Inactive module area from an EL image
I_{mp}	–	Current at the maximum power point
I_L	–	Light-generated current
I_{sc}	–	Short-circuit current
J	–	Current density
J_L	–	Light-induced current density
J_{01}	–	Dark saturation current density corresponding to the diffusion processes
J_{02}	–	Dark saturation current density corresponding to the recombination in the space charge region
P_{deg}	–	Relative maximum power degradation
$\widehat{P}_{deg}$	–	Estimate of the relative max. power degradation
P_{max}	–	Power at the MPP
$p_{EL}(i)$	–	Normalized EL image histogram of a PV module
$p_{EL\text{-}Cell}(k, i)$	–	Normalized EL image histogram of solar cell k
R_s	–	Series resistance of the solar cell or PV module
R_{sh}	–	Shunt resistance of the solar cell or PV module
T	–	Module temperature
T_c	–	Solar cell temperature
TH	–	Gray-level threshold value
T_{ref}	–	Reference temperature
T_{stress}	–	Experiment stress temperature
V_{dark}	–	Voltage component of the dark I-V characteristic
V_t	–	Thermal voltage of a solar cell or PV module
V_{mp}	–	Voltage at the maximum power point
V_{oc}	–	Open-circuit voltage
d	–	Estimation error of the P_{max} degradation

$\hat{d}$	–	Linearized estimation error of the P_{max} degradation
K	–	Boltzmann's constant
ns	–	Number of series connected cells in the module,
Q	–	Charge of an electron
T	–	Time
t_0	–	Initial time point
t_{final}	–	Final time point
t_k	–	Time at measurement sample k

CHAPTER 1 INTRODUCTION

This chapter presents the background and the motivation of PhD thesis, continues with objectives and limitations encountered, and ends with the list of the main contributions brought to this project along with a short presentation of the thesis outline.

1.1 BACKGROUND AND PROJECT MOTIVATION

1.1.1 CURRENT STATUS OF PHOTOVOLTAIC TECHNOLOGY

Photovoltaic (PV) energy has become one of the most important renewable energy technologies, reaching a global cumulative installed capacity of approximately 139 GW at the end of 2013, and at least 174 GW forecasted by the end of 2014 [1]. This significant growth of the PV market, shown in Figure 1.1, was possible due to favorable PV energy support policies [1], as well as considerable excess production capacities, which have led to substantial reductions in PV module prices [2].

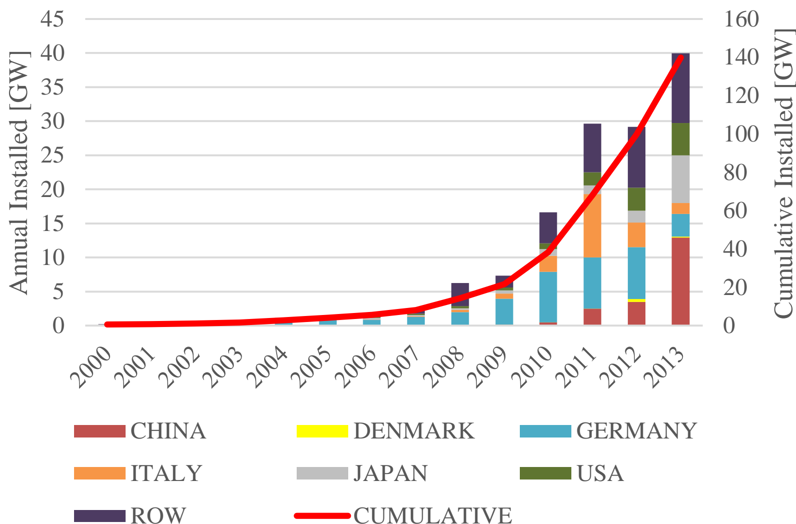

Figure 1.1: Evolution of annual PV installations (GW) [3].

From a technology perspective, Si-wafer based modules still dominate the market, accounting for about 90% of the total production in 2013 [4]. Considering module efficiency, the highest values achieved for mono and multi-crystalline modules were 22.9% and 18.5% respectively as of January 2014 [5]. Whereas the average efficiency for commercial wafer-based silicon modules reached ~16% at the end of 2013 [4].

Nowadays, quality PV modules are warranted for 25 years with a maximum estimated degradation rate of 0.8%/year [6], which is largely based on long-term performance data for older PV technology, as well as financial and statistical modeling.

These modules typically undergo a qualification test, such as the IEC 61215 for crystalline silicon modules, or the IEC 61646 for thin film modules, as well as the IEC 61730 test for module safety qualification. These qualification tests are able to identify design, material and process flaws that could lead to premature field failures, but they are not sufficient to demonstrate over 25 years of service lifetime [6].

A recent study on PV module degradation rates [7] reported that crystalline silicon modules have a median power degradation rate of 0.5%/year, but which can vary significantly with the installation year, and local climate conditions [8]. Variations in the module degradation rates with installation year are usually associated with module technology issues, which can result in the accelerated degradation of some of the module components. The local climate conditions play an equally important influence on the degradation rates of the module [7, 8]. As crystalline silicon module operated in temperate climates show lower degradation rates, modules operated in desert or tropical climates show higher degradation rates, which can easily go above 1%/year, due to the high temperatures and/or moisture [7, 8]. The increased degradation rates are caused by a series of failures and degradation modes affecting the PV system over the course of its lifetime. These failures not only decrease the performance of the PV system, but also pose a risk to the safe and long term operation of the PV system [9].

1.1.2 COMPETITIVENESS OF THE PHOTOVOLTAIC MARKET AND OUTLOOK

Considering the significant cost reductions and technology advances in the last years on one side, and the open-end question of reliability and lifetime on the other, PV still remains a policy-driven market in most countries in the world [1]. An analysis of the PV market incentives and enablers for 2013, shown in Figure 1.2, reveals that more than 70% of the global Pmarket was driven by Feed-in-Tariff (FiT) schemes, 16% was represented by investment subsidies, and only 4% of the global market has been driven by self-consumption or the sole competitiveness of PV in 2013 [3].

The recent decline in political support for PV in several European countries, by modification or phasing-out of national support schemes, has slowed or even halted the development of PV markets and industries these countries [1, 3].

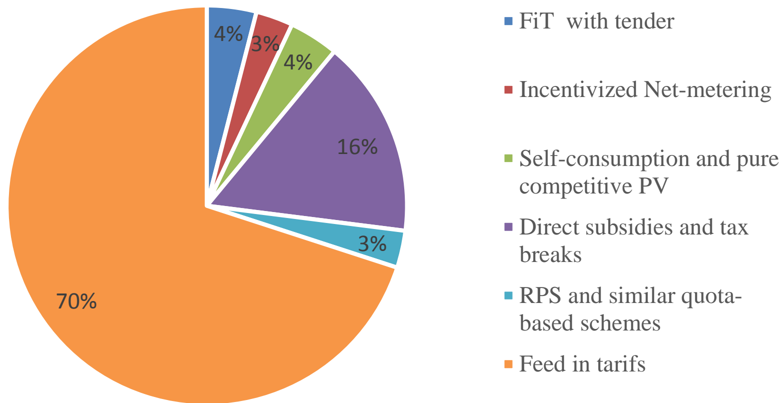

Figure 1.2: PV market incentives and enablers for 2013 [3].

In this context additional effort must be invested in the research and development of PV technologies that can enable the bankability of PV without subsidies, and making PV competitive with fossil fuels worldwide.

The competitiveness of PV energy can be compared with other energy sources, such as fossil fuels or wind energy, by calculating the levelized cost of energy (LCOE), as shown in Figure 1.3 for the USA (2014) [10] and Germany (2013) [2] energy markets.

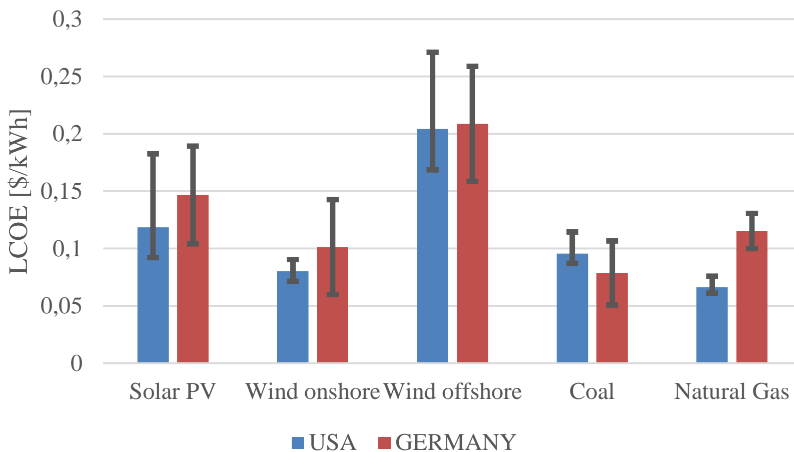

Figure 1.3: LCOE of renewable energy technologies and conventional power plants in USA (2014) [10] and Germany (2013) [2].

Here we can observe that the average LCOE for solar PV in USA, including subsidies, is approximately 0.118 $/kWh, higher than for conventional coal (0.095 $/kWh), natural gas (0.066 $/kWh), as well onshore wind (0.080 $/kWh) [10]. Similar LCOE trends can be observed for the German market [2].

In order to increase the competitiveness of solar PV, the main cost factors associated with solar PV, shown in Figure 1.4, have to be reduced [11]. In the last years, the decrease in module prices was the main driver in reducing the investment cost for solar PV [3]. However, in the following years, other cost factors, such as: (i) plant yield, (ii) useful lifetime of the plant, (iii) operation and maintenance costs, have to be optimized in order to make solar PV competitive.

In this respect there are several important technology goals that have to be achieved in the next years: (i) ensuring a 25+ years module lifetime, (ii) reducing the average module degradation bellow 0.5 %/year, (iii) developing methods for the timely detection of faults and underperformance in a PV system/plant.

These technology goals can be achieved by intensifying the research and development on: (i) module reliability and durability testing, that can predict module operation, degradation and failure rates in the field; (ii) module characterization and diagnostic methods, that can accurately identify the types of degradation and failure modes in a PV module; (iii) diagnostic methods and systems for PV plants, that can detect failures and ensure the optimal operation of the plant.

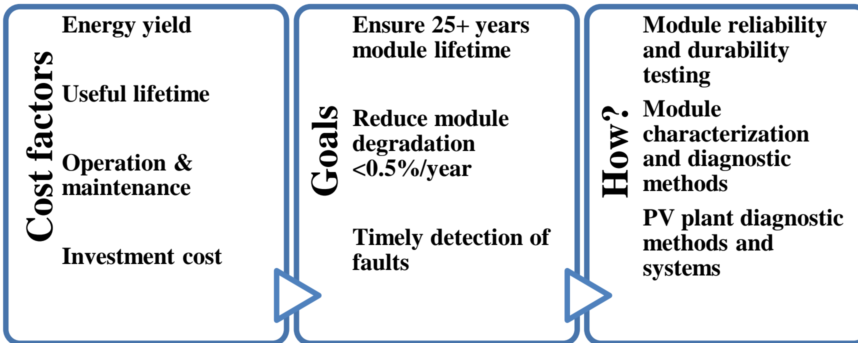

Figure 1.4: Main cost factors for solar PV, with the some of the most important technology goals to be achieved in order to drive the cost down.

1.2 PROBLEM FORMULATION

1.2.1 OVERVIEW OF THE DEGRADATION AND FAILURE MODES INVESTIGATED

Since there is a large spectrum of potential failures and degradation modes affecting PV modules nowadays, we have focused the scope of our investigation on four important types of degradation modes affecting wafer-based crystalline PV modules: (i) optical losses and degradation, (ii) degradation of the electrical circuit of the PV module, (iii) mechanical degradation of the solar cells, (iv) potential-induced degradation (PID) of the solar cells. Nevertheless, other failures modes of equal importance are not covered by these four types, and need to be addressed.

Optical losses and degradation can occur due to a series of factors that affect the optical layer of the PV module and reduce the amount of light reaching the cell surface. The most common of these factors are: encapsulant discoloration (Figure 1.5a), air bubbles or delamination (Figure 1.5b) [9, 12], soiling (Figure 1.5c) and shading [13, 14], front-glass corrosion or breakage (Figure 1.5d) [9], and deterioration of the antireflection coating [13, 15].

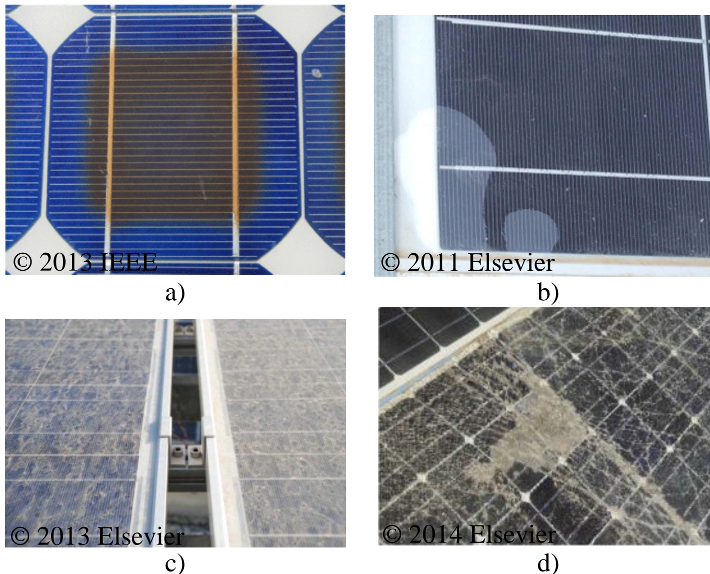

Figure 1.5: Typical causes for optical losses in fielded PV modules: a) EVA discoloration (reprinted from [16] with permission from IEEE); b) bubbles/delamination (reprinted from [15] with permission from Elsevier); c) front glass soiling (reprinted from [17] with permission from Elsevier); d)glass breakage (reprinted from [18] with permission from Elsevier).

Nowadays power loss due to encapsulant discoloration is less than 0.5%/year [9], although more severe cases have been reported in the past [13]. However ethylene vinyl acetate (EVA) encapsulant delamination has been reported to cause 4% power loss [12].

Front glass soiling is highly dependent on the site, weather patterns and mounting type and can cause an annual energy loss of up to 6% [14], although extreme cases with heavy pollution can lead to 10% or more power loss [19]. Shading occurs most often in residential applications and improperly designed PV systems [14], where depending on the relative position of the shadow and the bypass diodes configuration, it can cause significant power losses [20]. Apart from power loss, localized soiling, shading, discoloration, or delamination may cause current mismatch and reverse biasing of the affected solar cells, resulting in localized heating, causing the formation of *hot-spots* [21, 22], and even lead to module failure [13].

Factors causing optical losses usually leave a visual imprint on the PV module surface and can be detected through visual inspection [9, 13]. From an electrical perspective, uniform shading or degradation of the optical layer are characterized by a decrease in fill factor (FF) and degradation of the short-circuit current (I_{sc}) [23], due to the reduced amount of light reaching the solar cells. Furthermore, certain types of partial shading or optical degradation can be detected from the distortion they cause in the light current-voltage (I-V) characteristic [24, 25], whereas more generic fault-detection techniques identify shading by correlating power loss with a specific time of day [26] or relative position of the sun [27, 28].

Degradation of the electrical circuit of the PV module concerns the partial or total failure of the PV module's electrical components: busbars, cell and string interconnects, wiring, junction box connections, and cable connectors, except the solar cells themselves, which are examined separately. These electrical components can degrade over time, leading to power loss and potential hazards [9, 29, 30]. Degraded cell and string interconnects are often the result of poor soldering, mechanical stress, and thermal cycling [9, 29]. These can give rise to an increase in the module's series resistance (R_s) [29, 30], increased heating in the module, and localized hot spots [15, 30]. Fielded modules exhibiting such interconnect failures often go undetected especially in residential PV systems because they require infrared (IR) thermography or circuit fault detectors to be identified [31]. Furthermore, moisture ingress can cause corrosion of the module connectors [32], cell busbars and interconnect ribbons (Figure 1.6) [33], as well as corrosion of the string interconnects in the junction box [9], manifested as an increase in the PV module's series resistance and power loss [32].

Detecting this type of degradation would require visual inspection or IR imaging of the cables, connectors, and junction box.

Figure 1.6: Example of corrosion in the busbars and interconnect ribbons observed in different modules (reprinted from [33] with permission from IEEE).

Alternatively, accurate series-resistance measurements [34, 35], would reveal an increase in the module's series resistance. Other electrical "symptoms"/signatures indicating this degradation mode are: (i) decrease in *FF* [9, 29], (ii) decreased slope of the light I-V curve near the open-circuit voltage (V_{oc}) [36], (iii) and in extreme cases (R_s>10 Ωcm^2) a reduction in I_{sc} [37]. Similar effects can be observed in the high current region of the dark I-V curve [38].

Mechanical damage and degradation of the solar cells such as microcracks and fractures, can occur during the manufacturing process [39], module packaging and transport [40], module installation [9] and operation in the field due to mechanical [41] and thermal stresses [42]. Cell microcracks by themselves usually have a small impact on the performance of the module [43]. However, additional mechanical and temperature stresses can lead to cell fractures, where part of the cell breaks off (especially the metallization) and becomes inactive. Depending on the affected cell area, cell fractures can cause significant power loss, localized heating, and hot spots, due to the reverse biasing of the remaining active cell area [39, 44, 45].

Cell microcracks and fractures have no visual impact on the module surface, except for the so-called "snail tracks" that sometimes appear [9], and they can be difficult to detect without the help of diagnostic tools such as IR thermography [45] or electroluminescence (EL) imaging (Figure 1.7) [46, 47]. From an electrical diagnostic perspective, investigations on individual crystalline solar cells affected by microcracks have revealed increased recombination losses occurring in the depletion region (J_{02}) [48] of the solar cell, as well as increased shunting losses (decreased R_{sh}) [49]. As the cell microcracks develop into fractures their impact on the I-V characteristic becomes more noticeable, and is manifested by an increase in the internal series resistance of the module R_s, decreased *FF*, and as well as a decreased in current generation (I_{sc}) due to the loss of well-connected cell area [43, 44].

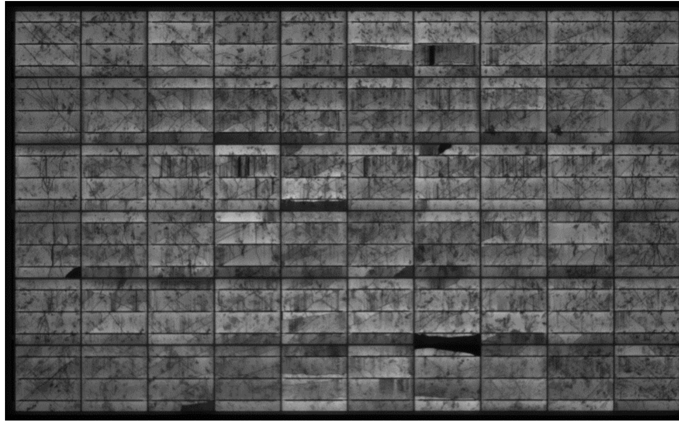

Figure 1.7: Example electroluminescence image of a multi-crystalline silicon PV module with cell cracks. Module power degraded down to 94.7% of the initial STC P_{max}.

PID of solar cells and modules, first investigated and reported by del Cueto in 2002 [50], and by Swanson in 2005 [51], has become an important reliability concern for PV systems, due to the relatively rapid and significant negative impact it can have on the performance of the plant [52-54].

In most PV systems nowadays, the modules are series-connected to increase the system voltage and reduce losses, whereas the metallic frames/mounting components of the modules are usually grounded to a fixed potential, for preventing electric shock to humans [52, 55]. This situation, depicted in Figure 1.8 for a PV array connected to a transformerless inverter, leads to voltage biasing of the solar cells relative to the module frame (ground), causing small leakage currents to flow [52, 55]. This voltage bias poses a stress for the solar cells and PV module components, and can lead to different types of damage or degradation typically known as PID [52, 55].

The onset of PID in a PV system is difficult to predict, since it is dependent on a combination several factors, such as: (i) the magnitude and polarity voltage bias [51, 56]; (ii) frame/grounding configuration [57]; (iii) inverter type [9, 52]; (iv) solar cell type [50, 58]; (v) environmental factors – high temperature and humidity [56, 59]; (vi) module components – glass type [54, 55], encapsulant type [52, 54], or anti-reflective coating [52, 55].

From a diagnostic perspective, PID of crystalline silicon solar cells and modules has been associated with cell shunting (R_{sh}) [52, 54, 55] and recombination losses occurring in the depletion region (J_{02}) [60, 61]. Electrical "symptoms"/signatures of PID include: (i) a significant decrease of the FF [52, 54], (ii) decreased R_{sh} [52, 55, 62], (iii) decrease of the low-light performance [53, 62], (iv) and degradation of the V_{oc} [52, 55, 62].

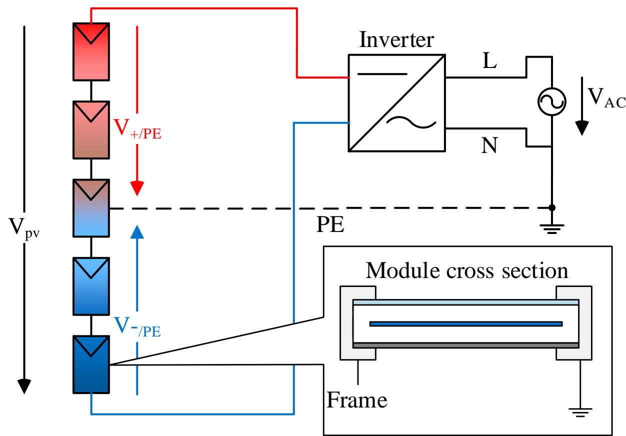

Figure 1.8: Schematic of a PV array connected to the grid by means of a transformerless inverter (redrawn from [63]).

However, in most cases crystalline silicon PV modules affected by PID do not show any visual symptoms [9], as exemplified in Figure 1.9 (left) for a multicrystalline PV array affected by PID [64]. Commonly PID can be detected in the field by IR thermography, considering the increased heating caused by power loss/shunting in the modules closer to one of the PV array ends, and the typical chessboard pattern associated with PID [9], as shown in the thermo-graphic image in Figure 1.9 (right).

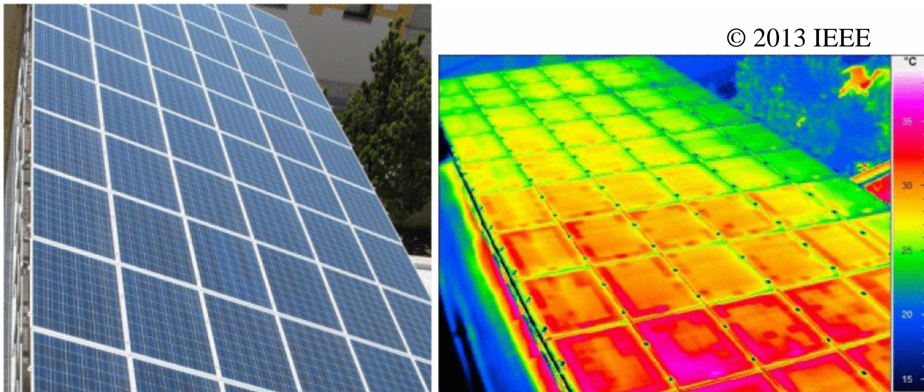

Figure 1.9: PV system affected by PID in Southern Europe (reprinted from [64] with permission from IEEE). Left picture shows no visual symptoms of PID, whereas the IR picture on the right shows heating due to power loss/shunting of the modules.

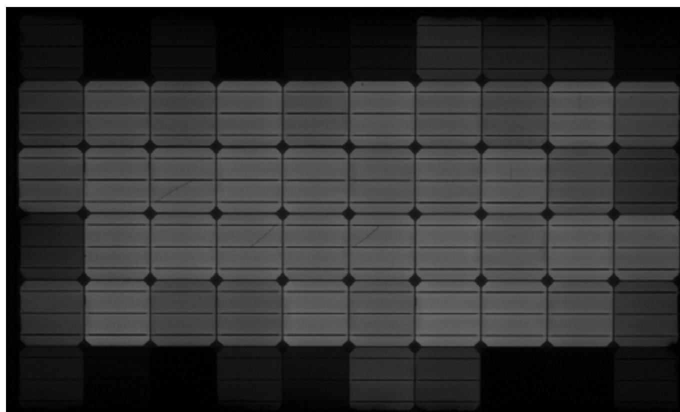

Figure 1.10: Example electroluminescence image of a mono-crystalline silicon PV module affected PID. Module power degraded down to 76.8% of the initial STC P_{max}.

The most reliable way for detecting PID is by low current bias EL imaging [9], where crystalline silicon modules affected by PID show the typical “chessboard” pattern [9], similar to Figure 1.10, where the solar cells closer to the module frame are more degraded than those closer to the center.

Other methods for detecting PID in the field are I-V curve monitoring [9] and measurement of module V_{oc} at both ends of the string during low-light conditions [62]. However, these are not always easy to apply on a large scale, and in many cases, PID can remain undetected until the degradation becomes severe [9, 53]. Moreover, it is difficult to estimate how many installed systems are currently affected by PID, although the number of reported cases is increasing [53]. This makes PID and important reliability concern, since it can lead to a significant impact on the performance of the PV system over time [52-54].

1.2.2 MODULE RELIABILITY AND DURABILITY TESTING FOR PID

Since the current IEC 61215 and IEC 61646 module qualification tests can only screen infant mortality problems, and cannot predict the long term operation of the modules, new module durability tests are necessary to ensure 25+ years of service lifetime [6, 65]. In this context there is a need to go beyond qualification testing, and to develop tests for module materials and components (encapsulants, backsheets, cables, connectors, junction boxes, bypass diodes), as well as specialized module stress tests (thermal cycling, dynamic mechanical load, enhanced hotspot, PID), which together are currently being denoted as “Qualification Plus Testing” [11, 65].

Amongst the main module degradation modes addressed by the “Qualification Plus Testing”, PID of crystalline silicon modules was focused upon in the current work.

Considering the many factors involved in triggering PID in a module/system, it is not trivial to predict if and how a module will be affected by PID for a given system configuration and local climate conditions. Thus there is an urgent need to develop relevant tests that can ensure the reliable and PID-free operation of modules for a long time. This requires the development of new tools and methods for accelerated stress testing and assessing the susceptibility of modules to PID.

Presently, there are no standard methods for testing or predicting the durability of PV modules in regards to PID [6]. Though, efforts are being made to develop such a test standard for detecting PID in crystalline silicon PV modules, denoted as IEC 62804 [66]. This current draft of the standard proposes a pass/fail PID test based on two accelerated stress test methods. The first method requires environmental chamber testing at 60°C temperature and 85% relative humidity (RH), where the modules are subjected to nameplate voltage bias (±1000 V) for 96 hours [67]. The second method, an alternative to chamber testing, can be performed at room temperature (25°C/40% RH) for 168 hours of stress under nameplate bias voltage while the front glass is covered by a conductive foil [67]. The pass criterion requires that modules are tested at both polarities, and show <5% power degradation, as well as pass IEC 61215 ed. 2 visual inspection criteria [67].

However, the pass/fail test cannot accurately quantify the lifetime of the module in relation to PID for given operation and local climate conditions. In this regard further research is necessary for understanding how the modules are affected by the voltage stress, as well as for developing relevant degradation and lifetime models.

An important challenge for developing such module degradation and lifetime models, especially through accelerated stress testing methods, is the accurate Standard Test Conditions (STC, 1000 W/m^2, 25°C, AM 1.5) performance monitoring of the modules during the degradation process. Collecting sufficient STC maximum power (P_{max}) degradation data from modules undergoing PID stress testing, has always been a time-consuming and expensive task. Performance characterization of PV modules undergoing accelerated PID stress testing generally involves intermittently removing the module from chamber and measuring its power on a solar simulator, which can require considerable time and effort when numerous samples are involved [60]. Often this results in acquiring just a few intermediate P_{max} degradation measurement points, which can make the data analysis and modeling of the degradation mechanism difficult and insufficiently accurate.

There are several methods for monitoring module degradation during accelerated PID stress testing, by measuring different electrical parameters of the module, although not all of them can be easily correlated to the STC performance of the modules.

The most accessible method for monitoring module degradation during PID stress testing is to monitor the module leakage current and accumulated charge [54, 59, 62],

which can be a good indicator of the progress of PID, although estimating the STC performance degradation can be difficult [59].

A second method is to monitor the shunt resistance (R_{sh}) of the of the solar cell or module undergoing PID stress testing [68]. This method assumes that PID is characterized mostly by ohmic shunting [68]. This assumption works well for solar cells, and can be used to estimate the performance loss from the R_{sh} measurement [68]. Although this method has certain limitations when applied to modules, due to the interconnection of multiple cells with different degrees of PID [68].

A third solution is to integrate a solar simulator into the environmental chamber/test setup, which would allow accurate STC performance characterization [69]. However, this method requires significant hardware resources, and is limited in the number of modules/solar cells that can be monitored during the test.

An alternative solution for characterizing module power degradation for PID accelerated lifetime testing, was proposed in [70], by in-situ characterization of the STC module performance degradation, from dark I-V measurements taken at 25°C. This method still requires ramping down the chamber/module temperature to 25°C, for estimating the STC module degradation. However, the module performance degradation monitoring and acquisition can be improved by estimating the STC module performance degradation from dark I-V measurements taken directly at the elevated stress temperature, and avoiding transients and possible errors due to the periodic module temperature ramp downs.

Publications I and II address these issues, to improve the data collection process and reduce testing time, and build upon this method to develop accelerated lifetime models for crystalline silicon PV modules undergoing PID. Further details are presented in **Chapter 2** of this thesis.

1.2.3 MODULE CHARACTERIZATION AND DIAGNOSTIC METHODS

PV module characterization and diagnostic methods are necessary to detect and identify degradation and failure modes affecting fielded PV modules as well as defects in new modules. Such methods can help spot certain weakness in module technology or design, identify problems with the system installation or configuration, as well as degradation and failures specific to that location or climate. This leads to understanding what the specific degradation or failure modes are, as well as why and how they occur; so that we can develop module durability tests and methods for detecting and predicting them, as discussed for the case of PID in the previous section.

From a field application perspective, being able to accurately identify the type of failure or degradation, in a fast and cost efficient manner, opens up the possibilities for advanced PV system monitoring solutions and optimizing PV system maintenance actions, based on the type and severity of the failure.

To limit the large spectrum of potential failures and degradation modes affecting PV modules nowadays, we have focused the scope of our investigation on four important groups, described in the previous sections and summarized in Table 1-1.

The process of identifying these four groups of module failure and degradation modes, requires different characterization and diagnostic methods, the most common of which are: visual inspection, IR thermography, EL imaging, and I-V characterization. Choosing the right diagnostic method involves striking a balance between: versatility, hardware cost, accuracy of identification, duration and complexity of the diagnostic process. Another important aspect which must be considered for present day needs, is the possibility of automatizing the diagnostic process through machine analysis of the diagnostic parameters. This would enable diagnosing a large volume of modules in a short time, thus reducing man-power and costs. Moreover, such an approach would enable the development of PV module condition monitoring applications that can identify degradation and failure much faster than traditional methods.

Table 1-1: Common PV module characterization and diagnostic methods for identifying the four degradation modes investigated

Degradation mode	Common diagnostic methods
Optical losses and degradation	Visual inspection, I-V charac.
Degradation of the electrical circuit	IR therm., I-V charac., EL imaging
Mechanical degradation of the solar cells	EL imaging
Potential-induced degradation of the solar cells	EL imaging, I-V characterization

The advantages and limitations of theses characterization and diagnostic methods in relation to the four degradation modes summarized in Table 1-1 are briefly discussed next. However, amongst these four methods, I-V characterization and EL imaging based diagnostics were focused upon in this work, and will be discussed in more detail here and in the following chapters.

Visual inspection

From the four common diagnostic methods summarized in Table 1-1, visual inspection is most suitable for identifying the factors causing optical losses, as well as the degradation of the optical layer. However, this method is limited in identifying electrical degradation or failures, unless these leave a visual footprint on the module, such as burn marks or corrosion.

IR thermography

In contrast to visual inspection, IR thermography is capable of identifying electrical degradation or failures characterized by increased R_s, disconnected or shunted cells, or other issues causing a variations in the temperature distribution of

the module. The sensitivity and resolution of IR thermography is more limited than for EL imaging. Nevertheless, from a field application perspective, IR thermography inspection can be performed on module or system level, allowing the fast inspection of a large number of modules, but requiring mobile platforms and trained personnel [9, 45]. However, research in ongoing on developing more advanced diagnostic methods such as aerial drone-mounted thermography for automated field inspection of PV systems [71].

I-V characterization

Compared to the other three diagnostic methods, I-V characterization can be used to identify both optical and electrical degradation and failures. Moreover, the I-V characterization process can be performed in the field by string or module converters with a DC/DC boost stage, enabling the implementation of automatic I-V-based diagnostic methods, directly in the power electronic converter.

One way to achieve this is by analyzing different parameters of the light I-V curve, such as: I_{sc}, V_{oc}, V_{mp}, I_{mp}, FF, or the slopes of the I-V curve near I_{sc} or V_{oc} which are sensitive to changes in module R_s [72], and R_{sh} respectively [68]. This approach, investigated in Publications IX-XII, is most suitable for developing PV plant level diagnostic systems**,** and will be further discussed in **Chapter 5**. Nevertheless these methods can be readily applied to PV modules.

An alternative PV diagnostic method is to determine the single-diode [73] or two-diode model [38] parameters from light or dark I-V measurements, which provide physical interpretation of the degradation and failure processes affecting the PV module. This methodology, based on the analysis of the diode model parameters was applied in Publication III for investigating the operation and characteristics of different solar cell technologies. Moreover, the diode model analysis was applied in Publications IV and V as a modelling and diagnostic tool for PV modules and arrays. However, this approach has two drawbacks in the context of this work. Firstly, identifying all the diode-model parameters necessary to identify the four degradation modes investigated, through curve fitting for example, requires expert knowledge and an iterative process to yield correct and realistic parameters. This makes automatizing the diagnostic process through machine analysis more difficult.

Another limitation of this approach is for PV modules with mismatched solar cell I-V characteristics, hindering the application of an average solar cell model for the entire PV module. This can occur when the solar cells of the module are degrading at different rates, as is the case for PID, where the cells closer to the module frame degrade more rapidly than those closer to the center. This phenomenon is clearly shown in [55] for a standard crystalline PV module affected by PID, where the light I-V curves of the solar cells closer to the module frame have a very different characteristic compared to those close to the module center. The aggregation of all

these solar cell I-V characteristics into a single module I-V curve may no longer allow analysis with a singular diode model. Nonetheless, this is one of the most widespread and successful PV diagnostic tools available.

These limitations were addressed in Publication VI, were we proposed a machine analysis friendly method for identifying the four module degradation and failure modes, based on the analysis of the light I-V and dark I-V characteristics. The methodology and main results of the method are presented in **Chapter 3** of this thesis.

Electroluminescence imaging

EL imaging is an excellent tool for identifying a wide array of module failures and defects, such as: cell cracks, disconnected cell areas, broken ribbons and fingers, increased series resistance regions, PID, shunted cells, humidity corrosion, or cell manufacturing defects [9]. Moreover, complementing EL imaging with I-V performance characterization, and visual inspection, can cover most important failure and degradation modes affecting PV systems, and can be a very effective and comprehensive diagnostic methodology. Such a diagnostic approach was explored in Publication V, for determining the main degradation and failure modes affecting a 15 year old PV system. However, such an approach can be time consuming, and does not lend itself to wide scale application.

Moreover, compared to I-V characterization and IR thermography, field application of EL imaging is more limited, requiring a complex hardware and diagnostic process [74], restricting the frequent application of the method in the field.

Despite its widespread adoption as a PV module diagnostic tool in PV laboratories and research institutes, EL imaging is mostly used as a qualitative diagnostic method, lacking standardized measurement procedures and failure quantification methods. Currently a new IEC standard is being developed for EL of photovoltaic modules (proposed future IEC TS 60904-13) [75], where some of these issues will be addressed.

Nevertheless, EL imaging has a great potential for machine analysis, in identifying and quantifying degradation and failures in PV modules, similar to what has already been done for the automatic detection of manufacturing defects of silicon wafers and cell [76-78]. In this regards, further research is needed for developing metrics and methods of quantifying the extent of degradation and failures distributed within a module: such as cells cracks, fully or partially disconnected cell areas, shunted cell areas, increased series resistance areas, cell voltage mismatch etc. Such metrics would allow to evaluate and compare the extent of failures within a module after module transportation or field operation, such as cell cracks, partially disconnected cell areas, or cell mismatch, which may not currently have a significant impact on the performance of the module. These issues will be further explored in **Chapter 4** of this thesis.

1.2.4 PLANT DIAGNOSTIC METHODS AND SYSTEMS

PV plant diagnostic methods and systems have the purpose to detect, identify, and locate degradation and faults of the PV system components, preferably in the early stages of degradation or failure. In this context preventive and/or reparative maintenance ca be performed, so that power loss can be minimized. If the diagnostic methods are automatized, the cost of plant operation and maintenance can be reduced.

Most electrical-based diagnostic methods for PV systems rely on some type of model to detect faults in the PV plant. These models are used to estimate one or more system parameters, such as plant energy yield or output power, from: local irradiance and temperature measurements [79-81]; satellite observations [26, 82]; or other system parameters [83, 84]. These estimates are then compared with measured system values to detect faults or underperformance of the PV system. The data analysis and modelling process can be based on analytical models of the PV generator [82, 84], empirical performance models [26, 83], generic estimators [85, 86], or statistical models [87], involving different degrees of complexity. The main advantage of these methods is that they usually have low hardware requirements and can be applied to a wide range of PV systems and plants. However, a common limitation of these methods is that they cannot accurately identify the cause of the fault or its location.

Another important limitation of model-based diagnostic methods is that obtaining an accurate model of the system can be difficult, and usually requires a dedicate system identification step, or parametrization by an expert user. We suggest a possible solution to this limitation in Publication VIII, where we propose a method to identify the PV model parameters online, during the operation of the PV system. The methodology and main results of this method are presented in Chapter 5 of this thesis.

In contrast to model-based methods, diagnostic methods based on signal response analysis, such as time-domain reflectometry [88] and Fourier analysis [89], can be used to identify and localize open-circuit type faults and arcing occurring in a PV system. However they are limited in detecting other types of faults, and need to be complemented by other diagnostic methods [88].

A third group of diagnostic methods is based on measuring and analysing the I-V characteristic curve of the PV array. In comparison with yield measurements, I-V curves can provide a lot more information regarding the condition and electrical properties of the PV array, such as: short-circuit current, open-circuit voltage, fill factor, series and shunt resistance, ideality factor [13, 90, 91], as well as indicate the presence of shading and soiling [25, 92], or other conditions. And considering the existing experience with module level I-V characterization and diagnostics, I-V based diagnostic methods for PV arrays have a great diagnostic potential.

I-V based diagnostic PV methods can be combined with other diagnostic methods, such as PV model analysis, and EL imaging, as was done in Publication V, which can provide valuable insight into the degradation modes and ageing of the different

components of the PV system. However the main advantage of these methods is that they can be automatized, considerably reducing the diagnostic effort. In this regard, in Publications IX-XI we proposed several I-V based diagnostic methods, for detecting shading, increased series resistance losses, and PID, affecting PV arrays that can be implemented directly in the inverter, or in a condition monitoring system. The methodology and main results are shortly described in Chapter 5.

Integrating such a method in a solar inverter is mostly a matter of implementing the I-V sweep functionality in the control software of the inverter. A good platform for implementing such diagnostic methods are dual-stage string inverters, which due to the boosting stage, are capable of sweeping the full I-V characteristic of the PV string or array connected at the input. Such commercial string inverters, like the Danfoss TLX Pro, capable of full I-V sweep [93], are already on the market, and have been used in this thesis as field testing and demonstration platform for different PV plant diagnostic methods. Further details about this platform can be found in Publication VII and in Chapter 5 of this thesis.

Nonetheless, I-V based diagnostic methods are not limited to dual-stage PV inverters, and could also make use of the partial I-V curve, measured by single-stage inverters, which have a limited I-V sweep capability.

In addition to warning the plant operator about power loss and faults occurring in the PV plant, PV diagnostic methods can also be used to improve the control and performance of the PV system during non-optimal operation conditions. An example of such a situation is for PV systems frequently affected by partial shading, as can be the case for some residential PV systems [20, 94]. Depending on the relative position of the shadow with the bypass diodes configuration, even a small area shadow can cause high power losses [94].These losses can be further aggravated by the creation of multiple maximum power points (MPPs) on the array's power-voltage (P-V) curve. The common MPP tracking (MPPT) methods such as perturb and observe (P&O) [95] or incremental conductance (INC) [96] have local maxima behavior, meaning that if a local maxima on the P-V curve is found, it will stop there [97].

Several Global MPPT methods for solving this problem have been previously proposed, such as the a two stage global MPPT method presented in [98], the Global Peak (GP) MPPT proposed in [99], or the Real MPPT detailed in [100]. These methods are characterized by different degrees of complexity and applicability.

An alternative solution is to integrate a partial shading detection method with the MPPT control of the inverter. The diagnostic method can detect the presence of partial shading, then trigger a partial I-V scan of the PV array to find the global MPP, and finally inform MPPT about the location of the global MPP. This intelligent MPPT concept was implemented and experimentally demonstrated in Publication XII, and is shortly described in Chapter 5 of this thesis.

1.3 PROJECT OBJECTIVES

i. To develop an automatic in-situ module power degradation estimation method for crystalline silicon modules undergoing accelerated PID stress testing that can be applied directly at the elevated stress temperature of the module, and does not requires temperature ramp down or interruption of the test.

ii. To develop a diagnostic methodology for PV modules that can be used to identify degradation and failure modes in crystalline silicon PV modules.

iii. To develop a diagnostic methodology for crystalline silicon PV modules for assessing and quantifying the distribution and extent of degradation, failures, and mismatch within a PV module by electroluminescence imaging

iv. To develop field diagnostic methods and algorithms that use the I-V characteristic of the PV array to detect and identify faults and degradation affecting the PV system.

1.4 PROJECT LIMITATIONS

- The characterization and diagnostic methods presented in this thesis were developed and tested for standard crystalline silicon modules and arrays, which is the prevalent PV technology nowadays, however other relevant technologies exist for which the methods were not tested.
- Although there are a number of important degradation and failure modes affecting crystalline PV modules, only four types were addressed: (i) partial and uniform shading: (ii) increased series resistance losses (increased module resistance and interconnect breaks); (iii) cell cracks and breaks; (iv) PID.
- The field diagnostic methods were tested only on a small scale 1.9 kWp PV system, for shading and increased series resistance losses only. Testing for PID was performed only on module level.
- Some of the PV plant diagnostic methods and systems were tested offline on a PC using measurement data acquired from the commercial string inverters, and were not directly implemented in the inverter control software, due to its closed and proprietary nature.

1.5 MAIN CONTRIBUTIONS

The main contributions of this thesis can be summarized as follows:

- **Automatic in-situ power degradation monitoring of modules undergoing PID stress testing, from stress temperature dark I-V measurements.**

This method implies semi-continuous dark I-V characterization of the PV

modules under test, at an elevated stress temperature, without interrupting the test. The dark I-V curves are then used to determine the degradation of the module's maximum power at STC, as a function of time and stress level. This leads to reduced test duration and cost, avoids stress transients while ramping to and from the stress temperature, eliminates flash testing except at the initial and final data points, and enables significantly faster and more detailed acquisition of statistical data for future application of various statistical reliability models.

- **New module degradation and failure mode identification method.**

A PV module diagnostic method was developed by combining the strengths of light I-V and dark I-V characterization, for the purpose of identifying degradation modes such as: (i) optical losses and degradation, (ii) cell cracks and breaks, (iii) degradation of the external circuit of the PV module; (iv) PID. This method, which is machine analysis friendly, can identify incipient degradation in modules, which would otherwise be difficult to detect from light I-V measurements alone. The method can be used as a laboratory diagnostic tool, and can also be implemented in future field applications, for example in: (i) in I-V tracers for PV degradation studies; (ii) or as a diagnostic function in module-integrated converters.

- **New method for quantifying module failures and degradation from EL images.**

A method was developed for quantifying the extent of different failures and degradation modes present in crystalline silicon PV modules from EL images. The method relies on identifying specific failure signatures in EL images, by analyzing the luminescence maps and distributions, as well as applying the fundamental diode model to analyze the distributed solar cell parameters. The method is suitable for automatic analysis and assessment of module quality from EL images, for the purpose of PV module diagnostics and module quality inter-comparison.

- **New model-based PV array condition monitoring method**

The PV array condition monitoring method proposed uses a model-based approach, and is suitable for PV systems where irradiance and module temperature sensors are available. The novelty of the method comes from its ability to (automatically) self-parameterize the performance model from measurements acquired by the PV inverter after the PV system has been commissioned, and does not require a dedicated system modelling effort.

- **New I-V based PV array diagnostic method**

The PV array diagnostic method proposed can operate without ambient sensors, and is based on measuring and analyzing parameters of the light I-V curve of the array. The method can detect the presence of shading, increased series-resistance losses, or PID. Moreover it requires low computation resources and it uses hardware capabilities that are already present in most PV inverters.

- **New MPPT optimization method based on partial shading detection.**

An intelligent MPPT method was developed that monitors the MPP voltage and triggers an I-V sweep only when a partial shadow is detected, therefore minimizing power loss due to repeated I-V sweeps. The proposed system is validated on an advanced, flexible photovoltaic inverter system test platform that is able to reproduce realistic partial shadow conditions, both in simulation and on hardware test system.

1.6 THESIS OUTLINE

This thesis is divided into two main parts. **Part I** contains the report of the work carried out during the PhD project period, while **Part II** contains the relevant articles published throughout the project work. **Part I** is structured into 6 chapters, which are briefly presented in the following:

Chapter 2: Characterization of module power degradation for PID accelerated lifetime testing presents a method for characterizing module power degradation during accelerated PID stress testing, using in-situ dark I-V measurements, and demonstrates its potential for developing accelerated life models for crystalline silicon PV modules undergoing PID. This chapter summarizes the results from Publications I and II.

Chapter 3: Module degradation and failure mode identification based on the light and dark I-V characteristics introduces a PV module diagnostic method for identifying: optical losses, degradation of the electrical circuit, cell cracks and fractures, and PID; based on the analysis of the light and dark I-V characteristics of the PV module. This chapter summarizes the results from Publications VI.

Chapter 4: Module degradation and failure diagnosis using electroluminescence imaging presents a method for quantifying the extent of different failures and degradation modes present in crystalline silicon PV modules. The results of this work were not published at the time of editing this thesis.

Chapter 5: Diagnostic methods and systems for PV plants presents methods for detecting power loss due to shading, increased series resistance, PID. Three practical diagnostic methods are proposed, that can be implemented in a PV Plant, depending on the hardware available. This chapter summarizes the results from Publications VII- XII.

Chapter 6: Conclusions summarizes the work which has been carried out throughout this project, and draws the main conclusions based on the achieved results. The chapter ends with an outlook to further research directions enabled by the work in this thesis.

1.7 LIST OF APPENDED PUBLICATIONS

I. **S. Spataru**, P. Hacke, D. Sera, C. Packard, T. Kerekes and R. Teodorescu. "Temperature-Dependency Analysis and Correction Methods of in-Situ Power-Loss Estimation for Crystalline Silicon Modules Undergoing Potential-Induced Degradation Stress Testing." Progress in Photovoltaics: Research and Applications 23, no. 11 (2015): pp. 1536-1549. DOI: 10.1002/pip.2587.

II. P. Hacke and **S. Spataru**. "Automated Data Collection for Determining Statistical Distributions of Module Power Undergoing Potential-Induced Degradation." Presented at *24th Workshop on Crystalline Silicon Solar Cells & Modules: Materials and Processes*, Breckenridge, Colorado, United States, 2014.

III. **S. Spataru**, D. Sera, T. Kerekes, R. Teodorescu, P. A. Cotfas and D. T. Cotfas. "Experiment Based Teaching of Solar Cell Operation and Characterization Using the Solarlab Platform." In proc. of *Proceedings of the 7th International Workshop on Teaching in Photovoltaics*, vol. 7, 2014.

IV. **S. Spataru**, D. Sera, T. Kerekes and R. Teodorescu. "Teaching Photovoltaic Array Modelling and Characterization Using a Graphical User Interface and a Flash Solar Simulator." In proc. of *Proceedings of the 6th International Workshop on Teaching in Photovoltaics*, vol. 6, pp. 36-44, 2012.

V. **S. Spataru**, P. Cernek and D. Sera. "Characterization of a Crystalline Silicon Photovoltaic System after 15 Years of Operation in Northern Denmark." In proc. of *29th European Photovoltaic Solar Energy Conference and Exhibition*, pp. 2680 - 2688, 2014, DOI: 10.4229/EUPVSEC20142014-5BV.1.31.

VI. **S. Spataru**, D. Sera, P. Hacke, T. Kerekes and R. Teodorescu. "Fault Identification in Crystalline Silicon PV Modules by Complementary Analysis of the Light and Dark Current-Voltage Characteristics." *Progress in Photovoltaics: Research and Applications*, 2015, DOI: 10.1002/pip.2571.

VII. C. Kopacz, **S. Spataru**, D. Sera and T. Kerekes. "Remote and Centralized Monitoring of PV Power Plants." In proc. of *Optimization of Electrical and Electronic Equipment (OPTIM), 2014 International Conference on*, pp. 721-728, 2014, DOI: 10.1109/OPTIM.2014.6851005.

VIII. **S. Spataru**, D. Sera, T. Kerekes and T. Teodorescu. "Photovoltaic Array Condition Monitoring Based on Online Regression of Performance Model." In proc. of *39th IEEE Photovoltaic Specialists Conference* pp. 0815 - 0820, 2013, DOI: 10.1109/PVSC.2013.6744271.

IX. D. Sera, **S. Spataru**, L. Mathe, T. Kerekes and R. Teodorescu. "Sensorless PV Array Diagnostic Method for Residential PV Systems." In proc. of *26th European Photovoltaic Solar Energy Conference and Exhibition*, pp. 3776 - 3782, 2011, DOI: 10.4229/26thEUPVSEC2011-4AV.3.37.

X. **S. Spataru**, D. Sera, T. Kerekes and R. Teodorescu. "Detection of Increased Series Losses in PV Arrays Using Fuzzy Inference Systems." In proc. of *Photovoltaic Specialists Conference (PVSC), 2012 38th IEEE*, pp. 464-469, 2012, DOI: 10.1109/PVSC.2012.6317658.

XI. **S. Spataru**, D. Sera, T. Kerekes and R. Teodorescu. "Diagnostic Method for Photovoltaic Systems Based on Light I-V Measurements." Solar Energy 119, (2015): pp. 29-44. DOI: 10.1016/j.solener.2015.06.020.

XII. **S. Spataru**, A. Amoiridis, R. N. Beres, C. I. Ciontea, T. Klein and D. Sera. "Development of an Intelligent Maximum Power Point Tracker Using an Advanced PV System Test Platform." In proc. of *Photovoltaic Specialists Conference (PVSC), 2013 IEEE 39th*, pp. 2953-2958, 2013, DOI: 10.1109/PVSC.2013.6745084.

1.8 RELATED PUBLICATIONS

The work and results of this thesis have also contributed to other papers related to control, firefighter safety protection, and grid integration of PV systems. However, these papers will not be included in this thesis.

R1. **S. Spataru**, D. Sera, F. Blaabjerg, L. Mathe, T. Kerekes, S. Spataru, D. Sera, F. Blaabjerg, L. Mathe and T. Kerekes. "Firefighter Safety for PV Systems: Overview of Future Requirements and Protection Systems." In proc. of *Proceedings of the IEEE Energy Conversion Congress and Exposition, ECCE 2013*, pp. 4468-4475, 2013, DOI: 10.1109/ECCE.2013.6647298.

R2. L. Mathe, D. Sera, **S. Spataru**, C. Kopacz, F. Blaabjerg and T. Kerekes. "Firefighter Safety for PV Systems: A Solution for the Protection of Emergency Responders from Hazardous dc Voltage." IEEE Industry Applications Magazine 21, no. 3 (2015): pp. 75-84. DOI: 10.1109/MIAS.2014.2345834.

R3. D. Sera, L. Mathe, T. Kerekes, **S. Spataru** and R. Teodorescu. "On the Perturb-and-Observe and Incremental Conductance MPPT Methods for PV Systems." *IEEE Journal of Photovoltaics* 3, no. 3 (2013): pp. 1070-1078, DOI: 10.1109/JPHOTOV.2013.2261118.

R4. B.-I. Craciun, **S. Spataru**, T. Kerekes, D. Sera and R. Teodorescu. "Power Ramp Limitation and Frequency Support in Large Scale PVPPs without Storage." In proc. of *Proceedings of the 2013 39th IEEE Photovoltaic Specialists Conference (PVSC)*, pp. 2354-2359, 2013, DOI: 10.1109/PVSC.2013.6744947.

R5. B.-I. Craciun, **S. Spataru**, T. Kerekes, D. Sera and R. Teodorescu. "Internal Active Power Reserve Management in Large Scale PV Power Plants." Presented at *4th International Workshop on Integration of Solar into Power Systems*, Berlin, Germany, 2014.

CHAPTER 2 CHARACTERIZATION OF MODULE POWER DEGRADATION FOR PID ACCELERATED LIFETIME TESTING

This chapter presents a method for characterizing module power degradation during accelerated PID stress testing, using in-situ dark I-V measurements, and demonstrates its potential for developing accelerated life models for crystalline silicon PV modules undergoing PID.

2.1 INTRODUCTION

The first part of this chapter introduces a method for characterizing module power degradation during accelerated PID stress testing, using *in-situ* dark I-V measurements. The original method was first proposed by Hacke et al. in [60], and is based on in-situ dark I-V characterization of the modules at 25°C, during the PID stress test. This in-situ characterization method was a significant improvement over intermittently removing the modules from chamber and measuring power on a solar simulator, which can require considerable time and effort when numerous samples are involved [60]. However some issues were still open in regards to interrupting the stress and ramping the module temperature down to 25°C.

Publication I addresses these issues, building upon this method, and proposing an automated solution for the characterization process. Moreover, it presents a method for estimating the module STC performance degradation, from dark I-V measurements acquired directly at the stress temperature, avoiding temperature transients and test interrupts. These two proposed procedures improve the data collection process, and reduce module PID stress testing time.

In addition to the possibility of the semi-continuous monitoring of the module degradation during the accelerated stress test, the power degradation data collected using this method, can be used to develop *acceleration models* to relate the main PID stress factors: temperature, voltage, and humidity, to time acceleration, and thus be able to predict the lifetime of the modules at use (field) conditions. This approach was followed in Publication II, where a PID temperature acceleration model was developed for crystalline silicon PV modules, based on the Arrhenius model.

2.2 IN-SITU CHARACTERIZATION OF MODULE POWER DEGRADATION FOR PID ACCELERATED STRESS TESTING

2.2.1 METHODOLOGY FOR IN-SITU CHARACTERIZATION OF MODULE POWER DEGRADATION AT 25 ºC

The in-situ characterization method, proposed in [60], was developed for determining the STC performance degradation of crystalline PV modules undergoing accelerated PID stress testing, by environmental chamber testing, where elevated damp-heat stress and module nameplate system voltage bias are applied to the modules continuously. The method proposes to monitors the dark I-V characteristic of the test modules semi-continuously, and by applying the I-V curve superposition principle [101, 102], it translates the 25°C dark I-V curve to the first quadrant, to recreate the 25°C light I-V curve. The translation is done by a current I_L, usually set as the average short-circuit current (I_{sc}) of the module [60], measured on a flash tester at 25°C and at the desired irradiance (usually 1000 W/m^2), before and after the PID stress test [70]. Consequently, the 25°C P_{max} degradation of the module $P_{deg}(t, 25°C)$, can be calculated for any time step t and irradiance level, by applying the superposition principle as in (2.1).

$$P_{\deg}(t,25°C)=\frac{P_{\max}(t,25°C)}{P_{\max}(t_0,25°C)}=\frac{\max\left\{\left[I_{dark}\left(t,25°C\right)+I_L\right]\mathrm{V}_{dark}\left(t,25°C\right)\right\}}{\max\left\{\left[I_{dark}\left(t_0,25°C\right)+I_L\right]\mathrm{V}_{dark}\left(t_0,25°C\right)\right\}} \quad (2.1)$$

Where $I_{dark}(t, 25°C)$ and $V_{dark}(t, 25°C)$ are the current and voltage components of the 25°C dark I-V curve, measured at time step t, whereas I_L sets the desired photocurrent/irradiance.

Using this method to determine the performance degradation of the module from 25°C dark I-V measurements taken during the PID stress test, has been shown to correspond excellently with the performance degradation measured by the solar simulator, for up to about 30% relative P_{max} degradation [70].

The solar cell I-V curve superposition principle, on which this method is based, has been shown to work well for most crystalline *pn* single-junctions [101, 102]. Nevertheless, there are some cases when the superposition principle may no longer apply; the most notably of which is for solar cells exhibiting a significant series resistance (R_s>10 Ωcm^2) [37, 102-104], however PID is usually not associated with increased series resistance [60].

Other limitations of the superposition principle are specific to: (i) high-efficiency solar cells with oxidized surfaces [105], (ii) solar cells with significant recombination and generation in the depletion region [102, 104, 106], (iii) or solar cells with voltage dependence of the depletion-region width [102, 104]. As a best practice, the validity

of the superposition principle should be tested, when applying the in-situ degradation characterization method to new module designs. This can easily be achieved by performing pre- and post-experiment light I-V and dark I-V measurements on the modules, and comparing the relative P_{max} degradation in the two cases [60].

2.2.2 PROPOSED METHODOLOGY FOR IN-SITU CHARACTERIZATION OF MODULE POWER DEGRADATION AT STRESS TEMPERATURE

The in-situ characterization method for determining the performance degradation of module undergoing PID stress testing, proposed in [60], and briefly described in the previous subchapter, requires periodic ramping down of the environmental chamber/module temperature to 25°C for dark I-V characterization of the PV modules being tested. This introduces module temperature and humidity transients which may be difficult to quantify in the degradation dynamics of the module, as well as lengthens the test time with each temperature ramp down.

These issues were addressed in Publication I where a method was developed for characterizing the performance degradation of the modules, directly at the elevated stress temperature, avoiding temperature transients and test interrupts, as well as improving the data collection process, and reducing testing time.

The new module degradation characterization method was developed upon the in-situ characterization method proposed in [60]. In the first stage the in-situ characterization method was fully automatized using the test setup shown in Figure 2.1, which was developed in collaboration with the PV Performance and Reliability Research Group at the National Renewable Energy Laboratory.

The test setup in Figure 2.1 is able to run a pre-programmed experiment profile for accelerated PID stress testing of PV modules, by environmental chamber testing with applied high voltage bias. Moreover, it is capable of monitoring the temperature and leakage currents of up to eight test modules, as well acquire dark I-V measurements for each module, at pre-programmed time intervals and temperature levels. Automatizing the test and in-situ characterization of the modules can greatly reduce the effort of the operator to monitor and characterize the modules, as well as allow for a much more granular characterization of the PV modules as they degrade.

Although the test equipment is capable of automatically ramping down the chamber/module temperature and acquire dark I-V measurements at 25ºC for estimating the module degradation, our goal was to develop a method for characterizing the module performance degradation that does not require interrupting the stress by having to ramp down the module temperature. This requires understanding the temperature dependency of the P_{max} degradation of modules undergoing PID.

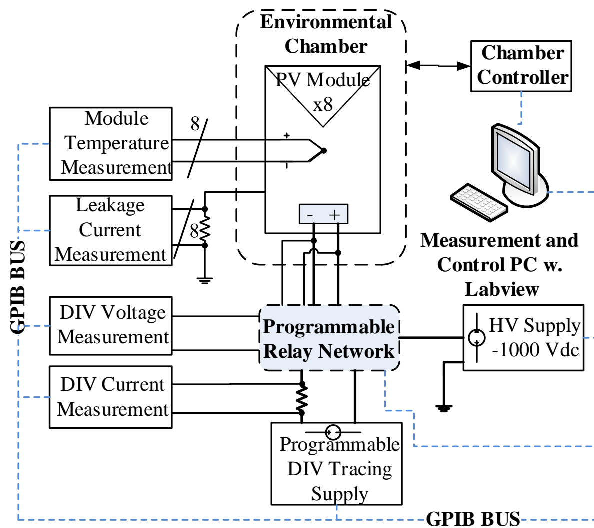

Figure 2.1: Fully automated experiment setup for performing damp-heat with system-voltage stress testing on PV modules.

For this purpose the experiment profile shown in Figure 2.2 was implemented and performed with the automated test setup in Figure 2.1. In this experiment, five crystalline module designs (denoted from A to E), with two replicates each, underwent damp-heat stress testing at 60ºC and 85% RH, with negative voltage bias (-1000 V) applied between the active material (shorted leads) and the frame of each module. Every three hours, the dark I-V characteristic of each module was acquired at 60º, 50º, 40º, 30º, and 25ºC by automatically ramping down the chamber temperature and RH. The temperature of each module was monitored by the test system, until it reached the desired set points, and the dark I-V characteristics were measured.

The dark I-V measurements acquired on the ramp-down of the module temperature were approximately matched with those acquired on the ramp-up, showing negligible influence of the ramps on the module degradation.

Moreover, the experiment profile and chamber control were significantly optimized to keep the temperature transients short in duration. Once all measurement points at the specified temperature are taken, the stress test is resumed automatically according to the profile in Figure 2.2. In addition, STC I-V measurements were acquired pre- and post-experiment/degradation, for every module using a flash tester. The resulting pre- and post-degradation STC I_{sc} values were used to check the assumptions that the photo-generated current of a PV module does not change significantly due to PID, as previously observed [52, 70, 107].

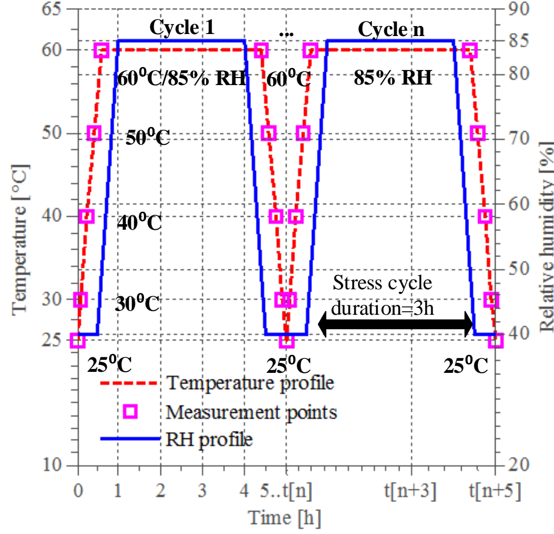

Figure 2.2: Chamber temperature and relative humidity profiles for performing damp-heat (60ºC/85% RH) with system voltage stress testing (-1000 V). At the start and end of each cycle, the dark I-V characteristic curves of the PV module samples are measured automatically at (60º, 50º, 40º, 30º, and 25ºC).

Figure 2.3 shows the relative P_{max} degradation curves $P_{max}(t, T)/P_{max}(t_0)$ for the ten modules undergoing PID, both at 25ºC and 60ºC. To validate the in-situ degradation characterization method and check if the superposition principle holds, the final P_{max} degradation values for each module, calculated from the 25ºC dark I-V characteristics, shown as solid lines in Figure 2.3, were compared with the actual power degradation, displayed as star markers in Figure 2.3, and measured using a flash tester.

Furthermore, from Figure 2.3 we can observe that the final values of 25ºC measured P_{max} degradation match very well. However, the P_{max} degradation, calculated from the 60ºC dark I-V curves, displayed with dashed lines in Figure 2.3, underestimates the power degradation by several percent, which was consistent for each module tested.

This difference is quantified in (2.2) by calculating the power-loss estimation error (δP_{deg}) as a relative percentage error between the $\underline{P_{max}}$ degradation determined at stress temperature T_{stress}, and the module degradation determined at 25ºC.

$$\partial P_{\deg}[\%] = \frac{P_{\deg}(t, T_{stress}) - P_{\deg}(t, 25\ ^{\circ}C)}{P_{\deg}(t, 25^{\circ}C)} * 100 \tag{2.2}$$

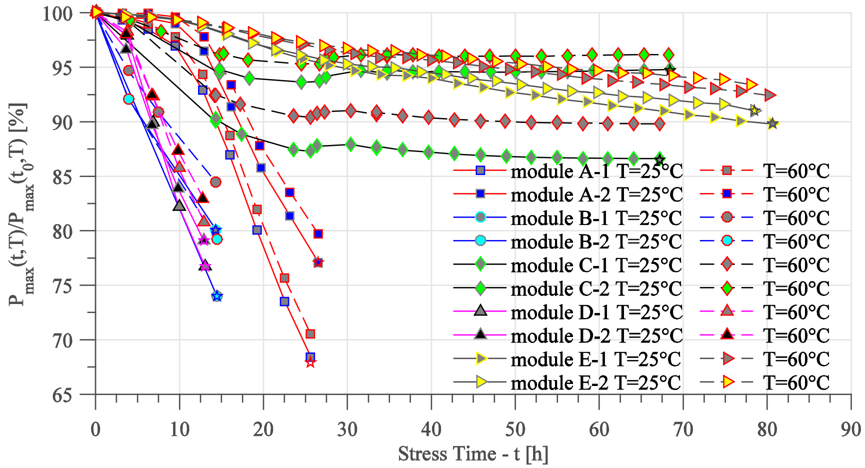

Figure 2.3: Maximum power (P_{max}) degradation curves calculated from the dark I-V measurements at 25ºC, solid lines; and 60ºC, dashed lines, for PV modules undergoing potential-induced degradation stress testing. Each P_{max} on the y axis is normalized to the P_{max} measured before the start of degradation at the same temperature (either 25ºC or 60ºC). The final degradation levels are validated using light I-V measurements at the finish of the experiment, and plotted as star symbols on the graph (matching the degradation levels estimated from the 25ºC dark I-Vs – full lines).

By plotting δP_{deg} for the stress temperature of 60ºC, as shown in Figure 2.4, it can be noticed that the power-loss estimation error is present for all module tested, progresses in magnitude as modules degrade, and is more significant for dark I-V measured at higher temperatures, as detailed in Publication I.

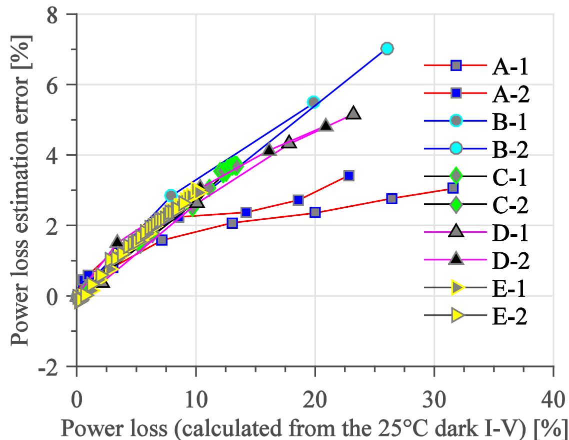

Figure 2.4: Relative power-loss estimation error δP_{deg} (at 60ºC) as a function of degradation level (calculated from the dark I-Vs measured at 25ºC) for all modules considered in the experiment.

If the module performance degradation measured at stress temperature is to be used for degradation modelling [108], acceleration-factor determination [109], or accelerated lifetime modeling [60] of crystalline PV modules in regards to PID, it is preferable to determine the STC P_{max} degradation curves as accurately as possible. In this regard, two existing P_{max} temperature-correction methods were investigated in detail in Publication I, where their applicability and limitations are discussed. As an alternative, a new *error compensation* method was proposed, that is more accurate and easier to apply for the case of PID being evaluated in-situ at test temperature.

To demonstrate this method, a relative estimation error $d(t_k, T_{stress})$ is calculated in (2.3) for a measurement point t_k during the PID test, as the difference between the dark I-V-determined P_{max} degradation, measured at T_{stress}, and the “real” degradation, namely P_{max} degradation measured at 25ºC (either by dark I-V or light I-V, equivalently).

$$d(t_k, T_{stress}) = P_{deg}(t_k, T_{stress}) - P_{deg}(t_k, 25\ °C) = \frac{P_{max}(t_k, T_{stress})}{P_{max}(t_0, T_{stress})} - \frac{P_{max}(t_k, 25\ °C)}{P_{max}(t_0, 25\ °C)} \quad (2.3)$$

The error curve $d(t_k, T_{stress})$, plotted in Figure 2.5 (red curve) for module D-1, is specific for each module and stress temperature, and depends on the degradation level of the module. Because the real error curve cannot be measured directly during the PID stress test (which would require ramping down the chamber/module temperature to 25ºC), it can be approximated with the linear relationship $\hat{d}(t_k, T_{stress})$ as in (2.4), assuming a linear dependence between the error d and the P_{max} degradation measured at stress temperature.

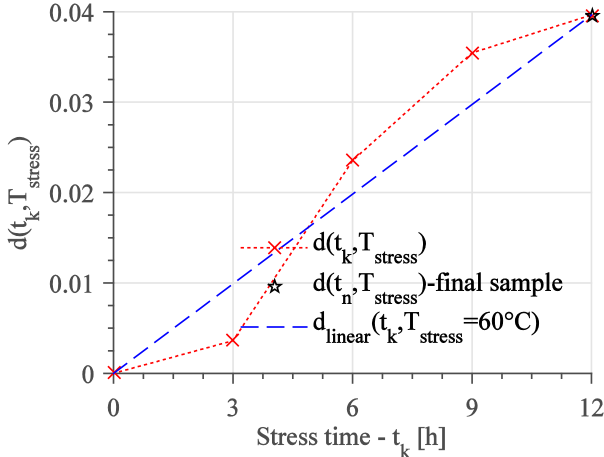

Figure 2.5: Example of the P_{max} degradation estimation error d, measured at a stress temperature of 60ºC for module D-1. The red curve represents the measured error (relative to the 25ºC reference measurement); the blue curve represents the linear approximation of the error, resulting from fitting the initial and final values of the measured error.

The linear relationship $\hat{d}(t_k, T_{stress})$ in (2.4) consists of a proportion (or slope) m and an intercept b that can be easily calculated from two points of the real error curve $d(t_k, T_{stress})$.

$$\hat{d}(t_k, T_{stress}) = mP_{\deg}(t_k, T_{stress}) + b = \frac{d(t_n, T_{stress})}{P_{\deg}(t_n, T_{stress}) - 1}\left[P_{\deg}(t_k, T_{stress}) - 1\right] \quad (2.4)$$

If we consider t_0 to be the initial measurement point, before the degradation of the module starts, then the degradation estimation error becomes $d(t_0, T_{stress}) = 0$, and the P_{max} degradation measured at T_{stress} becomes $P_{deg}(t_0, T_{stress}) = 1$. Similarly, t_n will be the final measurement point, acquired at the end of the PID stress test, when the P_{max} degradation is measured at both T_{stress} and at 25ºC. From these two measurement points (t_0 and t_n) for which both $d(t_{0,n}, T_{stress})$ and $P_{deg}(t_{0,n}, T_{stress})$ are known, the parameters of the linear approximation function $\hat{d}(t_k, T_{stress})$ can be easily calculated as in (2.4). An example of this approximation function is plotted in Figure 2.5 (blue curve) for module D-1.

Finally, correcting the P_{max} degradation to 25ºC conditions, $\hat{P}_{deg}(t_k, 25°C)$, at any measurement point t_k during the PID test becomes straightforward by replacing $d(t_k, T_{stress})$ in (2.3) with its linear approximation $\hat{d}(t_k, T_{stress})$, and rearranging it as in (2.5). Results of the corrected P_{max} degradation, compared to 25ºC and 60ºC, are shown in Figure 2.6 for module D-1. From here it can be observed that the corrected P_{max} degradation curve matches the 25ºC measured degradation curve very well.

$$\hat{P}_{\deg}(t_k, 25^o\,C) = P_{\deg}(t_k, T_{stress}) - d(t_n, T_{stress})\left[P_{\deg}(t_k, T_{stress}) - 1\right] / \left[P_{\deg}(t_n, T_{stress}) - 1\right] \quad (2.5)$$

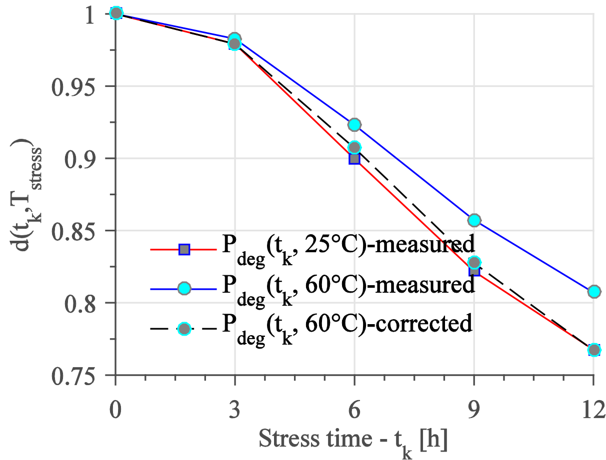

Figure 2.6: Example of the error compensation method, for translating P_{max} degradation for module D-1, measured at a stress temperature of 60ºC to 25ºC conditions.

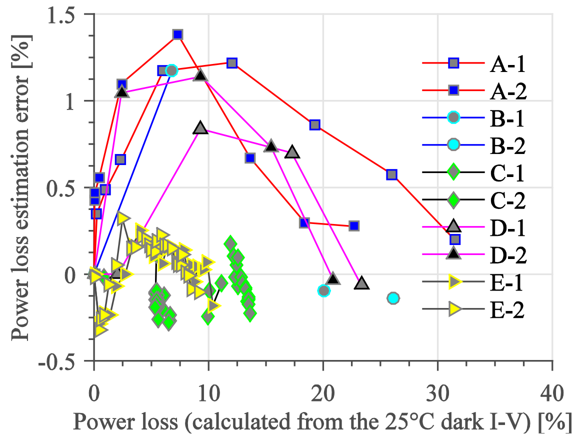

Figure 2.7: Power-loss estimation error δP_{deg} (from 60ºC to 25ºC), calculated for all PV modules, after the error compensation.

To validate the method and quantify its performance, the 60ºC P_{max} degradation curves for all PV module test samples are corrected to 25ºC conditions, and the power-loss estimation error, calculated as in (2.2), is plotted in Figure 2.7. This figure shows that the power-loss estimation error is significantly reduced after applying the error compensation method, as compared to the initial errors in estimating the power-loss, shown in Figure 2.4.

From a practical perspective, implementing the in-situ characterization of module power degradation directly at stress temperature would achieve cost reductions, since it requires simpler test hardware and less laboratory personnel effort and would lead to more rapid and greater accumulation of statistical data for future application of various statistical reliability models. An application of this method for developing an accelerated life model for modules undergoing PID is presented in the next subchapter.

2.3 ACCELERATED LIFE TESTS AND MODELLING OF CRYSTALLINE SILICON PV MODULE UNDERGOING PID

Since nowadays PV modules are expected to have a service lifetime of 25+ years, it is impractical to wait 25 years in order to assess the reliability in regard to PID (or other failures) of new module designs. Accelerated PID stress tests as those proposed in the IEC 62804 draft, and described in the previous subchapters can be used to reduce testing time and obtain module reliability data more quickly. However, it is also necessary to develop appropriate *acceleration models* to relate the main PID stress factors: temperature, voltage, and humidity, to time acceleration, and thus be able to predict the lifetime of the modules at use (field) conditions [110].

Typically, if the stress factors and the failure mechanisms are well understood, physical acceleration models can be developed that describe the failure-causing process over the range of the stress test conditions and that can provide extrapolation to use conditions [110].

This approach was followed in Publication II, where a PID temperature acceleration model was developed for crystalline silicon PV modules, using the in-situ power-loss characterization method, described in the previous subchapters. The PID temperature acceleration model was developed based on the well-known Arrhenius model, shown in (2.6):

$$TTF = A_0 \exp\left(\frac{E_a}{kT}\right) \tag{2.6}$$

Where: TTF is the time-to-failure, E_a is the activation energy, k is Boltzmann's constant, T is the temperature, and A_0 is a scaling factor [110].

The goal of developing such a temperature acceleration model is to determine the activation energy E_a of the temperature dependent failure processes, for a given: (i) module design; (ii) soft failure criteria (1%, 5%, or 20% STC P_{max} power loss for example); (iii) constant high voltage bias and polarity; (iv) constant humidity. Once the activation energy is known, the TTF of the modules can be determined for lower use temperatures, by using (2.6) if the scaling factor A_0 is known. Alternatively, the Arrhenius model can be rewritten as in (2.7) to translate the time to failure TTF_1 determined at a high temperature level T_1, to the use temperature T_2.

$$TTF_2 = TTF_1 \exp\left[\frac{E_a}{k}\left(\frac{1}{T_2} - \frac{1}{T_1}\right)\right] \tag{2.7}$$

This procedure was demonstrated on crystalline silicon PV modules undergoing PID at 85% RH and 60°C, 72°C, and 85°C, and -1000 V applied voltage bias, which is described in detail in Publication II. Five module replicas were tested at each temperature stress level, for which the STC P_{max} degradation was determined from dark I-V measurements, taken every four hours at stress temperature, and using the methodology presented in the previous subchapter and detailed in Publication I. The resulting STC P_{max} degradation curves are summarized in Figure 2.8.

Figure 2.8 shows the effect of temperature on modules undergoing PID, as well as slight differences between the degradation characteristics for module replicas at the same temperature level, due to the random characteristics of the modules. The error introduced by this random effect can be reduced by increasing the number of test modules for each temperature level, and applying appropriate statistical methods in determining the Arrhenius model parameters.

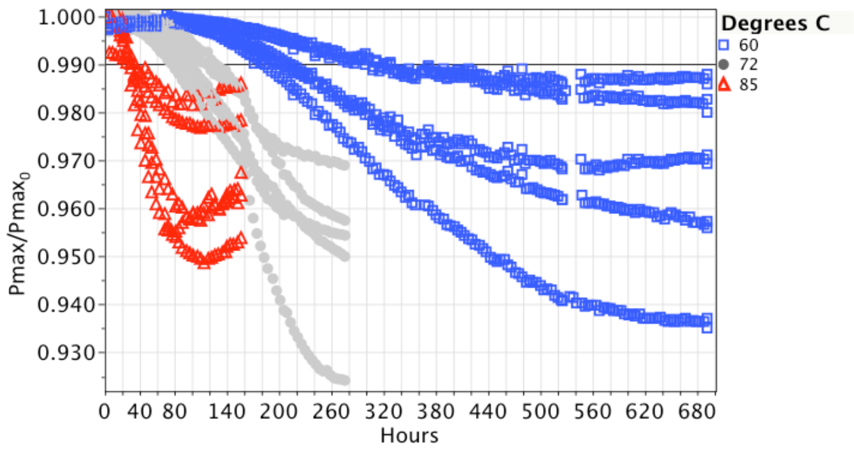

Figure 2.8: Normalized STC power of PV modules undergoing PID at 85% RH, -1000 V bias, and at three temperatures indicated on the plot. The data were obtained semi-continuously at the stress temperature.

Secondly, we can notice in Figure 2.8 that not all module replicas reach the same degradation levels, as a consequence a 1% STC P_{max} degradation level (0.99 relative power remaining) has been chosen as the failure criterion. For other module designs, which are more PID-prone, and degrade more, a higher STC P_{max} degradation level (e.g. 5% or 20%) can be imposed as the failure criterion, as was done in [60, 109].

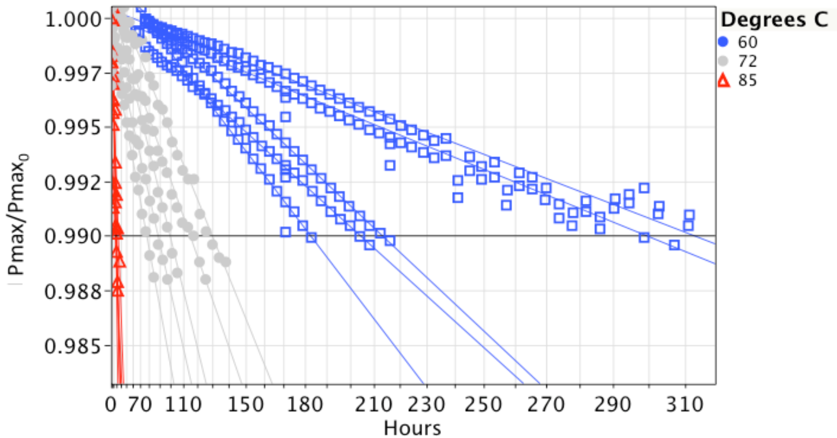

Figure 2.9: Subset of the normalized STC power of PV modules undergoing PID at 85% RH, -1000 V bias, and at three temperatures indicated on the plot. The data are successfully fit linearly with the time (h) scaled to the power of two, and the intersection in time of the curves at the failure criterion of 0.99 relative power remaining can be seen.

Once the failure criterion has been set, the next step is to determine the *TTF* for each module, as the time at which the STC P_{max} of each module decreases by 1%, as shown in Figure 2.9. Here it is abundantly clear why it is necessary to accurately measure the STC P_{max} degradation characteristic of each module, as well as have sufficient granularity/resolution in the measured data.

The resulting *TTF* values are typically assumed to have a lognormal distribution. Consequently, the logarithms of the *TTF* values are calculated, and used to compute the mean-time-to-failure (MTTF) of the modules at each temperature level [111]. Next, the activation energy is determined from (2.6), given the three temperature levels of 60°C, 72°C, and 85°C, and the corresponding MTTF values, resulting in 0.85 eV for this specific case. This value can then be used together with (2.7) to determine the MTTF of the modules at 25°C use temperature, 85% RH, and -1000 V voltage bias, resulting in approximately 8000 hours before the module STC P_{max} degrades by 1% due to PID.

Alternatively, the *TTF* for each sample in each temperature category can plotted on an Arrhenius scale, as shown in Figure 2.10. The points in each temperature category are shown with the computed lognormal distribution. The Arrhenius fitting curve and 95% confidence intervals are shown to either side of it. The curve can be extended to 25°C along with a computed lognormal distribution to estimate the MTTF at that temperature. However, the 8000 hours MTTF obtained with both methods, for the 25°C, 85% RH, and -1000 V voltage stress, must be considered in view that the actual field conditions are non-constant.

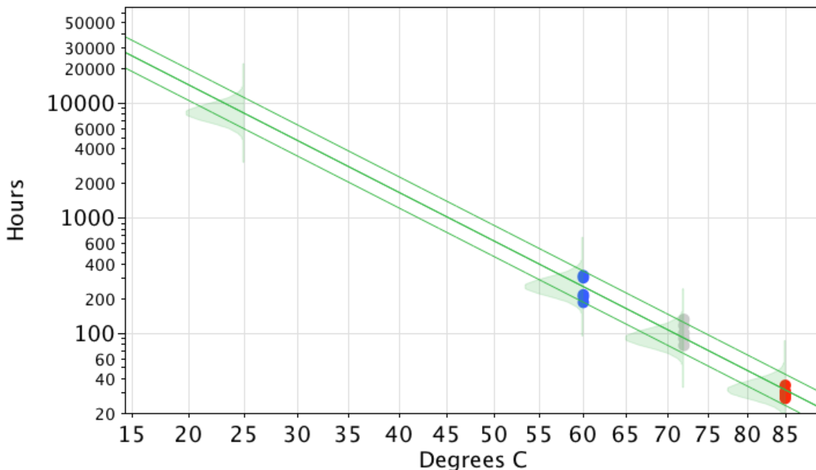

Figure 2.10: Three point Arrhenius fit to the lifetime data with activation energy 0.85 eV. 95% confidence intervals are shown to either side of the Arrhenius fit. Lognormal distributions are shown around the data points and the analysis is extended to a hypothetical 25°C use condition as an example.

Other limitations to be considered are that these accelerated tests were performed in the dark, whereas illumination, especially the UV component, is found to mitigate PID to an extent [67]. Moreover, if the humidity factor is removed (such as on a sunny day with low humidity), a stress factor is removed, in which case modules have been shown to recover to an extent by thermal activation [52]. On the other hand, relative humidity and temperature can for some periods be higher than 85% RH and 85°C.

The technique shown here can be used to evaluate the time-to-failure of various module types on a relative basis, but additional real-world factors such as illumination and PID degradation inclusive of recovery phenomena may be introduced. Moreover, this technique can be used to model other PID stress factors such as voltage and humidity with the associated failure mechanisms, and eventually integrated into a multi-stress acceleration model [110]. Such a model could be used to estimate the MTTF of modules for different local climates and operation conditions.

The in-situ characterization technique may also be extended to analyze MTTF of modules in relation with other degradation modes, such as mechanical degradation of the cells and interconnects due to mechanical loading and/or thermal cycling.

2.4 SUMMARY AND CONCLUSIONS

This chapter introduced an in-situ module power degradation monitoring method for crystalline silicon PV modules undergoing PID stress testing, and discussed its advantages and limitations. A solution for automatizing the in-situ monitoring method was proposed, and used to investigate the effects of PID on the power degradation estimation from dark I-V measurements taken at different temperatures. Based on this investigation, a method was proposed on how to compensate these temperature effects, and characterize module power degradation directly at stress temperature, thus avoiding temperature transients and test interrupts. Moreover, from a practical perspective, implementing the in-situ characterization of module power degradation directly at stress temperature would achieve cost reductions, since it requires simpler test hardware and less laboratory personnel effort and would lead to more rapid and greater accumulation of statistical data for future application of various statistical reliability models.

These advantages and the potential of the method were demonstrated in the last part of this chapter, where we showed how the performance degradation data collected using this method, can be used to develop acceleration models to relate the main PID stress factors, to time acceleration, and thus be able to predict the lifetime of the modules at use (field) conditions. This was exemplified for developing a PID temperature acceleration model for crystalline silicon PV modules, based on the Arrhenius equations. However the same approach could be applied to model voltage and humidity acceleration.

CHAPTER 3 MODULE DEGRADATION AND FAILURE MODE IDENTIFICATION BASED ON THE LIGHT AND DARK I-V CHARACTERISTICS

This chapter introduces a PV module diagnostic method for identifying: optical losses, degradation of the electrical circuit, cell cracks and fractures, and PID; based on the analysis of the light and dark I-V characteristics of the PV module.

3.1 INTRODUCTION

This chapter proposes a PV module diagnostic method that can identify the four degradation and failure modes described in Chapter 1, namely: (i) optical losses and degradation, (ii) degradation of the electrical circuit of the PV module, (iii) mechanical degradation of the solar cells, (iv) PID of the solar cells.

The method is based on the complementary analysis of the light and dark I-V characteristics of the PV module and has several advantages over traditional failure identification methods. First, the computational requirements of the method are low, and it does not suffer from solar cell modelling and curve fitting limitations, rendering the method machine analysis friendly.

Second, the method can be used as a laboratory diagnostic tool for PV modules, in the detection of damaged ribbon interconnects, cell microcracks, fractures, or incipient PID, without the need of thermal IR or EL imaging.

Third, the method has potential for implementation in I-V tracers for long-term reliability monitoring of PV modules, with the goal of identifying the onset and progression of the different degradation modes, without the need of periodic inspection and imaging. Another possible field application would be in module-integrated converters capable of bidirectional current flow, where the method can be used to optimize maintenance operations by scheduling appropriate actions based on the severity and type of degradation affecting the PV modules.

The proposed failure identification methodology and experimental validation are shortly described next. A more detailed explanation of the method and experiments are presented in Publication VI.

3.2 PROPOSED METHODOLOGY FOR IDENTIFYING DEGRADATION AND FAILURES IN CRYSTALLINE SILICON PV MODULES

The premise of the diagnostic method is that different degradation modes affect the light and dark I-V characteristics of the PV module in different ways, leaving distinct signatures. Table 3-1 summarizes some of the potential signatures for the four degradation modes investigated in this work.

Table 3-1: Summary of main signatures for the four degradation modes investigated

Degradation mode	Degradation signature
Optical losses and degradation	Decreased current generation (I_{sc}) [23] Distortion of the I-V curve (if bypass diodes are installed and activated) [24, 25]
Degradation of the electrical circuit	Increase in series resistance (R_s) [29, 30] [32]
Mechanical degradation of the solar cells	Decreased current generation (I_{sc}) [43, 44] Increase in series resistance (R_s) [43, 44] Shunting losses (decreased R_{sh}) [49] Increased recombination losses (J_{02}) [48]
Potential-induced degradation of the solar cells	Shunting losses (R_{sh}) [52, 54, 55] Increased recombination losses (J_{02}) [60, 61]

Starting from this premise, we propose to identify these four degradation modes by detecting and quantifying these specific signatures from light and dark I-V measurements. This is done by taking advance of the intrinsic diagnostic capabilities of light and dark I-V characterization. On one hand, light I-V measurements are excellent at characterizing the current generation and total series resistance of the PV module. Whereas dark I-V measurements are superior in characterizing the diode properties of the solar cells within the module.

Based on this idea we developed several *diagnostic parameters* to quantify the different degradation signatures. These diagnostic parameters are grouped in three categories depending on their purpose: (i) to separate optical losses from electrical degradation, (ii) to characterize increases in the series resistance of the PV module, (iii) to characterize increased shunting and recombination processes in PV module. When all these parameters are analyzed together they can pinpoint which of the four degradation modes is affecting the PV module.

3.2.1 SEPARATING OPTICAL LOSSES FROM ELECTRICAL DEGRADATION

The first step of the diagnostic method is to separate optical losses and degradation of the optical layer from the degradation of the solar cells and electrical components of the module. This is an important step in the diagnostic process because optical factors can be a significant source of error when (automatically) monitoring or measuring electrical parameters of the PV module, such as series resistance.

This case is exemplified in Figure 3.1, in which a 72-cell multicrystalline silicon PV module with bypass diodes is affected by two generic types of shading, generated by covering parts of the module with semi-transparent foils.

In the first case, depicted by the blue curve in Figure 3.1, the shading has a homogenous/uniform impact on the light I-V curve, similar to soiling of the module front-glass, EVA discoloration, or other shading cases when the bypass diodes do not activate (or are not installed). The second case, depicted by the orange and green curves in Figure 3.1, show a heterogeneous/partial impact on the light I-V due to the activation of the bypass diodes, which generate inflection points in the I-V curve.

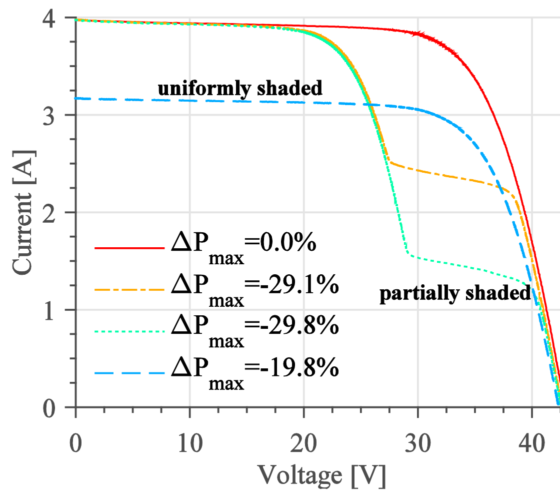

Figure 3.1: Light I-V characteristics of a crystalline silicon PV module with bypass diodes, affected by uniform shading (blue curve) – where the entire module covered with 1 layer of semi-transparent foil; and by partial shading – where only 2 cells were covered once with 2 layers of foil (orange curve), and once with 4 layers of foil (green curve).

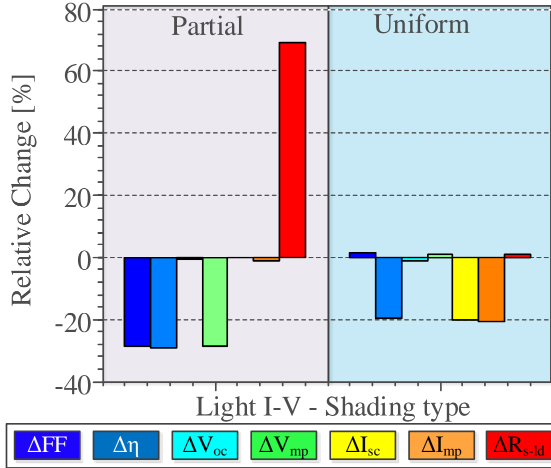

Figure 3.2: Effects of partial (2 cells covered with 2 layers of semi-transparent foil) and uniform (100% module area covered with 1 layer of foil) shading on the light I-V parameters of a PV module with bypass diodes. The initial STC I-V parameters of the module were FF_0 =0.7, η_0=10.95 %, V_{oc0}=42.87 V, V_{mp0}=33.21 V, I_{sc0} = 3.97 A, I_{mp0}=3.62 A, $R_{s\text{-}ld0}$=1.82 Ωcm².

This is not a big issue when the I-V measurements are performed by expert personnel, however this can be a problem when automatically characterizing a large number of modules, or when monitoring the I-V parameters of modules in the field.

Separating optical losses from electrical degradation of the module, starts from the assumption that optical losses and degradation only affect the light I-V characteristic of the module, prompting changes in the MPP and *FF* of the module, as well as possibly other I-V curve parameters such I_{sc} and V_{oc}.

This assumption is valid for most incipient cases of optical losses and degradation, nevertheless, in time, some of these cases, such as localized soiling or delamination, can lead to hot-spots, moisture ingress and corrosion, electrical failures and degradation. In this situation, we consider the degradation to be of electrical nature.

Subsequently, electrical degradation of the module will affect both the light and dark I-V characteristic of the module. Therefore, to quantify changes in the dark I-V characteristic of the module, analogously to the light I-V curve, we use a dark I-V equivalent for the fill factor (FF_{dark}) calculated as shown in Figure 3.3:

In this case, $V_{d\text{-}max}$, calculated as the voltage at I_L=I_{sc}, is the dark I-V equivalent of the V_{oc}. Whereas, (V_p, I_p) is the dark I-V equivalent of the MPP, determined by translating the dark I-V curve to the first quadrant, by superposition with I_L, and calculating the maximum power point of the superimposed dark I-V curve.

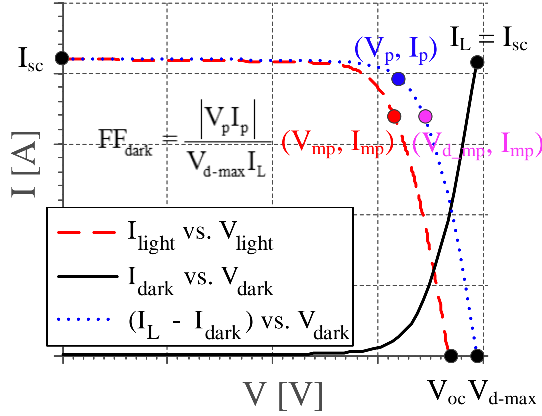

Figure 3.3: Method for calculating diagnostic parameters (FF_{dark}, $V_{d\text{-}max}$, V_p) from the high voltage/current region of the dark I-V.

If the nature of the degradation or failure mode has been identified as optical electrical, the next step is to identify other degradation signatures that can help pinpoint the specific type of electrical degradation.

3.2.2 CHARACTERIZING INCREASED SERIES RESISTANCE OF THE PV MODULE

One such degradation signature is the increase in the PV module's series resistance. This can occur both through the degradation of the module's electrical circuit [34], as well as through mechanical degradation of the solar cells [43, 44]. Due to the distributed nature of the PV module's series resistance, small increases in this parameters are best captured by combining a high-illumination light I-V measurement with a low-illumination [34] or dark I-V measurements [35, 112]. Such a diagnostic parameter that can accurately quantify the total series resistance of the module, is the *light-dark* series resistance ($R_{s\text{-}ld}$), calculated from a light and dark I-V curve, as shown in (3.1) [35, 112]:

$$R_{s-ld} = \left. \frac{V_{d-mp} - V_{mp}}{\mathrm{I}_{mp}} \right|_{|I_{dark}| = I_{sc} - I_{mp}} \tag{3.1}$$

Here, V_{mp} and I_{mp} are the voltage and current at the MPP on the light I-V curve, whereas $V_{d\text{-}mp}$ is the voltage corresponding to $I_{dark}=I_{sc}\text{-}I_{mp}$ on the dark I-V curve, as shown in Figure 3.3.

3.2.3 CHARACTERIZING INCREASED SHUNTING AND RECOMBINATION IN THE PV MODULE

Increased shunting and recombination are associated with increased leakage (loss) currents bypassing the *pn* junction of the solar cell, caused by PID, mechanical degradation of the solar cells, or other mechanisms, as discussed in more detail in Publication VI. A common method for identifying this type of degradation is by curve fitting the I-V characteristic to a diode model, and analyzing the underlying model parameters. This approach can be very successful when investigating the degradation modes of solar cells, however, as previously discussed, this method has a limited applicability to machine analysis and modules with mismatched solar cell I-V characteristics.

We proposed instead a more practical approach, and seek to identity these degradation signatures directly from the dark I-V characteristic. To achieve this, we start from the simplified electrical model of a solar cell without any parasitic resistances (R_s, R_{sh}) under dark conditions, as shown in (3.2):

$$\ln(J) = \frac{q}{nkT}V + \ln(J_0) \tag{3.2}$$

Where J is the current density; V is the terminal voltage; J_0 is the diode saturation current density; n is the diode ideality factor; T is the cell temperature; k is the Boltzmann constant; and q is the elementary charge.

This simplified model is often used to estimate the saturation current $J_0(V)$ and ideality factor $n(V)$ characteristics of solar cells with low parasitic resistances [113]. Most commonly, the $n(V)$ characteristics have been studied to identify changes in the diode quality factor. Less commonly, the $J_0(V)$ term has been studied, however $J_0(V)$ can capture changes in both the magnitude and type of recombination; as well as provide a much more sensitive indicator of all types of changes, increasing with both higher diode quality factor and with parasitic resistances.

If we limit the $J_0(V)$ curve analysis to the low current region of the dark I-V curve, series resistance effects are small, as shown in Publication VI. Still, $J_0(V)$ will remain highly sensitive to shunting and increased recombination processes, and can be used as a diagnostic tool to identify this type of degradation.

To avoid ambiguity between the single diode model interpretation of the saturation current density J_0, and the diagnostic interpretation of the $J_0(V)$ curve, presented in this work, we will denote the $J_0(V)$ curve as $J_{Loss}(V)$ from hereon. The $J_{Loss}(V)$ characteristic can be calculated by piecewise approximation of the measured $ln(J)$-V curve with equation (3.2), and solved locally for each (V_k, J_k) measurement point. This can be achieved through curve fitting or by linear approximation, as shown in (3.3):

$$J_{Loss}\left(V_k\right)=J_0\left(V_k\right)=\exp\left[\frac{\ln\left(J_{k-1}\right)V_k-\ln\left(J_k\right)V_{k-1}}{V_k-V_{k-1}}\right] \quad (3.3)$$

For the $J_{Loss}(V)$ curve we identify two distinct diagnostic sensitivity regions, depicted in Figure 3.4 for a crystalline silicon solar cell affected by different power loss mechanisms. Here, *Region A* of the $J_{Loss}(V)$ curve is highly sensitive to decreased shunt (R_{sh}) and increased junction recombination (J_{02}) processes. Whereas, *Region B* is most sensitive to increased surface and bulk recombination (J_{01}), as well as increased J_{02}, and to some extent increased series resistance (R_s). Further details regarding the derivation of this analysis are given in Publication VI.

To quantify changes in magnitude of the $J_{Loss}(V)$ curve in these two regions, we propose two diagnostic parameters $J_{Loss\text{-}A}$ and $J_{Loss\text{-}B}$, calculated as in (3.4) and (3.5):

$$J_{Loss-A}=\max\left[J_{Loss}\left(V\right)\right], for\, 0.1<V<0.40-\text{Region A} \quad (3.4)$$

$$J_{Loss-B}=\min\left[J_{Loss}\left(V\right)\right], for\, 0.4<V<0.66-\text{Region B} \quad (3.5)$$

The $J_{Loss\text{-}A}$ diagnostic parameters will primarily be sensitive to a decrease in R_{sh} and increased J_{02} losses. Whereas, $J_{Loss\text{-}B}$ will characterize increases in both J_{01} and J_{02} recombination losses, and, to a lesser extent, increased R_s also. Applying this diagnostic methodology to modules, requires normalization of the dark I-V curve to a per-cell basis. However, the computational requirements are minimal, rendering the method suitable for machine analysis.

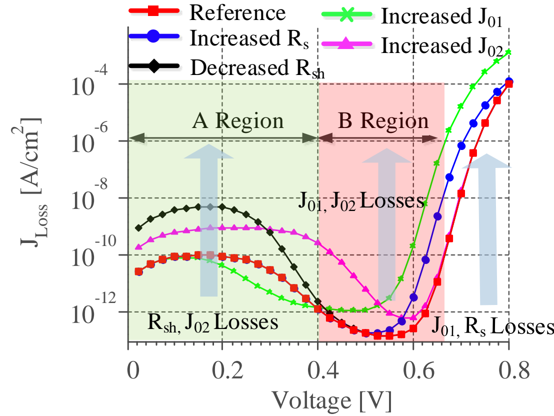

Figure 3.4: $J_{Loss}(V)$ characteristic calculated from the dark J-V curve of a crystalline silicon solar cell affected by different power loss mechanisms (simulated through diode parameter changes): red – reference dark J-V (n_1=1, n_2=2, R_s=0.8 Ωcm2, R_{sh}=10^9 Ωcm^2, J_{01}=10^{-13} A/cm^2, J_{02}=10^{-10} A/cm^2); blue – increased R_s=4 Ωcm^2; black – decreased R_{sh}=10^7 Ωcm^2; green – increased J_{01}=10^{-12} A/cm^2; magenta – increased J_{02}=10^{-9} A/cm^2.

3.3 EXPERIMENTAL VALIDATION OF THE DIAGNOSTIC PARAMETERS

The process of identifying any of the four degradation modes investigated, requires a combined analysis of all three categories of diagnostic parameters, to quantify the signatures associated with each degradation mode, as summarized in Table 3-1.This diagnostic process is shortly demonstrated next, more details ca be found in Publication VI.

3.3.1 IDENTIFYING DEGRADATION OF THE ELECTRICAL CIRCUIT

To reproduce this degradation mode, we impaired increasing levels of damage to the cell interconnect ribbons of four conventional 60-cell multicrystalline silicon PV modules (denoted R1 to R4). In module R1, two out of three ribbons per cell (for a total of four cells) were cut from the backside of the module, causing a 1.7% degradation of the STC maximum power of the module (Figure 3.5).

Modules R2, R3, and R4 sustained increasing numbers of damaged cells (12, 16, 24) interconnects leading to additional power loss, as shown in Table 3-2.

The four modules were characterized before and after impairing the damage by light I-V measurements at STC as well as dark I-V measurements (25°C).

Identifying this type of degradation can be summarized in four steps: (i) confirm the electrical nature of the degradation; (ii) confirm increases in module series resistance; (iii) confirm there is no significant increase in shunting or recombination losses; (iv) confirm there is no significant decrease in current generation.

The electrical nature of this degradation mode is confirmed by the changes in both FF and FF_{dark} parameters, as evident from Table 3-2.

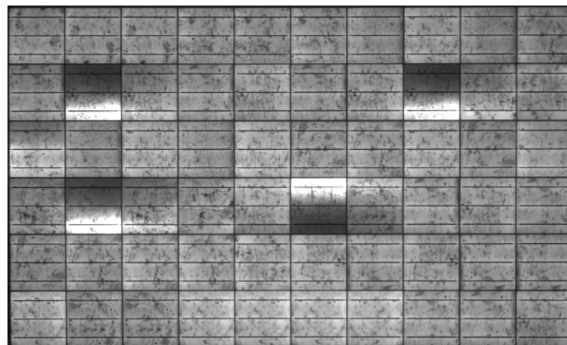

Figure 3.5: Electroluminescence image of module R1 taken at STC I_{mp} bias. The module sustained open-circuited cell interconnects, causing 1.7% STC P_{max} loss.

Table 3-2: Relative change in the diagnostic parameters of the four PV modules that have sustained different levels of damage to their cell interconnects.

Diagnostic step	Module	R1	R2	R3	R4
1) Electrical degradation confirmed	ΔP_{max} [%]	-1.7	-3.1	-5.5	-6.3
	ΔFF[%]	-1.84	-2.74	-5.18	-6.1
	ΔFF_{dark} [%]	-0.84	-1.06	-1.95	-2.77
2) Increased series resistance confirmed	$\Delta V_{d\text{-}max}$ [%]	1.04	1.76	2.88	3.84
	$\Delta R_{s\text{-}ld}$ [%]	22.4	38.2	65.8	76.2
3) No significant shunting or recombination	$\Delta J_{Loss\text{-}B}$ [%]	12.9	10.76	32.1	25.9
	$\Delta J_{Loss\text{-}A}$ [%]	-10.4	-30	-11.8	-27.8
4) No significant decrease in current generation	ΔI_{sc} [%]	0.09	-0.3	-0.27	-0.29

Next, if we analyze the series resistance of the module, we can observe a significant increase of the $R_{s\text{-}ld}$ parameter in Table 3-2, which is very sensitive to any type of series resistance losses. Moreover, the dark I-V parameter, $V_{d\text{-}max}$ increases, suggesting an addition voltage drop caused be the increase in module series resistance.

Detecting increased shunting and recombination requires analyzing the J_{Loss}(V) curve. This is exemplified in Figure 3.6, for the worst degraded module (R4) and the highest increase in series resistance.

Here, we observe that changes in the J_{Loss}(V) curve are minor. These findings are reflected in the $J_{Loss\text{-}A}$ and $J_{Loss\text{-}B}$ parameters in Table 3-2, where we can see a relatively small variation (compared to the other failure types), which is mostly due to temperature variations and numerical noise.

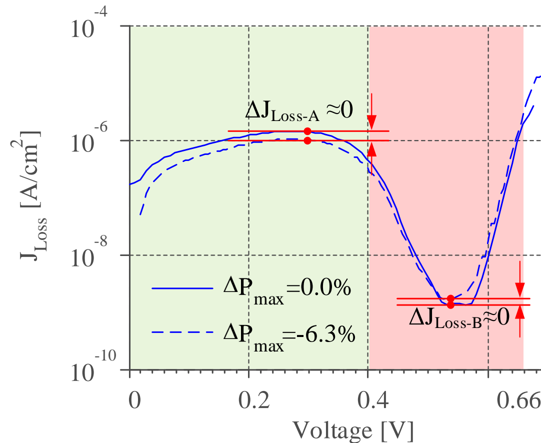

Figure 3.6: Semilog plot of the J_{Loss}(V) characteristic of module R4 with open-circuited cell interconnects (full lines – no damage; dashed lines – after damage).

Previously repeat measurements on another module design yielded a compound uncertainty of ±8% for these two parameters, for a ±0.8°C uncertainty in the module temperature. Considering this, the changes in the $J_{Loss\text{-}A}$ and $J_{Loss\text{-}B}$ parameters, are not significant enough to be attributed to any shunting or recombination losses, which will become more evident in the following sections.

3.3.2 IDENTIFYING SOLAR CELL CRACKS AND BREAKS

This degradation mode was reproduced in a laboratory environment by mechanically loading the PV modules and expanding the microcracks by exposing them to humidity-freeze cycles according to IEC 61215. We applied this accelerated procedure to a conventional 60-cell multicrystalline silicon PV module for three stress rounds, resulting in a gradual degradation of the module, as shown in Figure 3.7.

After initial STC I-V, 25°C dark I-V, and EL characterization, the module entered the first stress round (b), where it was loaded with ~400 Kg of sandbags, after which it underwent twenty-two humidity-freeze stress cycles in the environmental chamber.

After I-V and electroluminescence characterization, the module underwent the second stress round (c), consisting of additional mechanical loading. In the third stress round (d), the module underwent thirteen more humidity-freeze cycles before final characterization.

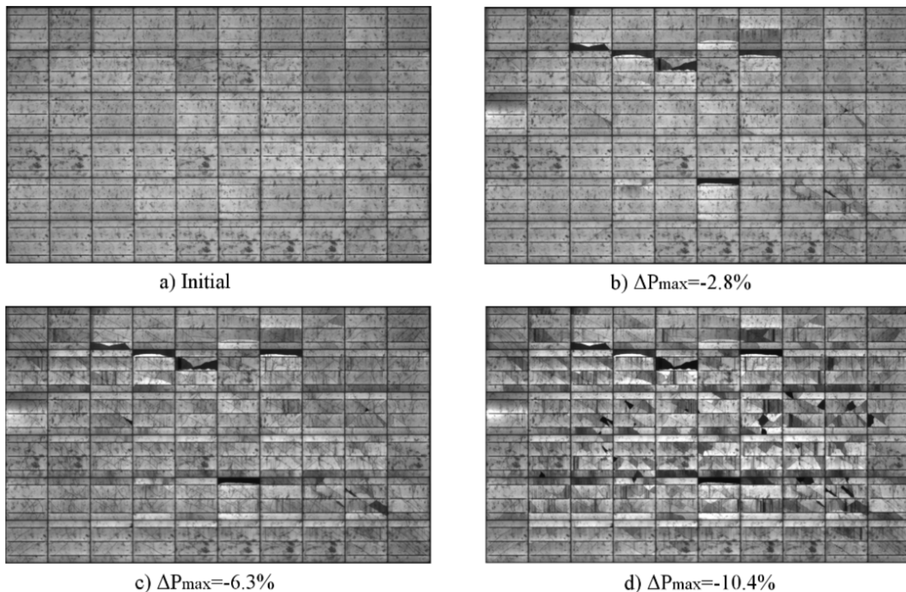

Figure 3.7: Electroluminescence image of a crystalline silicon PV module taken at STC I_{mp} bias. The module has sustained three rounds of mechanical damage to its cells. The module's STC P_{max} degraded with: a) initial – no degradation b) -2.8%; c) -6.3%; d) -10.4%.

Table 3-3: Relative change in the diagnostic parameters for a PV module in different stages of mechanical degradation.

Diagnostic step	Damage	b	c	d
1) Electrical degradation confirmed	ΔP_{max} [%]	-2.8	-6.3	-10.4
	ΔFF[%]	-1.9	-5.08	-9.18
	ΔFF_{dark} [%]	-0.8	-2.7	-4.3
2) Increased series resistance confirmed	$\Delta V_{d\text{-}max}$ [%]	0.3	1	2.9
	$\Delta R_{s\text{-}ld}$ [%]	17.8	37.9	87.6
3) Increased shunting and recombination confirmed	$\Delta J_{Loss\text{-}B}$ [%]	1E2	51E2	44E2
	$\Delta J_{Loss\text{-}A}$ [%]	1E1	2E2	2E2
4) Decrease in current generation confirmed	ΔI_{sc} [%]	-0.8	-1.05	-0.95

The STC power loss and diagnostic parameters are summarized Table 3-3 for each stage of the mechanical damage/degradation of the PV module.

Identifying mechanical degradation of the solar cells can be summarized in four steps: (i) confirm the electrical nature of the degradation; (ii) confirm increases in module series resistance; (iii) confirm increased in shunting or recombination losses; (iv) confirm decrease of current generation – due to loss of well-connected cell area.

The electrical nature of the degradation mode is confirmed by the changes in both FF and FF_{dark} parameters; whereas the decrease in current degeneration is confirmed by a reduction of I_{sc}, as shown in Table 3-3.

Similarly, we can observe an increase in module series resistance, indicated by the change in the $R_{s\text{-}ld}$ parameter in Table 3-3.

Further investigation of the J_{Loss}(V) curve, shown in Figure 3.8, confirms increased saturation currents in both the A and B regions, although the extent of their increase varies with each degradation/stress stage sustained by the module.

In the first stress stage (Figure 3.7b), $J_{Loss\text{-}B}$ increases by over 100% increase suggesting increased series and recombination losses. After the second stress stage (Figure 3.7c), the number of cracked cells increases considerably, whereas the fracture cell area increases only slightly. In this situation, we observe a significant increase in $J_{Loss\text{-}B}$ (>50 times) and $J_{Loss\text{-}A}$ (more than two-fold) compared to $R_{s\text{-}ld}$ (37.9%), suggesting active shunting and recombination losses in addition to series resistance.

Additional stress leads to an increased number of fractured/inactive cell areas, as observed in Figure 3.7d. The additional power loss may mostly be caused by series resistance ($R_{s\text{-}ld}$), which almost doubles, because $J_{Loss\text{-}A}$ and $J_{Loss\text{-}B}$ do not increase any further.

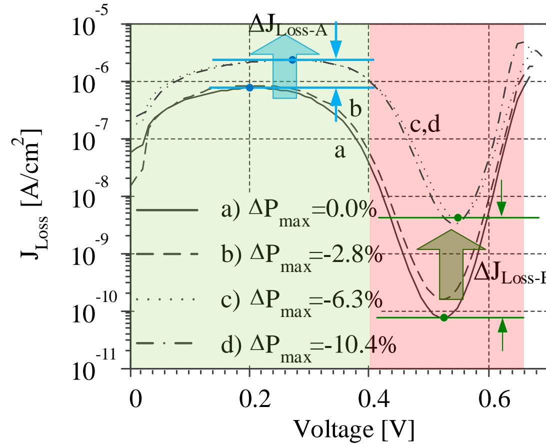

Figure 3.8: Semilog plot of the $J_{Loss}(V)$ characteristic of a PV module with mechanically damaged solar cells (full lines – no damage; dashed lines – after damage during three events).

3.3.3 IDENTIFYING POTENTIAL-INDUCED DEGRADATION

PID can be reproduced in the laboratory by means of damp-heat stress testing with applied system voltage bias [56]. We performed such an accelerated PID stress test on four conventional 60-cell multicrystalline silicon modules of different designs and PID sensitivity levels, denoted P1, P2, P3, and P4.

Modules P1, P3, and P4 were stressed at 60°C/85% RH and voltage bias of -1000 V, during which they exhibited medium to high PID sensitivity. The fast degradation rate of these modules is readily evident from the STC P_{max} degradation curves shown in Figure 3.9, measured *in-situ* according to the procedure described in [70]. In contrast, module P2, which was designed by the manufacturer to be PID-resistant, degraded much slower, as can be observed from Figure 3.9.

In addition to the in-situ (dark I-V) characterization, all modules were flash tested at STC, before and after PID stress test. Based on these measurements we calculated the changes in the diagnostic parameters, which are summarized in Table 3-4.

Similar to the previous two electrical degradation modes, identifying PID of the solar cells can be summarized in four steps: (i) confirm the electrical nature of the degradation; (ii) confirm there is no significant increases in the module's series resistance; (iii) confirm significant increase in shunting and recombination losses; (iv) confirm there is no significant decrease in current generation.

The electrical nature of the degradation is readily confirmed by the significant decrease in both *FF* and FF_{dark}, as can be observed from Table 3-4.

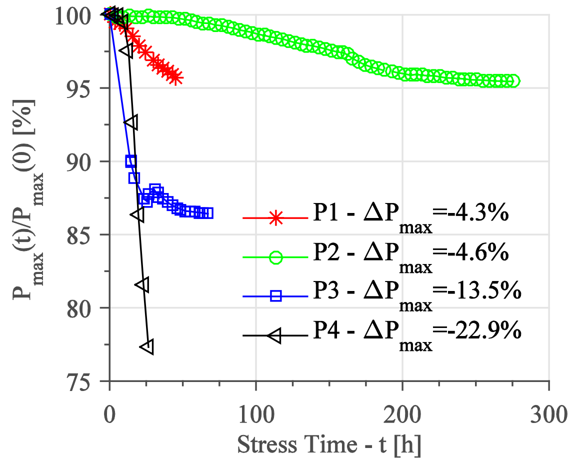

Figure 3.9: STC P_{max} degradation curves of the four modules affected by PID, as a function of stress time. The degradation curves were determined from in-situ dark I-V measurements.

Table 3-4: Relative change in the diagnostic parameters measured for the four modules affected by PID.

Diagnostic step	Module	P1	P2	P3	P4
1) Electrical degradation confirmed	ΔP_{max} [%]	-4.3	-4.6	-13.5	-22.9
	ΔFF [%]	-3.82	-4.04	-12.25	-18.2
	ΔFF_{dark}[%]	-4.05	-3.86	-11.6	-17.1
2) No significant increase in series resistance	$\Delta V_{d\text{-}max}$ [%]	-0.6	0.45	-1.13	-5.3
	$\Delta R_{s\text{-}ld}$ [%]	-2.9	3	3.56	9.2
3) Increased shunting and recombination confirmed	$\Delta J_{Loss\text{-}B}$ [%]	4.1E4	5.2E3	5.2E5	9.9E5
	$\Delta J_{Loss\text{-}A}$ [%]	8.5E2	1.6E3	5E1	4.5E2
4) No significant decrease in current generation	ΔI_{sc} [%]	-0.17	-0.24	-0.17	0.4

Moreover, there is no significant change in current generation (I_{sc}), except for the most degraded module. However, as the module become severely shunted, I_{sc} could decrease further [52, 54].

In contrast to the other two electrical degradation modes, there is no significant change in the series resistance, as indicated by the $R_{s\text{-}ld}$ parameter. Moreover, $V_{d\text{-}max}$ indicates a degradation in voltage, typically associated with shunting and PID.

Analyzing the $J_{Loss}(V)$ curve of module P2 in Figure 3.10, shows a significant increase in $J_{Loss\text{-}A}$ (~16 times) and $J_{Loss\text{-}B}$ (~52 times), indicating increased shunting and recombination losses. The same significant increases in both $J_{Loss\text{-}A}$ and $J_{Loss\text{-}B}$, can be found for the other modules, as shown in Table 3-4. However, the magnitude varies, depending on the PID susceptibility of the module, and the level of degradation.

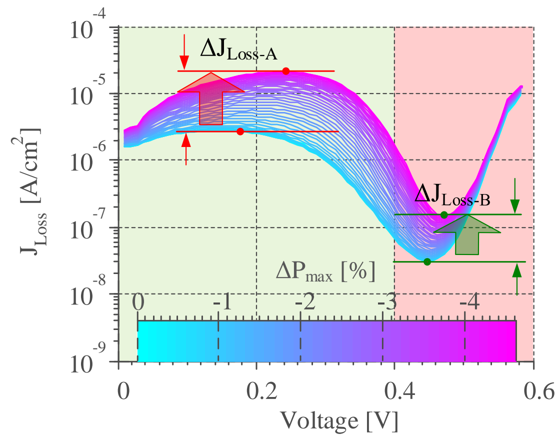

Figure 3.10: Semilog plot of the $J_{Loss}(V)$ characteristics of module P2 (cyan – no PID; magenta – after PID) causing 4.6% STC P_{max} loss, calculated from the dark I-V curves were measured in-situ at stress temperature, during the accelerated PID stress test.

To be noted that, perhaps the most significant parameters for identifying the presence of PID are J_{Loss-A} and J_{Loss-B}, which show a very large increase for this particular failure mode, as can be observed in Table 3-4—several orders of magnitude larger than in the case of cell cracks and fractures (Table 3-3).

3.4 SUMMARY AND CONCLUSIONS

This chapter proposed a PV module diagnostic method that can identify: (i) optical losses and degradation, (ii) degradation of the electrical circuit of the PV module, (iii) mechanical degradation of the solar cells, (iv) PID of the solar cells.

The method is based on the analysis of the light and dark I-V characteristics of the PV module, and is founded on the premise that the four degradation modes discussed have different signatures reflected on the light I-V (FF, I_{sc}, R_{s-ld}) and dark I-V (FF_{dark}, V_{d-max}, J_{Loss-A}, J_{Loss-B}) diagnostic parameters. These signatures can be used to devise a simple fault-identification procedure summarized as follows:

Optical losses and degradation are indicated by changes in light I-V parameters (FF, I_{sc}, R_{s-ld}) but not present in the dark I-V parameters (FF_{dark}, V_{d-max}).

Degradation of the electrical circuit of the PV module is indicated by: decreased FF and FF_{dark}, increased R_{s-ld} and V_{d-max}, no significant change in I_{sc}, and no significant change in J_{Loss-A} and J_{Loss-B}.

Mechanical degradation of the solar cells is indicated by: decreased FF and FF_{dark}, increased R_{s-ld} and V_{d-max}, possible decrease in I_{sc}, and significant change in the J_{Loss-A} and J_{Loss-B} parameters.

PID of the solar cells is indicated by: significant decrease of FF and FF_{dark}, no significant change in $R_{s\text{-}ld}$, possible decrease in $V_{d\text{-}max}$, no significant change in I_{sc}, and a very large increase in the $J_{Loss\text{-}A}$ and $J_{Loss\text{-}B}$ parameters.

The diagnostic method is very sensitive to the progression of the four degradation modes discussed, and can be used as an automated laboratory diagnostic tool, since it has low computational requirements and is machine analysis friendly. Moreover, the method has potential for field applications such as implementation in I-V tracers for long-term reliability monitoring of PV modules, with the goal of identifying the onset and progression of the different degradation modes, without the need of periodic inspection and imaging. Another possible application would be in module-integrated converters capable of bidirectional current flow, where the method can be used to optimize maintenance operations by scheduling appropriate actions based on the severity and type of degradation affecting the PV modules.

Implementing the method for outdoor operation needs to take into consideration the changing ambient conditions, as well as practical implementation issues; however, this falls outside the scope of the current work and is anticipated to be developed in the future.

CHAPTER 4
MODULE DEGRADATION AND FAILURE DIAGNOSIS USING ELECTROLUMINESCENCE IMAGING

This chapter proposes a method for quantifying the extent of different failures and degradation modes present in crystalline silicon PV modules by analyzing the electroluminescence intensity distribution obtained by imaging the modules.

4.1 INTRODUCTION

EL imaging of PV modules is most commonly used as a qualitative diagnostic tool for visual identification of failures, defects, and degradation. However, the diagnostic information contained in the EL images can be quantified, with the purpose of rating module quality or the state of health, enabling advanced PV module diagnostics, beyond visual or qualitative methods. In this regard we propose a quantitative EL diagnostic method, based on analyzing the EL intensity (ELI) distribution of the PV module being diagnosed. This allows for calculating distribution statistics and other empirical parameters that can quantify defects and degraded module/cell areas visible in the EL image of the module.

This method can be used to rate cell degradation/failures or quality of modules after transportation, installation, or field operation. Moreover, the method can be automated and used in quality control for module manufacturers or installers, or as a diagnostic tool by plant operators and diagnostic service providers.

The next two sections will present the main diagnostic concepts and steps for calculating the diagnostic parameters from the ELI distribution of the module and then move on to diagnosing individual cells within the module. These concepts will be exemplified on a crystalline silicon PV module which has sustained mechanical degradation of its solar cells. The third part of the chapter will show experimental results from the application of the method to quantify: (i) mechanical degradation of the solar cells (cell fractures), (ii) PID of the solar cells, (iii) and cell interconnect degradation in PV modules.

The EL measurement hardware, procedure, and test conditions followed the guidelines according to the future standard entitled “Photovoltaic devices - Part 13: Electroluminescence of PV modules (proposed future IEC TS 60904-13)” [75].

4.2 MODULE-LEVEL ELI DISTRIBUTION ANALYSIS

The derivation of the diagnostic method starts by analyzing the ELI distribution of a standard 60-cell multicrystalline silicon PV module, which has sustained four rounds of mechanical loading and humidity-freeze cycling according to IEC 61215, resulting in a gradual mechanical degradation of its solar cells. The module was characterized at STC on a flash tester and imaged before and after each round of stress.

The EL measurements were taken in a temperature controlled (25ºC) dark room imaging studio, with a high resolution (4096x2504) NIR camera (CCD sensor). The modules were mounted in a fixed position such that the camera is normal with respect to the module surface, and at a fixed distance, to optimize the useful module image area. They were forward biased at STC I_{mp} with a dc supply during measurement. Moreover, the camera aperture, exposure, and integration time were optimized to obtain a good image contrast and avoid saturation of the image. To facilitate the image analysis and obtain high quality EL images of the module, the test conditions were kept constant in subsequent measurements on the same module test sample (or design, if more than one modules are analyzed).

The resulting EL images of the initial and four subsequent stages of mechanical degradation are shown in Appendix A, Figure A.1 to Figure A.5. As can be observed from these grayscale EL images, the damaged/degraded module areas appear as distinct solar cell regions with lower EL intensity, relative to the EL intensity of healthy cells. To detect and quantify these low EL intensity regions from the module grayscale EL image, we propose to analyze the normalized image histogram $p_{EL}(i)$, calculated as in (4.1):

$$p_{EL}(i) = \frac{n_i}{n}, \ 0 \leq i < L \tag{4.1}$$

Where i is the gray level of a pixel, n_i is number of occurrences of gray level i, n is the total number of pixels in the image, L is the total number of gray levels in the image (256 in this case). If we calculate the histograms $p_{EL}(i)$ from the module EL images (Figure A.1 to Figure A.5), taken before and after the degradation of the solar cells, we obtain the EL intensity distributions shown in Figure 4.1. Here, the lowest EL intensity 0 signifies absolute dark, whereas 1 signifies the highest EL intensity that can be measured and represented by the EL camera.

From Figure 4.1 we can observe that the $p_{EL}(i)$ is a bimodal distribution, composed of: (i) a higher EL intensity sub-distribution, and denoted from hereon as the *active area* of the module, representing the radiative regions of the solar cells; (ii) and a lower EL intensity sub-distribution, composed of the darker module regions, representing the background, the non-radiative module components, space between solar cells, as well as the defected and most degraded cell regions, denoted from hereon as the *inactive area* of the module.

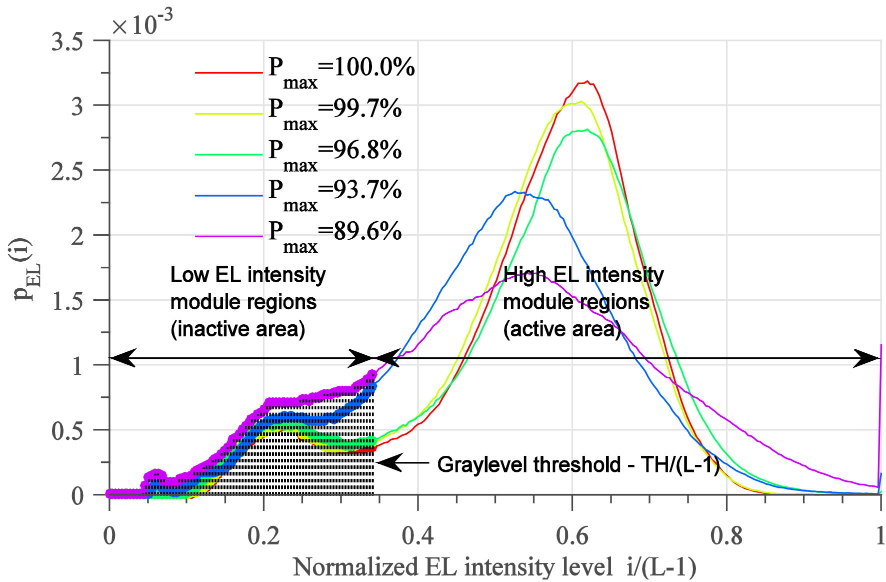

Figure 4.1: Normalized (L=256) EL intensity histogram of a crystalline silicon PV module which has sustained four rounds of mechanical damage to its cells. The module's STC P_{max} was measured after each round of damage and is shown relative to the initial value. The normalized gray level threshold TH/(L-1)=0.34 was calculated using Otsu's method [114].

This type of bimodal EL intensity distribution is typical for crystalline silicon PV modules, since low and high EL intensity module regions will always be present, provided the EL image has been acquired with a high contrast ($p_{EL}(i)$ has a high spread), and image was not saturated (due to overexposure).

As the module degrades, the shape, spread, and location of the two ELI sub-distribution changes, due to the increased number of defects and degraded solar cell regions, which causes a decrease of luminescence in the affected module areas. These changes can be characterized by calculating summary statistics (such as standard deviation, median, kurtosis, and skewness) for the two ELI sub-distributions, and used as diagnostic parameters to quantify the extent of solar cell defects and degradation.

To calculate the summary statistics we first need to separate two ELI sub-distributions from $p_{EL}(i)$, by choosing an appropriate gray level threshold value TH, as highlighted in Figure 4.1. This can be done manually, or by using an image segmentation algorithm such as Otsu's method [114], which calculates and optimal threshold value that separates the two ELI sub-distributions so that their combined intra-class variance is minimal. It is important to note that gray level threshold value and conditions for test should be kept constant once chosen for a module type.

Starting from the initial EL image of the module, shown in Appendix A, Figure A.1, we applied Otsu's method [114], and calculated an optimal threshold value

TH/(L-1)=0.34. This value was then used to separate all subsequent ELI sub-distributions, as shown in Figure 4.1, and then calculate summary statistics for each distribution.

One important summary statistic parameter used in this analysis is the standard deviation (STD) of the ELI sub-distributions, calculated as in (4.2), (4.3), and (4.4) for the total, inactive, and active ELI sub-distributions:

$$STD_{Total} = \sqrt{\sum_{i=0}^{L-1} \left[p_{EL}(i) - \mu_{Total} \right]^2} \; where \; \mu_{Total} = \frac{1}{L} \sum_{i=0}^{L-1} p_{EL}(i) \tag{4.2}$$

$$STD_{Inactive} = \sqrt{\sum_{i=0}^{TH} \left[p_{EL}(i) - \mu_{Inactive} \right]^2} \; where \; \mu_{Inactive} = \frac{1}{TH+1} \sum_{i=0}^{TH} p_{EL}(i) \tag{4.3}$$

$$STD_{Active} = \sqrt{\sum_{i=TH+1}^{L-1} \left[p_{EL}(i) - \mu_{Active} \right]^2} \; where \; \mu_{Active} = \frac{1}{L-TH-1} \sum_{i=TH+1}^{L-1} p_{EL}(i) \tag{4.4}$$

The STD of the ELI distributions, shown in Figure 4.2 for the different stages of module degradation, can be used to quantify the general condition and quality of the module. For high quality modules, with few defects and degraded cells, the spread of the ELI distributions will be tight, characterized by a small STD value. Whereas degraded, or low quality modules (with defects and mismatched cells) will have a higher STD value. This allows for a practical comparison method between modules of the same design (new vs. degraded), or modules of different design (or manufacturers).

Another important parameter is the percent of inactive module area IMA_{EL}, calculated from the low EL intensity sub-distribution from $p_{EL}(i)$, as shown in (4.5):

$$IMA_{EL}[\%] = 100 \sum_{i=0}^{TH} p_{EL}(i) \tag{4.5}$$

The IMA_{EL} parameter will quantify both: (i) the percent of damaged/degraded solar cell regions in the module; (ii) as well as cell defects, low lifetime and dark regions in the EL image (busbars, space between cells, etc.). To separate these two groups, and determine the percent of damaged/degraded solar cell regions denoted CD_{EL}, we need to make a baseline EL measurement on a “best- in-class” module of the same design and under the same measurements conditions. Using this reference module, we can calculate an $IMA_{EL\text{-}baseline}$ value and determine the CD_{EL} as in (4.6):

$$CD_{EL}[\%] = IMA_{EL} - IMA_{EL-baseline} \tag{4.6}$$

For crystalline silicon modules EL imaged at high current bias (I_{mp} or I_{sc}), we determined an average $IMA_{EL\text{-}baseline}$=11%.

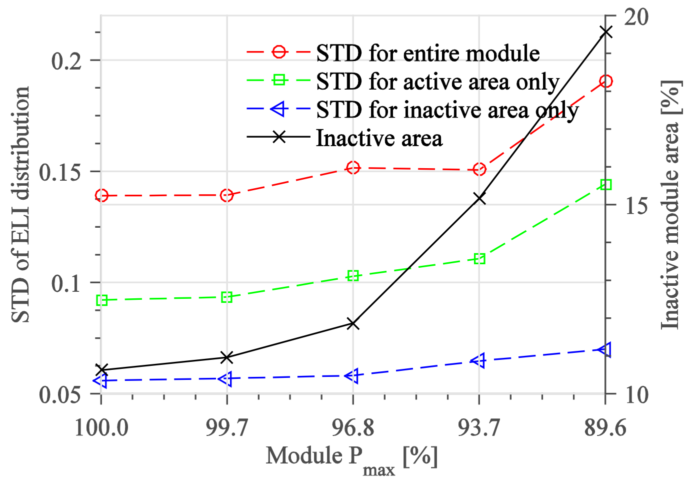

Figure 4.2: Standard deviation of the EL intensity distributions and percent or active/inactive module area IMA_{EL}, calculated for each degradation stage of the module.

To exemplify, Figure 4.2 shows the percentage of inactive module area IMA_{EL}, starting from 10.6% when the module was new, up to 19.6 % after the last round of degradation, allowing a practical measurement of the extent of damaged cells.

Going one step further, we use the same threshold value *TH* to segment the module EL image into two classes (active and inactive), where the low EL intensity module regions will be associated with the inactive class, whereas the higher EL intensity region will belong to the active class. This process, also known as *image thresholding or segmentation* [115], practically reduces the grayscale EL image to a binary image, denoted from hereon as the *active/inactive module area map*.

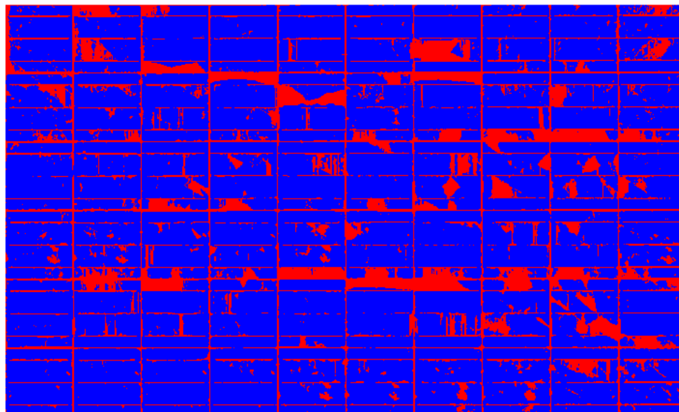

Figure 4.3: Module map of active (blue - 80.4%) and inactive (red – 19.6%) areas, calculated by thresholding (at 0.34 ELI) the EL image of the PV module, taken after the last round of mechanical damage (STC P_{max} = 89.6% of initial value).

We then used this segmentation process to calculate the *active/inactive module area maps* for each degradation stage of the module, shown in Appendix A, Figure A.6 to Figure A.9, and in Figure 4.3 for the final stage of degradation, where the red areas denote the inactive module regions, and the blue area denote the active regions. These maps can be used to highlight the degraded or damaged solar cells.

4.3 CELL-LEVEL ELI DISTRIBUTION ANALYSIS

The module-level summary statistics (STD_{Total}, STD_{Active}, $STD_{Inactive}$) and percent of inactive module area (IMA_{EL} and CD_{EL}) can be used directly as diagnostic parameters to quantify module quality and degradation. However, considering that a PV module is composed of solar cells, it is sometimes relevant to know whether one cell is 60% damaged or two cells are each 30% damaged. For example when assessing the risk of power loss in PV modules with mechanically degraded solar cells; a single cell, having 12% to 50% electrically disconnected cell areas (cracks), can cause a power loss that increases nearly linearly from zero to the power of one double cell-string [44]. Moreover, in most practical cases the power loss from two cracked cells is determined by the cell with the largest inactive cell area per double string [44], thus it not cumulative and must be assessed individually.

To quantify damage and degradation on cell level, we propose to perform the ELI distribution analysis on the sub-EL images of individual cells. Identifying individual cells within a module's EL image can be relatively easy achieved automatically by dividing the module surface image into evenly distributed rows and columns, given the number of solar cells and their layout within the module. This process is exemplified in Figure 4.4 for the standard 60-cell module analyzed previously.

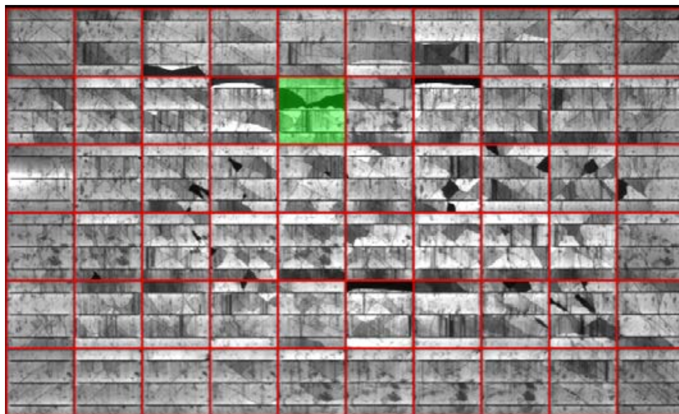

Figure 4.4: Example of dividing the module EL image into individual cell images for performing ELI distribution analysis on each solar cell.

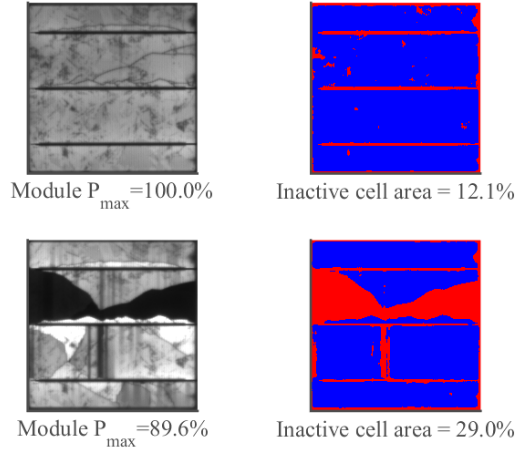

Figure 4.5: EL image of cell (2, 5). The upper images show the solar cell before the degradation, whereas the lower images show the cell after the last round of mechanical stress.

In Figure 4.4 the solar cell from row 2, column 5, highlighted with green, will be used to demonstrate the cell-level ELI distribution analysis.

This cell is detailed in Figure 4.5 (left), where the upper images show the solar cell before the degradation, whereas the lower images show the cell after the last round of degradation. By segmenting these two images, using the same procedure and *TH* value obtained from the module-level analysis, we obtain a cell-level active/inactive area map, shown in Figure 4.5 (right).

From each solar cell sub-EL image we can determine a cell-level image histogram $p_{EL\text{-}Cell}(k, i)$, calculated as in (4.7), and shown in Figure 4.6:

$$p_{EL-Cell}\left(k,i\right)=\frac{n_i^k}{n^k},\ 0\leq i<L,1\leq k\leq N_c \tag{4.7}$$

Where k is the solar cell number, N_c is the number of solar cells in the module, n_i^k is number of occurrences of gray level i in cell k, n^k is the total number of pixels in the image of cell k.

Next, by analyzing the $p_{EL\text{-}Cell}(k, i)$ histograms for this cell, through the five stages of degradation, as shown in Figure 4.6, we can observe that the shape of the two ELI sub-distributions changes (in this case the spread increases). These changes of the ELI sub-distributions can be quantified by summary statistics, similar to the module-level case in (4.2)-(4.4) and compared with the parameters of a “best-in-class” solar cell, from the same module or a module of similar design.

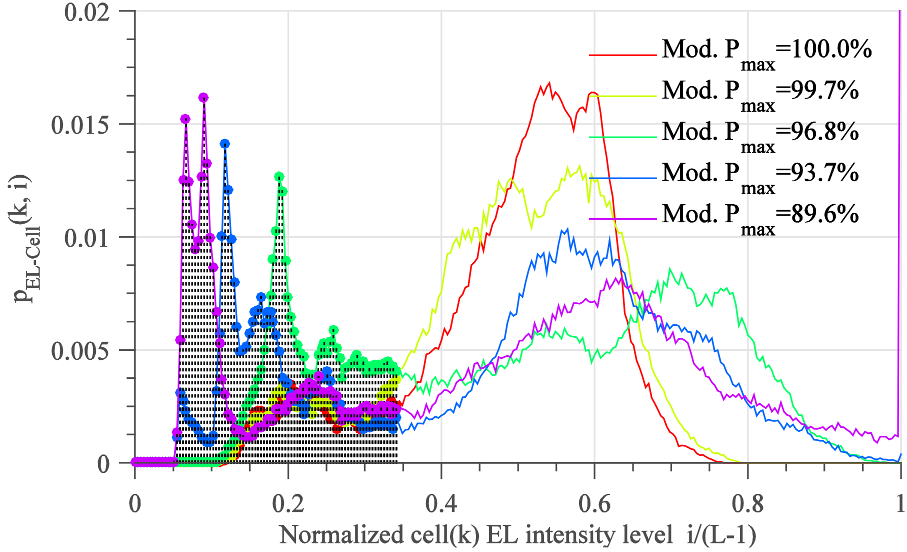

Figure 4.6: Normalized (L=256) EL intensity histogram of cell (2, 5). The threshold value used was TH/(L-1)=0.34, calculated from the initial ELI distribution of the PV module.

We can consider cell (2, 5) before degradation to be the "best-in-class", and determine the spread of the ELI distribution $STD_{Cell}(k)$, calculated as in (4.8), for each round of degradation. The resulting $STD_{Cell}(k)$, for cell (2, 5) is shown in red in Figure 4.7, exhibiting a significant increase as the module degrades.

$$STD_{Cell}(k)=\sqrt{\sum_{i=0}^{L-1}\left[p_{EL-Cell}(k,i)-\mu_{Cell}\right]^2}\ \ where\ \ \mu_{Cell}=\frac{1}{L}\sum_{i=0}^{L-1}p_{EL-Cell}(k,i) \quad (4.8)$$

Alternatively, we can calculate the summary statistics of the low and high ELI sub-distributions of the solar cell, similar to (4.3) and (4.4) for the module-level case. These are shown in green and blue in Figure 4.7, and show a similar trend with the module-level EL intensity spread in Figure 4.2. These cell-level parameters can potentially be used to identify specific solar cell degradation signatures, such as cell shunting vs. cell fractures, for modules affected by more than one failure/degradation mode.

Similarly, we can calculate the percent of inactive cell area $IMA_{EL\text{-}Cell}$, relative to the total area of the cell, for each cell as in (4.9):

$$IMA_{EL-Cell}(k)[\%]=100\sum_{i=0}^{TH}p_{EL-Cell}(k,i) \quad (4.9)$$

For cell (2, 5) in Figure 4.5, we calculated an $IMA_{EL\text{-}Cell}$=12.1% before degradation, and 29% after the last stage of degradation, given a module-level IMA_{EL}=19.6%.

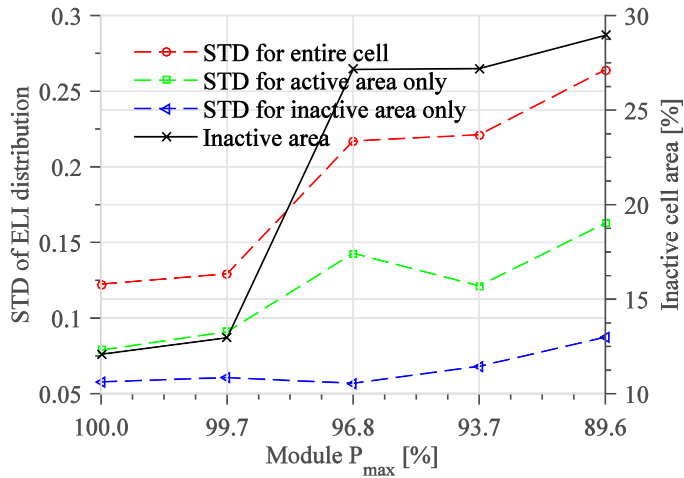

Figure 4.7: Standard deviation of the EL intensity distribution and percent or active/inactive area for cell (2, 5), calculated for each degradation stage.

In the case of cell fractures, the module-level IMA_{EL} can be useful to quickly rate module quality and detect improper transportation or mishandling of the modules during installation. Whereas the cell-level $IMA_{EL\text{-}Cell}$ can be used to rate the severity of the cell fractures and quantify the risk of power loss in the modules, by determining the size of the cell fractures for each cell.

Moreover, if we calculate and aggregate the summary statistics, or $IMA_{EL\text{-}Cell}$ of each cell, we can quantify the differences/mismatch between the solar cells in the module, without requiring a reference solar cell, and practically use it as an indicator for module quality.

4.4 QUANTIFYING MODULE DEGRADATION AND FAILURES

To demonstrate the diagnostic procedure described in the previous sections, we will apply it to diagnose three types of module degradation modes: (i) mechanical degradation of the solar cells (cell fractures); (ii) PID of the solar cells; (iii) degradation of the solar cell interconnects. Then we will show how to use the resulting cell-level ELI parameter matrix quantify cell mismatch within the module.

4.4.1 MECHANICAL DEGRADATION OF THE SOLAR CELLS

In this example we analyze the degradation of the 60-cell multicrystalline silicon PV module, described in the previous section, which has sustained four rounds of mechanical and thermal stress. EL images for the initial and four subsequent stages of mechanical degradation are shown in Appendix A, Figure A.1 to Figure A.6.

We first calculate the matrix of “percent of inactive cell area” $IMA_{EL\text{-}Cell}$ parameters as shown in (4.9), for each cell within the module, and for the initial and final degradation stage. By plotting these matrices, as shown in Figure 4.8, before degradation (left), and after the last stage of degradation (right), we can get a clear picture of the distribution of cell fractures and cell mismatch within the module, as well as the severity of these fractures.

Such 3D plots of the diagnostic matrices can be useful to visually represent the location and severity of cell failures/defects within a module. However, to quantify the diagnostic information in these matrices, into fewer diagnostic parameters that can allow direct comparison between modules, we calculate the distribution of $IMA_{EL\text{-}Cell}(k)$ matrix elements, as shown by the histogram in Figure 4.9.

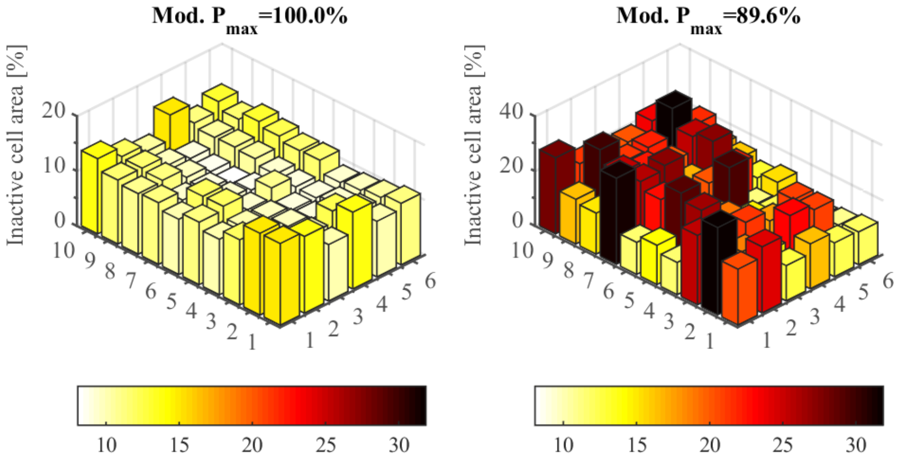

Figure 4.8: Diagnostic matrix of $IMA_{EL\text{-}Cell}$ cell-level parameters, calculated before (left) and after (right) the module degradation, for each cell within the module. The threshold value used was 0.34, calculated from the module’s initial ELI distribution.

The distribution of $IMA_{EL\text{-}Cell}(k)$ parameters in Figure 4.9 allows for a quick numerical evaluation of the condition of the cells in the module. For example, when the module is in good condition (P_{max}=100%), few cells have defects and most of them are nearly identical, resulting in a tight distribution of the $IMA_{EL\text{-}Cell}(k)$ parameters. However, as the module degrades, the number of fractured cells increases, leading to an increasing spread (STD_{IMA}) of the $IMA_{EL\text{-}Cell}(k)$ parameters, calculated as in (4.10):

$$STD_{IMA} = \sqrt{\sum_{k=1}^{Nc} \left[IMA_{EL-Cell}(k) - \mu_{IMA} \right]^2} \; where \; \mu_{IMA} = \frac{1}{Nc} \sum_{k=1}^{Nc} IMA_{EL-Cell}(k) \quad (4.10)$$

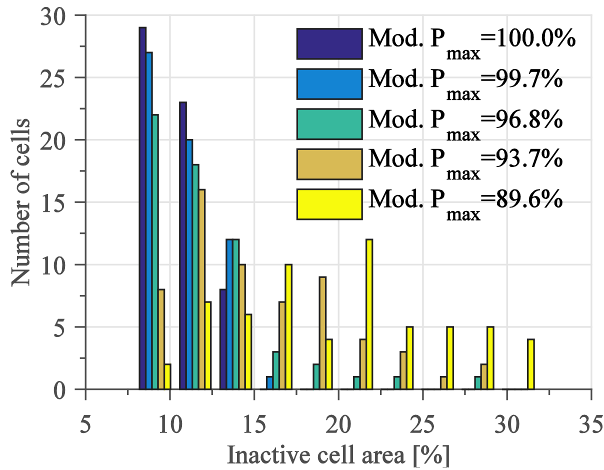

Figure 4.9: Distribution of $IMA_{EL\text{-}Cell}(k)$ cell-level parameters within the module, calculated for each degradation stage.

Calculating summary statistics for the distribution of $IMA_{EL\text{-}Cell}(k)$ cell-level parameters, such as the STD_{IMA} or median, can be used to directly quantify the level of cell mismatch, and extent of cell fractures in the module, with a single parameter. This is exemplified in the boxplot in Figure 4.10, where we can clearly observe an increase in the median inactive cell area (red in in Figure 4.10), increased spread (the 25th and 75th percentiles) and STD (blue in in Figure 4.10), as well an increased number of outliers, as the module degrades, and representing the most degraded cells.

The same procedure can be applied to visualize and quantify other cell-level diagnostic parameters, such as the STD_{Cell}(k), calculated as in (4.8), and shown in Figure 4.11.

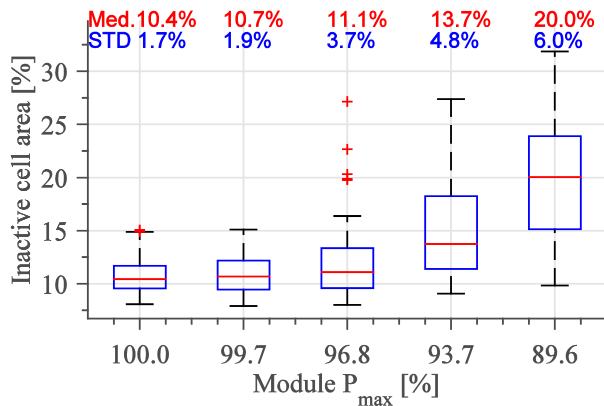

Figure 4.10: Boxplot of the distribution of $IMA_{EL\text{-}Cell}$ cell-level parameters within the module, calculated for each degradation stage. Median and STD are shown in red and blue, in percent units since the $IMA_{EL\text{-}Cell}(k)$ is measured in percent.

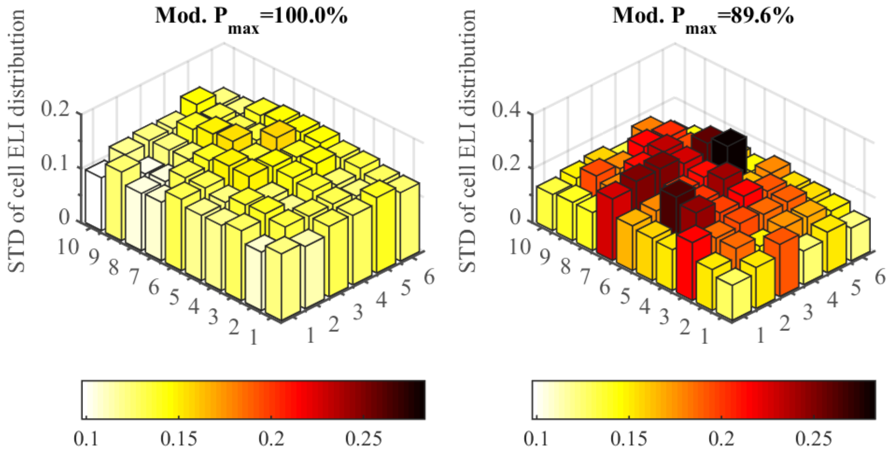

Figure 4.11: Diagnostic matrix of $\underline{STD_{Cell}}(k)$ parameters, calculated before (left) and after (right) the module degradation, for each cell within the module.

In this case, the distribution of $STD_{Cell}(k)$ cell-level parameters can be used to quantify the overall quality of the cells within the module. Since better quality solar cells will tend to have a more uniform luminescence distribution (uniform radiative recombination [116] occurring across the cell surface), resulting in a tighter ELI distribution. Whereas, degraded or lower quality solar cells with defects, will vary in luminescence across the solar cell surface, depending on the defect type, resulting in a wider ELI distribution, and thus higher $STD_{Cell}(k)$ values. This is evident in Figure 4.12, where the number of cells with wider cell ELI distributions (higher STD values) increases as the module degrades.

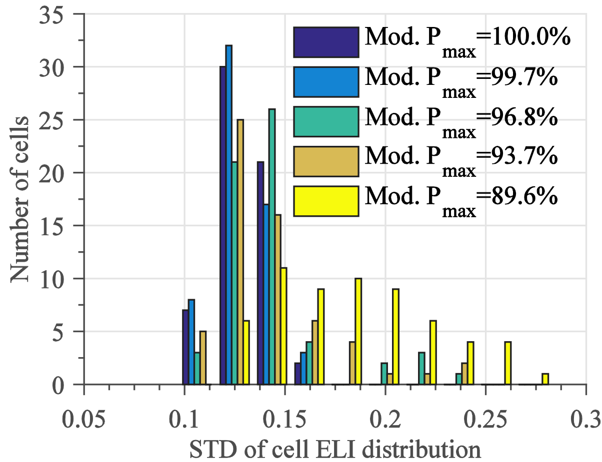

Figure 4.12: Distribution of $STD_{Cell}(k)$ parameters within the module, calculated for each degradation stage.

4.4.2 PID OF THE SOLAR CELLS

PID was reproduced and studied on a conventional 60-cell monocrystalline silicon PV module, by means of damp-heat stress (60°C/85% RH) testing with applied system voltage bias (-1000 V), according to the procedure in [56]. The module was characterized at STC on a flash tester (P_{max} degraded down to 76.8% of the initial value), and imaged before (Appendix B, Figure B.1), and after the PID stress (Figure B.2). The EL measurements were taken under dark conditions, at STC I_{mp} current bias, using the same setup and procedure described in the previous sections.

Next, the module-level ELI distribution $p_{EL}(i)$ was calculated from the initial (P_{max} =100%) EL image of the module, and using Otsu's method, an optimal gray level threshold value $TH/(L-1)$=0.3 was determined.

Using this threshold value, we segmented both the initial EL image (Figure B.1) of the module, as well as the one taken after the PID stress (Figure B.2), resulting in two active/inactive module area maps, shown in shown in Appendix B, Figure B.3 and Figure B.4. From the initial $p_{EL}(i)$ distribution we calculated a total module inactive area IMA_{EL}=10.2%, indicative of a new module. Whereas, from the $p_{EL}(i)$ distribution measured after the module degradation, we calculated an inactive area of IMA_{EL}=31.3%. In this case, the solar cells closer to the module frame, degraded faster than those in the center, and became shunted, appearing darker in the EL image (shown in Figure B.2). The same solar cells can be observed in Figure B.4, where they show a high percentage of inactive cell areas.

The degraded cells can be better visualized and identified by calculating the cell-level inactive area $IMA_{EL\text{-}Cell}(k)$ parameters, as in (4.9), and showed in Figure 4.13. Here, solar cell shunting corresponds to a high $IMA_{EL\text{-}Cell}(k)$.

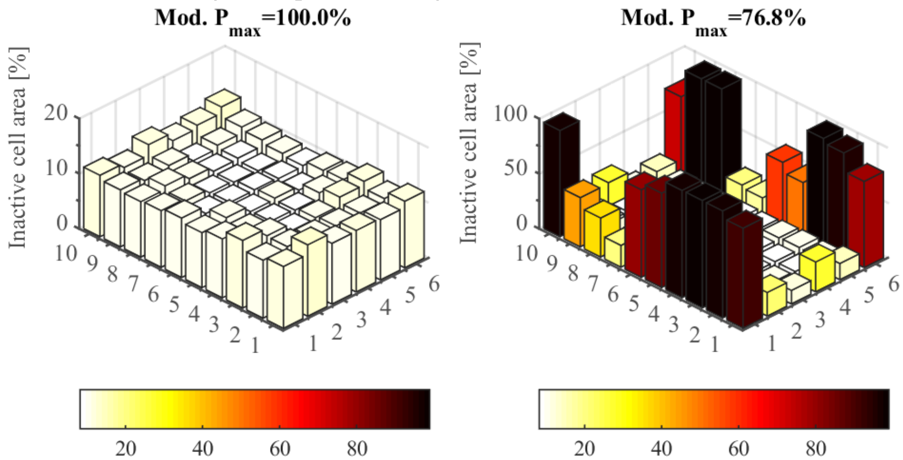

Figure 4.13: Diagnostic matrix of $IMA_{EL\text{-}Cell}$ cell-level parameters, calculated before (left) and after (right) the PID stress, for each cell within the module.

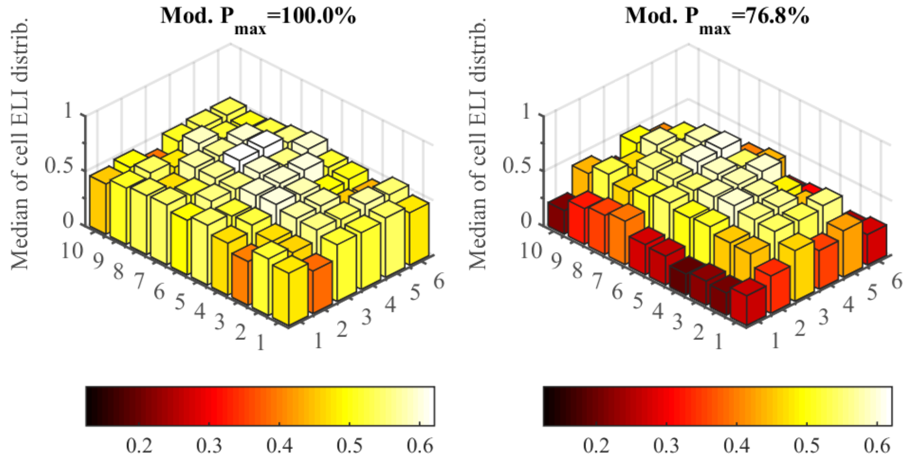

Figure 4.14: Diagnostic matrix of "Median of cell ELI distribution" parameters, calculated before (left) and after (right) the PID stress, for each cell within the module.

Similarly, considering that PID/shunted cells are characterized by a decrease in luminescence, we can use the median of the cell-level ELI distribution $p_{EL\text{-}Cell}(k, i)$, to quantify this decrease in luminescence. This is exemplified in Figure 4.14, where the cells degraded by PID show a decreased EL intensity.

The diagnostic information contained in the matrix of $IMA_{EL\text{-}Cell}$ and ELI median cell-level parameters, shown in Figure 4.13 and Figure 4.14, respectively, can be summarized by calculating their own summary statistics, as shown in Figure 4.15.

Here we can observe a significant increase in STDIMA (from 1% to 33.5%), whereas the median is nearly constant (from 10.3% to 11.1%), suggesting that most cells are in good condition, whereas some cells are severely degraded.

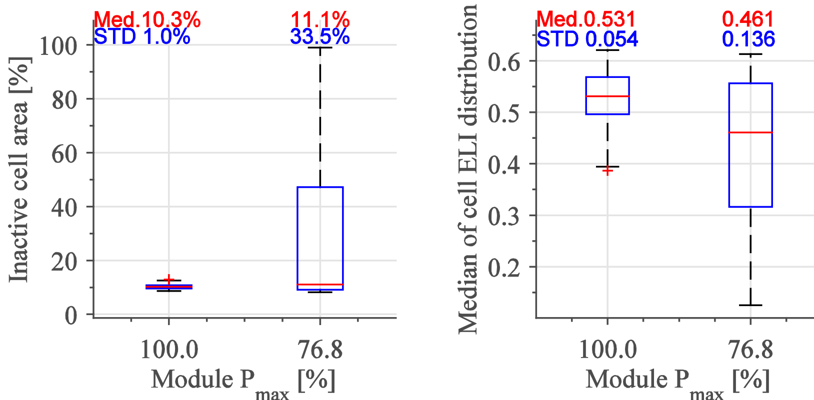

Figure 4.15: Boxplot of the distribution of the "inactive cell area" $IMA_{EL\text{-}Cell}(k)$ (left) and "median of cell ELI distribution" (right) parameters within the module, calculated before and after the PID stress. Median and STD values are shown in red and blue.

4.4.3 DEGRADATION OF THE CELL INTERCONNECTS

To reproduce this degradation mode we damaged the cell interconnect ribbons of a conventional 60-cell multicrystalline silicon PV module, by cutting one of the two ribbons per cell (for a total of twelve cells), from the backside of the module, causing a decrease of 3.1% of the module's STC P_{max}. The module was EL imaged before (Appendix C, Figure C.1), and after the damage to cell interconnects (Figure C.2). The EL measurement were taken under dark conditions, at STC I_{mp} current bias.

As in the previous two sections, we calculated the module-level ELI distribution $p_{EL}(i)$, from the initial EL image (Figure C.1), and used Otsu's method to threshold this distribution, resulting in an optimal threshold value $TH/(L-1)$=0.24. Using this threshold value, we segmented both the initial EL image (Figure C.1) of the module, as well as the one taken after the damage to the cell interconnects (Figure C.2), resulting in two active/inactive module area maps, shown in Appendix C, Figure C.3, and Figure C.4.

From the ELI distribution $p_{EL}(i)$ of the initial EL image, we determined a total module inactive area IMA_{EL}=11.6%. Whereas, after the damage to the cell interconnects, the IMA_{EL} increased to 15.6%.

The decrease in luminescence in the inactive module areas, highlighted in Figure C.4, can be explained by the lack of current due to the interconnect break – since the current is supplied from the power source through those interconnects.

The affected solar cells are clearly visible by plotting the inactive cell area parameters for all solar cells in the module, as shown in Figure 4.16. Here, these solar cells show a significant increase in inactive cell area.

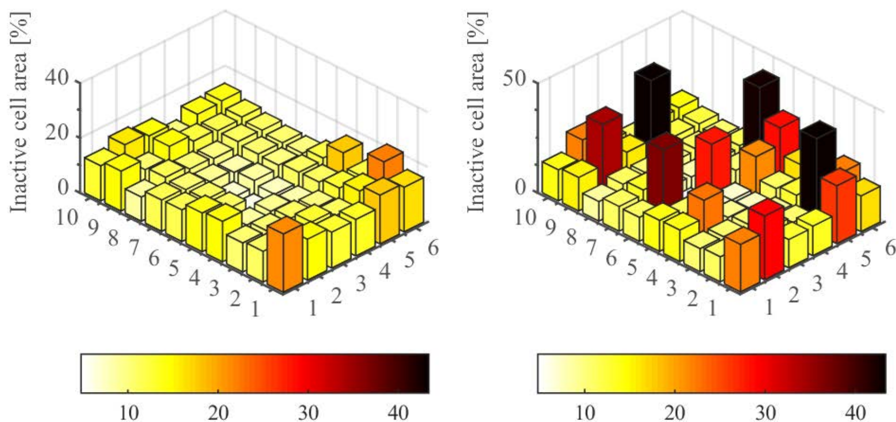

Figure 4.16: Diagnostic matrix of $IMA_{EL\text{-}Cell}$ cell-level parameters, calculated before (left) and after (right) the damage to the cell ribbons, for each cell within the module.

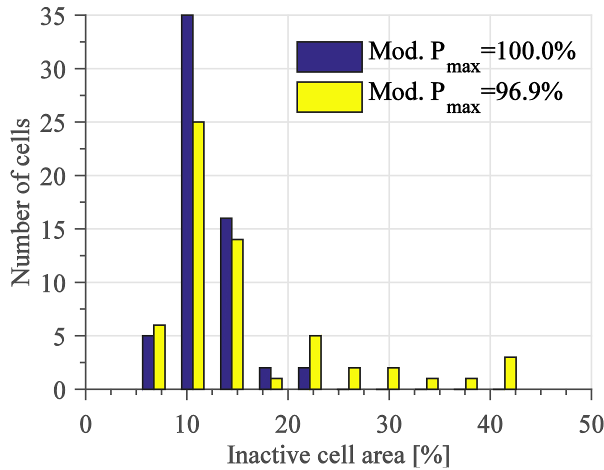

Figure 4.17: Distribution of $IMA_{EL\text{-}Cell}(k)$ cell-level parameters within the module, calculated before and after the damage to the cell interconnects.

This mismatch between solar cells, due to the damaged cell interconnects can be quantified by calculating the distribution of $IMA_{EL\text{-}Cell}(k)$ cell-level parameters, as shown in Figure 4.17. In this case the STD_{IMA} increases from 3.1% to 9.2% due to the damaged cells.

4.5 SUMMARY AND CONCLUSIONS

This chapter proposed a method for quantifying the extent of different failures and degradation modes present in crystalline silicon PV modules by analyzing the EL intensity distribution obtained by imaging the modules.

First, the methodology was presented for analyzing the module-level EL intensity distribution, introducing the concepts of bimodal distribution thresholding, calculation of the active/inactive area map, and use of the ELI distribution summary statistics in analyzing the module EL image.

The module-level diagnostic parameters, such as inactive module area IMA_{EL} and STD_{Total}, can be used to quickly rate module quality and detect improper transportation or mishandling of the modules during installation, by comparison with a control module of the same design. For these parameters to be effective, the test conditions should be similar.

In the second part of the chapter, the same methodology was applied on cell-level, and used to derive diagnostic parameters such as the inactive cell area $IMA_{EL\text{-}Cell}(k)$ and the spread of the cell EL intensity $STD_{Cell}(k)$. These cell-level diagnostic parameters can be used to quantify the severity and distribution of the cell degradation/damage in the module, as well as determine the level of mismatch

between the solar cells in the modules, which can be used as an indicator of module quality. Moreover, these parameters can be adapted and have different interpretations depending on the degradation/failure mode investigated. For example the $IMA_{EL\text{-}Cell}(k)$ can be used to quantify the risk of power loss in the modules, by determining the size of the cell fractures for each cell.

The last part of the chapter demonstrated the application of the method to quantify: (i) mechanical degradation of the solar cells, (ii) PID of the solar cells, (iii) and cell interconnect degradation, in PV modules. Based on these results we proposed this method be used to rate cell degradation/failures or quality of modules after transportation, installation, or field operation. Moreover, the method can be automated and used in quality control for module manufacturers or installers, or as a diagnostic tool by plant operators and diagnostic service providers.

The method can be enhanced by combining it with analytical EL diagnostic methods, to calculate the actual voltage and series resistance distribution in the module, and use this information to classify cell-level failures and rate their severity.

CHAPTER 5 DIAGNOSTIC METHODS AND SYSTEMS FOR PV PLANTS

The chapter presents methods for detecting power loss due to shading, increased series resistance, and PID affecting PV arrays. Three practical diagnostic methods are proposed, that can be implemented in a PV plant, depending on the hardware available.

5.1 INTRODUCTION

This chapter presents three diagnostic methods for detecting power loss, degradation, and faults affecting PV arrays, as well as demonstrates the practical application of these methods in the field. The methods differ between them based on the sensors and measurements required, which are closely linked to the detection accuracy of the method, and the possibility of identifying the cause of the power loss.

Most of the experimental data required for developing and validating the operation of these diagnostic methods on PV arrays, was acquired using a PV system monitoring platform presented in Publication VII and shortly described in section 5.2.

Using this monitoring platform, we developed a simple PV array condition monitoring method that uses a model-based approach to detect power loss in the PV array, and is capable of self-parameterization, lending itself to direct implementation in the PV inverter. The details of method are presented in Publication VIII, whereas the main ideas and results are described in section 5.3 of this chapter.

Next, we investigated methods for identifying the cause of the power loss in the PV array, by measuring and analyzing its I-V characteristic. We focused on detecting power loss due to shading of the array in Publication IX, and due to increased series resistance in Publication X. These two diagnostic methods were fine-tuned and integrated in an I-V based diagnostic system for PV modules and arrays, detailed in Publication XI, for which we show the main ideas and results in section 5.4.

PV array diagnostic methods can alternatively be used to optimize the control and operation of the PV system. Such an application is presented in Publication XII, where a simple partial shading detection method is used to improve the MPPT operation of the PV inverter. The main ideas and results of this method are shown in section 5.5 of this chapter.

5.2 PV SYSTEM MONITORING PLATFORM

Developing PV system diagnostic methods poses two important challenges: (i) obtaining sufficient and reliable measurement data for characterizing the system operation during normal conditions and faults; (ii) and testing the diagnostic method under realistic field conditions.

For overcoming these challenges we developed a low-cost and flexible monitoring system for PV plants, depicted in Figure 5.1, and detailed in Publication VII. Compared to classical PV monitoring solutions which can require dedicated hardware and/or specialized data logging systems, the monitoring system we propose allows parallel monitoring of PV plants with different architectures and locations by taking advantage of the intrinsic monitoring capabilities of the inverters and their internet connectivity.

When considering these intrinsic monitoring capabilities, most PV inverters only measure system parameters such as input/output current and voltage, as well as power and energy production. However, the inverter could be also programmed to monitor the partial or full I-V characteristic of the PV array, depending on its hardware topology. Such measurement data can provide a wealth of diagnostic information about the state of the PV array. Measuring the full I-V characteristic (from 0 V to V_{oc}) of a PV array requires a PV inverter with a boost stage, as the commercial string inverter solution presented in [93]. Whereas, a single stage PV inverter can measure the partial I-V characteristic (from a minimum dc bus voltage to V_{oc}) of the PV array.

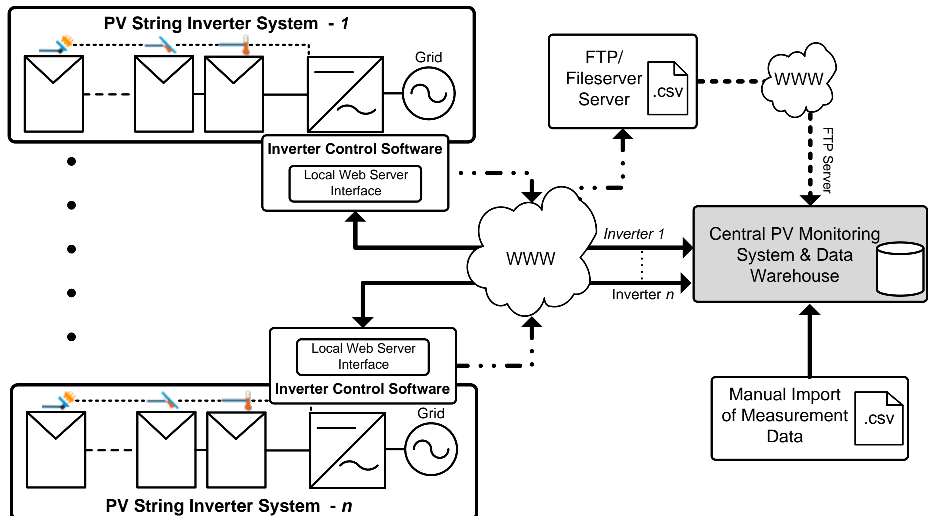

Figure 5.1: PV plant remote monitoring system.

The novelty of the PV monitoring platform in Figure 5.1, is that it takes into account both these intrinsic inverter monitoring capabilities. This is achieved using a software system capable of collecting both PV system production and I-V curve measurements from the inverters within each PV plant monitored. The monitoring software stores the measurements in a data warehouse optimized for managing and data mining large amounts of data, from where it can be later analyzed.

Monitoring both PV system production and PV array I-V curve measurements, opens the possibility for smarter diagnostic and condition monitoring systems that can provide more detailed and relevant diagnostic information to the plant operator.

In the current stage of development, the PV monitoring platform is being used as a data collection and performance monitoring tool. PV array measurements obtained with this platform were used to develop and test the PV array diagnostic methods described in the next sections.

In the next stage of development, these diagnostic methods will be implemented directly in the PV monitoring platform, to perform long term field testing and validation of the diagnostic methods.

In the final stage of development, the PV monitoring platform will become a full-fledged PV condition monitoring system for automatic supervision and diagnostic of PV plants, that can be offered as a service to PV plant operators.

5.3 FAULT DETECTION BASED ON PERFORMANCE MODELLING

5.3.1 DIAGNOSTIC METHOD

The first fault detection method developed using the PV monitoring platform uses a model-based approach to predict the power output of the PV array based on ambient sensor measurements, and to detect power loss or faults affecting the system.

Generally, such model-based diagnostic methods can be very helpful in monitoring various system parameters that characterize the condition of the PV system; and can achieve a high fault-detection rate, if properly parameterized. However, one common limitation of these methods is obtaining accurate model parameters of the system, which typically requires an offline system identification or modelling step performed by an expert user.

A possible solution to this limitation is presented in Publication VIII, where we propose a method to identify the PV model parameters online, from PV inverter measurements, acquired during the operation of the PV system.

The core of this diagnostic method is the Sandia Array Performance Model (SAPM) [117], which is a *point-value model* used in PV system design and analysis, that can estimate the P_{max} of the PV array within 1% accuracy [118]. In a typical use-case scenario, the SAPM parameters of a particular system can be accurately

identified by performing a series of outdoor [117], or indoor [119] pre-tests on modules. Whereas, the method we propose, parameterizes the model from measurements acquired by the PV inverter, during operation, such as plane-of-array (POA) irradiance, module temperature, and the P_{max} of the PV array.

These system variables are monitored periodically using ambient sensors and the MPPT of the solar inverter (which estimates the P_{max}), or alternatively use I-V scans (if the solar inverter has this capability) to measure the real P_{max} of the PV array. Parameterizing the model this way lowers its prediction accuracy (±5% of P_{max}), however it greatly simplifies the parameter identification procedure and lends itself to implementation in PV inverter control software.

The actual parameter identification of the model is performed in a *learning phase* of the diagnostic system, when P_{max}, POA irradiance, and module temperature measurements are collected for a predetermined period of time, when the system is assumed to be working nominally. Part of this training data is then used to calculate the model parameters by *linear regression* of a generic PV performance model derived from the SAPM, and detailed in Publication VIII.

The resulting candidate model is validated using parameters calculated by residual analysis, the coefficient of determination, and by evaluating the accuracy of the model with data which was not used in the training. If the model is not validated, its structure is optimized using a stepwise regression procedure, where terms from candidate model are added or removed successively. This process is repeated automatically until a sufficiently accurate model is determined.

The learning phase is first performed after the commissioning of the PV system, to determine an initial model of the PV array with a lower accuracy, and can be reactivated periodically, to increase its accuracy, and take into account seasonal variations and the natural ageing of the PV system.

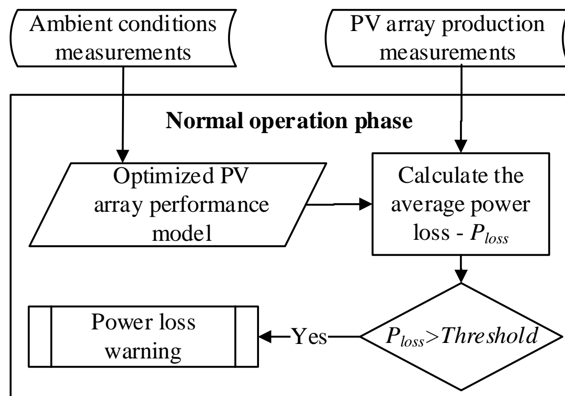

Figure 5.2: Normal operation phase, when the PV array production data is monitored, together with the ambient conditions.

If the candidate model is validated, the diagnostic system enters the *normal operation phase*, shown in Figure 5.2, where irradiance and module temperature measurements are used as inputs to the PV array performance model to predict/estimate the P_{max} of the PV array. The system then compares the predicted and measured P_{max} values to calculate an average power loss P_{loss} of the PV array.

If the P_{loss} is above a preset threshold value, a warning is issued to the plant operator. This threshold value is directly related to the prediction accuracy of the performance model, the accuracy of the P_{max} measurements, and that of the irradiance and module temperature sensors.

The quality of the P_{max} measurement data has to be considered for obtaining an accurate performance model, especially when the P_{max} is estimated using the MPPT of the inverter. This can be a problem during high irradiance variability events, such as fast moving clouds, when the MPPT can no longer accurately track the P_{max} of the PV array. Alternatively, inverters could do a fast scan of the I-V curve of the PV array, to determine the real P_{max}, and overcome this limitation. These issues are further discussed in the next section, where the diagnostic method is experimentally validated, and the two methods for determining the P_{max} of the PV array are compared.

5.3.2 EXPERIMENTAL VALIDATION

The experiments are performed on a PV array consisting of eight multicrystalline Si (BPMSX120) modules connected to a Danfoss TLX Pro inverter. The measurement data is collected using the PV monitoring platform described in section 5.2.

In the first study case, the PV array's P_{max} is estimated by the inverter MPPT, by simply measuring the dc output power of the PV array, assuming the MPPT keeps the operating point near the real P_{max}. In the second case, the P_{max} is determined from the I-V scan of the PV array, measured by the same inverter.

To test the fault detection capability and accuracy of the diagnostic method, we devised three PV array power loss/degradation scenarios, shown in Figure 5.3.

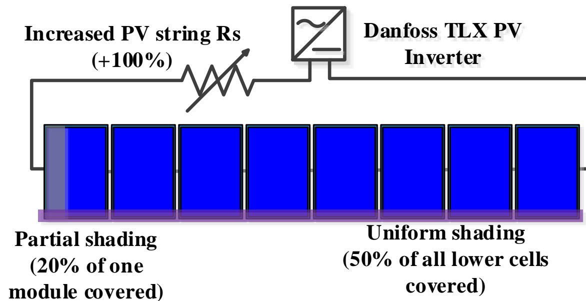

Figure 5.3: Field test setup consisting of a PV string (eight modules) and a commercial string inverter, for performing three test scenarios:(i) the PV string series is increased by +100%;(ii) 20% of one module is shaded;(iii) 50% of all lower cells in the string are shaded.

In the first scenario, the total *series resistance* of the PV array was *increased* with 100%, by connecting a resistor in series with the PV array and inverter, which produces effects similar to the degradation of the electrical circuit of the PV array.

In the second scenario, 20% of one of the eight PV modules in the array was fully covered, generating a small *partial shading* effect.

Last, 50% of all lower cells in the array were fully covered, to generate a uniform shading effect on the PV array I-V characteristic. Representative I-V curves of each scenario, translated to STC, are shown in Figure 5.4.

In the first study case, several days of one-minute averaged PV array dc output power measurements are collected by the inverter. The dc output power is acquired using the inverter's data logging capabilities, whereas the POA irradiance and module temperature are measured with a digital silicon irradiance sensor.

Since the measurements contain both clear sky and cloudy sky data, they are filtered using the procedure described in Publication VIII.

After filtering out the cloudy sky data, we use the POA irradiance, temperature sensor measurements, and the MPPT measured P_{max} (dc output power of the PV array), acquired during the normal operation period of the PV system, to calculate a PV array performance model, as described in the previous sections. To validate the model we compare MPPT measured vs. the model predicted P_{max} power, shown in red in Figure 5.5, and with the ideal/expected power (shown in cyan).

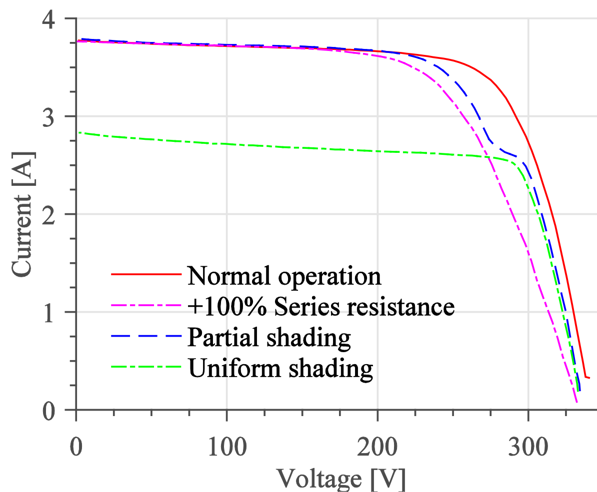

Figure 5.4: I-V curves of a mc-Si PV array affected by different types of shading and increased series resistance: red – normal I-V curve, magenta - +100% increase in the series resistance of the PV array; blue – partial shading affecting 20% of one PV module (8 total); green – uniform type shading similar to dirt accumulation on 50% of the surface of all lower solar cells. All I-V curves were acquired under similar irradiance and temperature.

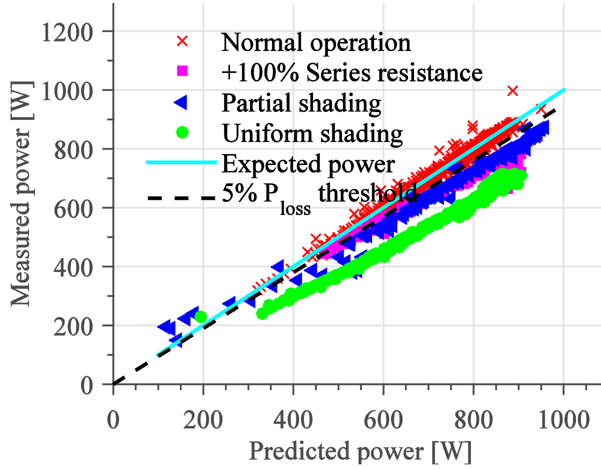

Figure 5.5: Predicted vs. measured power for the case when the performance model is trained with MPPT of one minute averaged data, measured with a commercial inverter.

As can be observed from the results in Figure 5.5, the normal operation predicted P_{max} is below the 5% power loss threshold (shown in black), imposed as the detection threshold of the diagnostic method. However, some P_{max} estimates are above the 5% threshold, which is to be expected when using the MPPT estimated P_{max}. Such false alarms due to outliers can be avoided by averaging the power loss factor over a larger time window.

Next we analyze the predicted P_{max} power for the three fault/power loss scenarios: (i) increased series resistance of the PV system (shown in magenta in Figure 5.5); (ii) partial (shown in blue); (iii) and uniform (shown in green) shading. Here we can observe that in most cases the power loss is above 5% (the threshold limit), and can be detected by the diagnostic method.

In the second study case the P_{max} data is extracted from the I-V characteristic of the same PV array, measured periodically (every 10 minutes) with the same inverter, during the same period as in the previous case. From a power loss perspective, sweeping the I-V curve every 10 minutes is reasonable, considering that for an 11 hour daylight operation of the PV system during clear sky conditions, 6.19 kWh dc energy was produced, 65 I-V sweeps were performed, and 0.00413 kWh was lost due to I-V sweeping, which is below 0.1% of the total energy produced.

To make comparison possible with the previous study case, the irradiance and module temperature were measured using the same sensors.

In the learning phase, the performance model is parameterized using I-V curves of the array measured at various irradiances and temperatures, in normal operation conditions, over a period of several days. A very accurate prediction of the P_{max} can be achieved in this case, as can be observed from the normal operation data (red markers) in Figure 5.6.

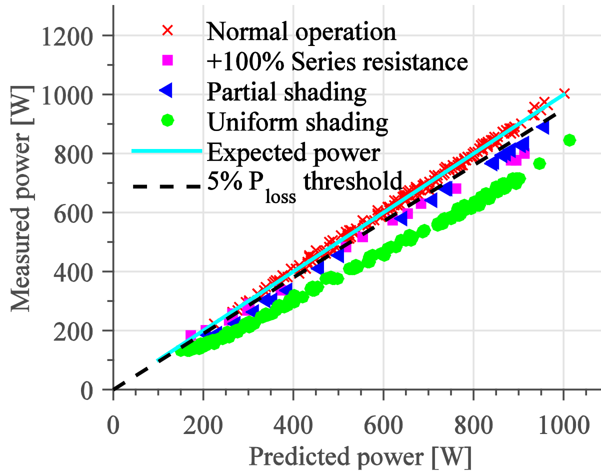

Figure 5.6: Predicted vs. measured power for the case when the performance model is trained with data extracted from I-V curves, measured with a commercial inverter.

Since the I-V curves were acquired in identical conditions with the previous case (same PV array, inverter, ambient sensors, same partial shading, and during the same period), a comparison can be made between MPPT/dc output power based performance model (Figure 5.5) and real P_{max}/I-V curve based performance model (Figure 5.6). As can be observed from the results in Figure 5.6, the real P_{max} extracted from the I-V curve makes it possible to detect even relatively small power losses, with high accuracy (< 5% P_{max}), and low modelling efforts.

The method can be further developed by employing a lookup table of performance model parameters, corresponding to different time periods of the year, to remove the effect of seasonal variations. Moreover, including time as model variable, certain PV array ageing effects could be captured and predicted by the model. These ideas will be explored in a future publication.

5.4 FAULT DETECTION BASED ON I-V CHARACTERIZATION

5.4.1 DIAGNOSTIC METHOD

The second PV plant diagnostic method developed in this work focuses on identifying the cause of the power loss in the PV system, be it shading of the PV array, increased series resistance due to degradation of the electrical circuit of the PV array and module components, or PID of the solar cells.

The diagnosis is achieved by measuring and analysing changes in the I-V curve of the PV array. The diagnostic method is based on diagnostic parameters that are easy to calculate from the shape of the I-V curve; this proves to be an advantage when diagnosing PV arrays affected by shading for example, where other model based

diagnostic methods, such as curve fitting the I-V curve to the diode model would fail. This renders the method machine-analysis friendly and suitable for implementation in the power electronic converter.

The diagnostic parameters and logic of the method were derived from module level tests on standard crystalline silicon PV modules. These parameters were normalized to a per-unit basis to remove dependency on system configuration. Additionally, the diagnostic logic was formalized using fuzzy logic sets and rules, lending robustness and flexibility to the diagnostic method, such that it can be applied to a wide range of standard crystalline silicon based PV systems.

Some of the diagnostic parameters and logic for detecting partial shading from I-V measurements were initially derived in Publication IX. Whereas the diagnostic method for detecting increased series resistance losses in PV arrays, were first investigated in Publication X. This diagnostic methodology was improved in Publication XI, and integrated with a similar method to detect PID, into a complete PV array *diagnostic process* that can be implemented directly in the string inverter, provided that it can measure the full I-V curve. In practice this requires a converter with a boost stage, such as the commercial string inverter [93] used by the PV monitoring platform presented in section 5.2, which already has the I-V sweep functionality implemented.

The diagnostic process is explained step-by-step in Publication XI, and is shortly described next. The diagnostic process consists of three main stages shown in Figure 5.7. In the first stage, the I-V curve of the PV array is measured, along with the in-plane irradiance (G). Typically, the irradiance sensor is optional, since the effective irradiance can be estimated to a certain degree from the I_{sc} of the PV array.

In the second stage of the diagnostic process, if G is too low (<500 W/m^2) the diagnostic process is stopped. The reasoning behind this verification is that the effects of shading or increased series-resistance are most visible in I-V curves taken at high irradiance conditions. Therefore, in order to maximize the detection rate of the diagnostic system and avoid false detection events, the diagnostic process should be performed only under such conditions.

If the irradiance is sufficiently high for the diagnostic process to continue, the measured I-V curve is pre-processed by filtering any measurement noise.

Next, a set of *diagnostic indicators* are calculated from the pre-processed I-V curve, and normalized to relative per-unit values (relative to a base value calculated in the initial commissioning phase of the diagnostic system), in order to maintain independence from system parameters. The derivation and experimental analysis of these diagnostic parameters, along with the normalization procedure, is presented in detail in Publication XI.

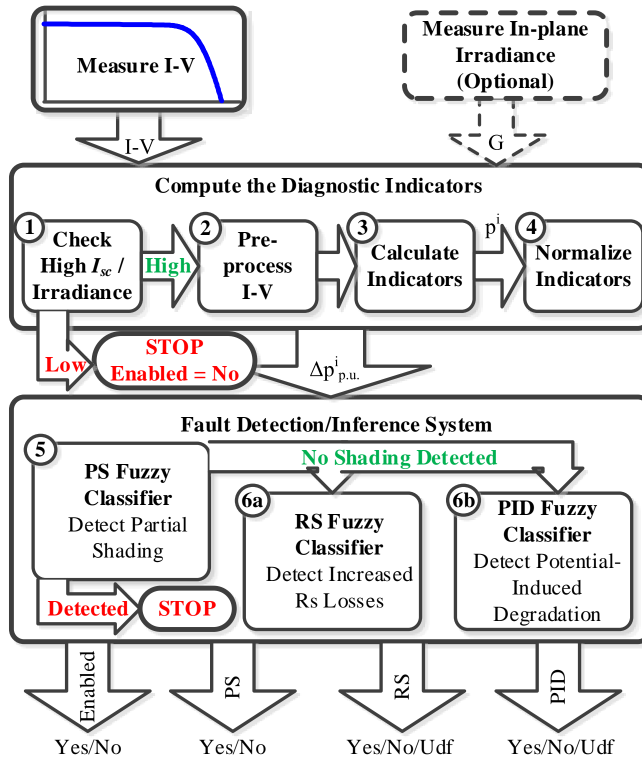

Figure 5.7: Structure of the diagnostic system based on light I-V measurements.

Last, in the third stage of the diagnostic process, the normalized diagnostic indicators are analysed automatically by a diagnostic system, which detects if the PV array is affected by partial shading, increased series-resistance losses, or PID. The detection logic of the diagnostic system is implemented in three *fuzzy classifiers* [120, 121], denoted as: *PS Fuzzy Classifier* – for detecting the presence of shading; *RS Fuzzy Classifier* – for detecting increased series-resistance losses; *PID Fuzzy Classifier* – for detecting PID.

At the end of the diagnostic process four output variables are generated: *Enabled (Yes/No)* – the diagnostic process was possible and ran successfully; *PS (Yes/No)* – the presence of partial shading was detected; *RS (Yes/No/Udf)* – increased series-resistance losses were detected; *PID (Yes/No/Udf)* – PID was detected.

In case the irradiance is too low, the *Enabled* output is set to *No*, in order to signal to the external systems or user that the diagnosis was not performed. Moreover, if shading has been detected, the *RS* and *PID* outputs are set to *Udf – undefined*, in order to avoid false detection alarms, due to the shading. The structure and operation of the fuzzy classifiers, and the derivation of the diagnostic rules are presented in more detail in Publication XI.

5.4.2 DETECTION PERFORMANCE

To quantify and optimize the fault detection performance of the diagnostic method we used *Receiver Operation Characteristic* (ROC) analysis, which is a method for analysing and optimizing the detection performance of diagnostic/classification systems in terms of *detection* and *false alarm rate* [122]. For performing this analysis, we used a test dataset, detailed in Publication XI, which consists of 740 I-V curves of crystalline silicon PV modules, measured on a solar simulator in different test conditions of shading (uniform and partial), increased series resistance, and PID.

The test dataset was evaluated for each fuzzy classifier repeatedly, during which a classifier optimization parameter denoted as *score threshold*, was swept from 0 to 1, resulting in a detection and false alarm rate for a range of threshold values. By plotting these rates on an *x-y*, as shown in Figure 5.8, the performance curves of the classifiers were obtained [122], and the optimal threshold values for the fuzzy classifiers was determined.

The performance of the *PS Fuzzy Classifier* was evaluated in two scenarios: (i) the detection system is equipped with an in-plane irradiance sensor – thus the uniform type shading can be detected; (ii) no irradiance sensor measurements are available – uniform shading cannot be detected, only partial type shading.

The performance curve for first shading scenario (red curve in Figure 5.8) shows a high *detection rate* = 1, such that all instances of partial and uniform shading are detected successfully by the *PS Classifier*.

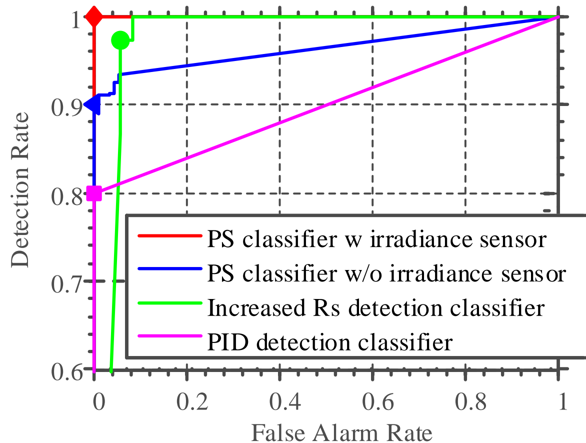

Figure 5.8: Performance curves of the three fuzzy classifiers: red – partial shadow classifier with irradiance sensor – for detecting uniform partial shadow types (shading 6); blue – partial shadow classifier without irradiance sensor; green – classifier for detecting increased series-resistance losses; magenta – classifier for detecting PID.

In the second scenario (blue curve in Figure 5.8), the *optimal detection rate* = 0.9 is lower, since the uniform shading test cases are not detected.

The performance curve of the *RS Fuzzy Classifier* (green curve in Figure 5.8), using an irradiance sensor, shows a high *detection rate* = 0.97. There are also some instances of false alarms (*false alarm rate* = 0.057), where the diagnostic system incorrectly classifies I-V curves affected PID as increased series-resistance losses. This is a sensitivity limitation of the diagnostic method. Similarly, for the *PID Fuzzy Classifier* (magenta performance curve in Figure 5.8), using irradiance measurements, we calculated a *detection rate* = 0.8.

5.4.3 EXPERIMENTAL VALIDATION

The diagnostic method presented in this work, together with the classifier parameters (fuzzy sets, diagnostic rules, and threshold values), determined in the previous sections, can be implemented "as is" in the field, by taking advantage of the I-V measurement (sweep) capabilities of the inverters.

To demonstrate the practical application and operation of the diagnostic system, we developed a field test setup, shown in Figure 5.9. The test setup consists of a 0.9 kWp PV string (eight multicrystalline silicon modules connected in series), a Danfoss TLX Pro string inverter [93], capable of measuring the I-V curve of the PV string every 10 minutes, and a variable resistor connected in series with the string. Based on this setup, we devised two study cases for testing the operation of the diagnostic system in the presence of shading or increased series resistance of the PV string.

The variable shading study case, depicted in Figure 5.9, resulted by placing a 100x30 cm plank in front one of the PV modules, similar to the shadow caused by a chimney. In the second study case, the series resistance of the PV string was increased with 50%, by connecting a resistor in series with the PV string and solar inverter.

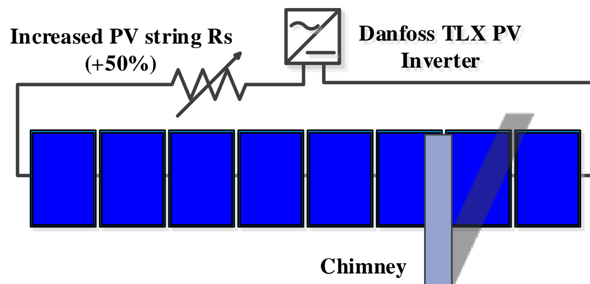

Figure 5.9: Field test setup consisting of a PV string (eight crystalline silicon modules connected in series), a commercial string inverter capable of measuring the I-V curve of the PV string every 10 minutes, and a variable resistor connected in series with the string.

For both study cases, string I-V measurements and in-plane irradiance were acquired every 10 minutes for the duration of one day.

Commissioning phase for the field test setup

In the commissioning phase of the field test setup the I-V characteristic of the PV string was recorded by the inverter for a period of two weeks, when the system was unaffected by shading or increased series-resistance losses. The resulting high irradiance (900 W/m^2−1100 W/m^2) I-V curve data was used to calculate the base values for the diagnosing indicators, as described in Publication XI. These base values were then used in the indicator normalization for the following study cases.

Case 1 – Partial shading

The results of this study case are shown in Figure 5.10, where the P-V characteristic curves are plotted for the period of one day, when the system was affected by shading. As can be observed from the green P-V curves, the shading is not present in the morning hours. After some time, the obstacle starts to create significant shading on the PV string, and the shading is detected (red P-V curves) by the diagnostic system.

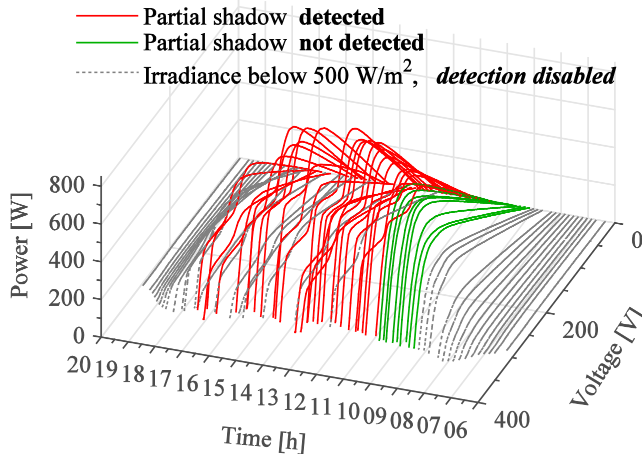

Figure 5.10: Test PV string affected by variable shading, due to an obstacle placed in front of one of the PV modules.

Case 2 – 50% Increase in the PV string series resistance

In the second study case we tested the increased series detection capabilities of the diagnostic system, at the lower sensitivity limit of the diagnostic indicators. This was achieved by artificially increasing the series resistance of the PV string by 50%, using an external resistor, as depicted in Figure 5.9.

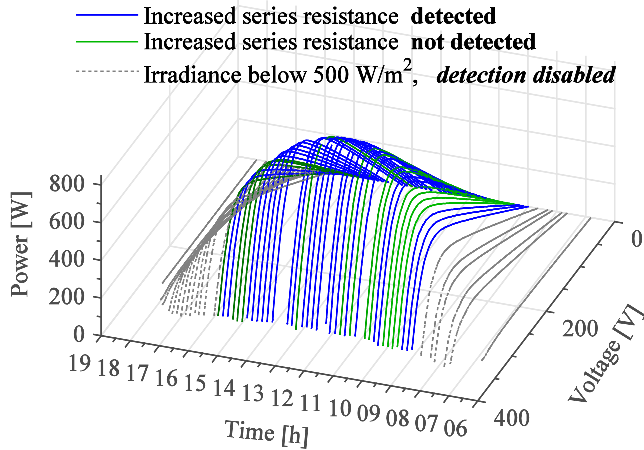

Figure 5.11: Test PV string affected increased series resistance (+50%). For some of the lower irradiance cases, the increased series resistance is not detected, since the detection system is at the lower limit of sensitivity.

As can be observed from Figure 5.11, the diagnostic system is able to detect the degradation mode in most of the cases (blue curves in Figure 5.11). But as the irradiance is lower, the detection rate decreases as well, since the series-resistance losses are less significant/visible at lower irradiance/current conditions.

The PID detection function was not tested in the field, only on module level, and requires a larger dataset of PV modules affected by PID to improve and validate. However, as was shown in Chapter 3 and Publication VI, there are several other I-V parameters that can be used to improve the detection of this degradation mode. These issues will be explored in the future, when more PID module data is available.

The next step in the development and field validation of this method is to integrate it in the PV monitoring platform, and perform long term testing and monitoring of different PV systems with different module designs and configurations.

5.5 OPTIMIZED MPPT OPERATION USING PARTIAL SHADING DETECTION AND I-V CHARACTERIZATION

5.5.1 DIAGNOSTIC METHOD

In addition to warning the plant operator about power loss and faults occurring in the PV plant, diagnostic methods can be used to improve the control and performance of the PV system during non-optimal operation conditions. An example of such a situation is for PV systems frequently affected by partial shading. This can lead to the creation of multiple MPPs on the array's P-V curve that can confuse the inverter's MPPT, and degrade the performance of the PV system.

To overcome this problem we proposed a simple and practical solution in Publication XII, where we use a partial shading detection method to improve the MPPT operation of the inverter when the PV system is affected by shading. The concept of this method, denoted iMPPT, is depicted in Figure 5.12, where a partial shadow detection unit is continuously monitoring the state of the PV array, and in case it detects the presence of shading it triggers an automatic I-V scan to detect the position of the global MPP (P_{max}), and corrects the MPPT with the new position (V_{ref}) if necessary.

The actual partial shading detection is performed by monitoring the V_{mp} voltage, estimated by the MPPT. During normal operation of the PV system, the V_{mp} varies mainly due to changes in irradiance and temperature, for which we can determine the minimum and maximum values, and set a *normal operation zone* for the V_{mp}. Moreover, by using ambient sensors, we can predict these changes in V_{mp} using a PV model, and can then narrow the normal operation zone of the V_{mp}.

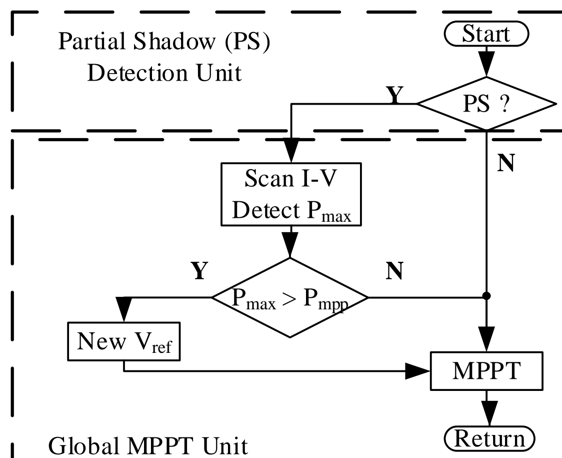

Figure 5.12: Intelligent MPPT algorithm.

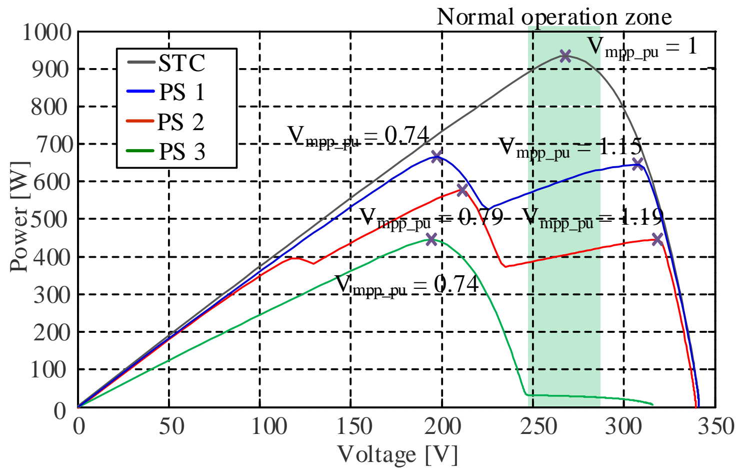

Figure 5.13: Power-voltage characteristic of a PV array in normal operation, and affected by three different partial shadows.

However, in case of partial shading and the formation of multiple MPPs, the value of the V_{mp} voltage can change significantly, as shown in Figure 5.13, where we show the STC I-V curve of a PV array affected shading of different sizes and locations.

Considering this behavior, we can detect partial shading events that cause the V_{mp} to move outside the normal operation zone. More details about the derivation of this method can be found in Publication XII.

One important advantage of this method is its simplicity, however, more advanced partial shading detection methods, such as the one presented in section 5.4, can be implemented instead. Moreover, the shading detection can be combined with any MPPT algorithm, such as P&O, as is the case in the present work. Last, the method requires only a partial scan of the PV array's I-V curve, and can be implemented in most inverter topologies.

5.5.2 EXPERIMENTAL VALIDATION USING THE PV MONITORING PLATFORM

To test the operation of this method, we used the PV monitoring platform, described in 5.2, to acquire 10 minutes I-V scans for a PV array affected by different types of partial shading, over the course of several days. This measurement data was then used to evaluate the operation of a simple P&O MPPT in the presence of shading, compared to the proposed iMPPT method.

Next we present two relevant days of operation: (i) one day when the array is affected by variable shading, such as shading from a chimney (Figure 5.9); (ii) and one day when the PV array is affected by constant shading, when several cells are

covered constantly the entire day. More details and results are given in Publication XII.

In the first example, shown Figure 5.14, both the P&O (black line), and the proposed iMPPT (red line) methods, track the ideal/global MPP (blue line).However, as the position of the sun changes relative to the obstacle placed in front of the array, partial shading is generated on the array, and the P&O losses track the global MPP and continues to track a local MPP. Nonetheless, the iMPPT detects that the V_{mp} is outside the normal operation zone, triggers and I-V scan to find the global MPP, and corrects the position of the MPPT. By calculating the efficiency of the two MPPT methods for this day, as the ratio between the actual energy yield during the considered day and the maximum possible energy yield from the array, we find that the simple P&O has an efficiency of 84.6 %, whereas the iMPPT has 99.4 % efficiency.

Another illustrative example of the operation of this method, is presented in Figure 5.15. Here, part of PV array is shaded constantly, similar to the effect of soiling or snow on the PV array. In this situation, there is a chance that the MPPT is locked on the local MPP from the beginning of the day, as illustrated by the black line in Figure 5.15, and never gets to find the global MPP. However, the iMPPT is able to detect the shading early on, and set the MPPT to the correct position. The efficiency of the P&O in this case is 75%, whereas the iMPPT is close to 99.9%.

The method was also implemented and tested on a flexible PV inverter setup described in Publication XII, demonstrating the practical application of the method.

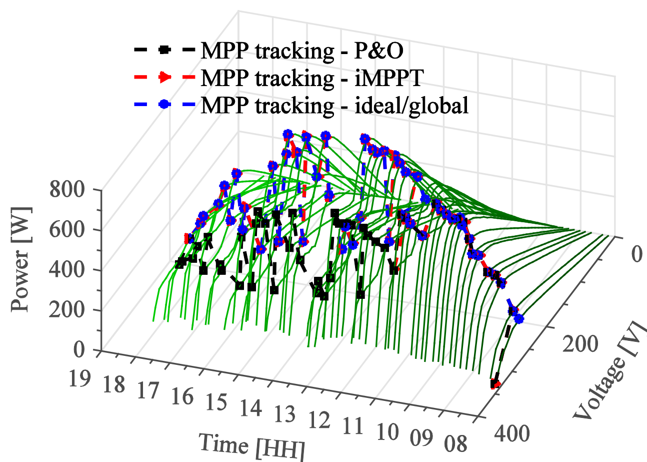

Figure 5.14: Comparison P&O and iMPPT operation during variable shading.

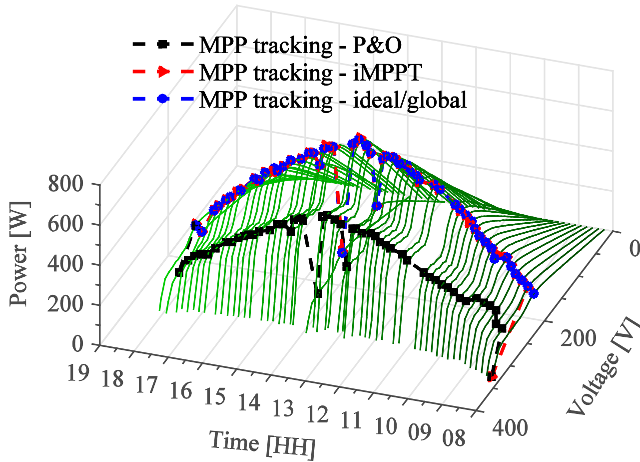

Figure 5.15: Comparison of P&O and iMPPT operation during constant shading.

5.6 SUMMARY AND CONCLUSIONS

This chapter introduced three diagnostic methods for detecting failures and degradation occurring in PV arrays that can be implemented in the control software of the inverters or as part of the condition monitoring system of the PV plant.

These methods were developed and validated using a PV monitoring platform that can acquire PV array production and I-V curve measurements directly from the solar inverters in the PV plant.

The first PV plant diagnostic method developed using this platform uses a performance model of the PV array to predict its maximum power from irradiance and temperature sensor measurements. The novelty of the method comes from its ability to (automatically) self-parameterize the performance model from measurements acquired by the PV inverter after the PV system has been commissioned, and does not require a dedicated system modelling effort. The method shows a good power loss detection accuracy (>5%), considering its simplicity, and is suitable for implementation in PV inverters equipped with, or with access to (through communication) irradiance and module temperature sensors.

The second type of PV plant diagnostic method developed can operate without ambient sensors, and is based on measuring and analyzing parameters of the light I-V curve of the array. Experimental results showed that the I-V based diagnostic method can detect and identify shading and increased series-resistance losses affecting PV arrays, with high accuracy. Moreover, preliminary results were shown on how this method can be used to detect PID in crystalline silicon modules. The method can be

implemented in PV inverters with a boost stage, capable of tracing the I-V characteristic of the PV array. Moreover, this method does not require an irradiance sensor, although, if one is available, it can improve its performance.

The last part of this chapter showed how integrating a partial shading detection method, into the MPPT controller of the PV inverter, can optimize the operation and performance of the PV system under shading conditions.

CHAPTER 6
CONCLUSIONS

The main conclusions of the thesis are underlined in this chapter along with several recommendations for future work regarding areas that could be further investigated.

6.1 THESIS SUMMARY

This thesis investigated diagnostic methods for characterizing and detecting degradation modes in crystalline silicon PV modules and arrays and was focused on two main subjects: (i) PV module characterization and diagnostic methods for use in module diagnostics and failure identification, accelerated stress testing, and degradation studies, investigated in **Chapter 2** and **Chapter 3**; and (ii) diagnostic methods for PV arrays that are suitable for implementation in the solar inverter or incorporated in a condition monitoring system, investigated in **Chapter 4** and **Chapter 5**.

Chapter 2 introduced an in-situ module power degradation monitoring method for crystalline silicon PV modules undergoing PID stress testing, and discussed its advantages and limitations. A solution for automatizing the in-situ monitoring method was proposed, and used to investigate the effects of PID on the power degradation estimation from dark I-V measurements taken at different temperatures. Based on this investigation, a method was proposed on how to compensate these temperature effects, and characterize module power degradation directly at stress temperature, thus reducing testing time and improving the data collection process.

The advantages and potential of this solution were exemplified in the last part of the chapter, where a PID temperature acceleration model was developed for crystalline silicon PV modules, based on the Arrhenius model and accelerating life testing procedures.

Chapter 3 proposed a PV module diagnostic method that can identify: (i) optical losses and degradation, (ii) degradation of the electrical circuit of the PV module, (iii) mechanical degradation of the solar cells, (iv) PID of the solar cells.

The method is based on the complementary analysis of the light and dark I-V characteristics of the PV module, has low computational requirements and is machine analysis friendly. Moreover, the method has potential for field applications such as implementation in I-V tracers for long-term reliability monitoring of PV modules, with the goal of identifying the onset and progression of the different degradation modes, without the need of periodic inspection and imaging. Another possible

application would be in module-integrated converters capable of bidirectional current flow, where the method can be used to optimize maintenance operations by scheduling appropriate actions based on the severity and type of degradation affecting the PV modules.

Chapter 4 proposed a method for quantifying the extent of different failures and degradation modes present in crystalline silicon PV modules by analyzing the EL intensity distribution obtained by imaging the modules.

First, the methodology was presented for analyzing the module level EL intensity distribution, introducing the concepts of bimodal distribution thresholding, calculation of the active/inactive area map, and use of the ELI distribution summary statistics in analyzing the module EL image.

Next, the methodology was applied on cell-level, and used to derive diagnostic parameters such as the inactive cell area and the STD of the ELI distribution.

The last part of the chapter showed experimental results from the application of the method to quantify: (i) mechanical degradation of the solar cells, (ii) PID of the solar cells, (iii) and cell interconnect degradation, in PV modules.

Chapter 5 introduced three diagnostic methods for detecting failures and degradation occurring in PV arrays that can be implemented in the control software of the inverters or as part of the condition monitoring system of the PV plant.

These methods were developed and validated using a PV monitoring platform that can acquire PV array production and I-V curve measurements directly from the solar inverters in the PV plant.

The first PV plant diagnostic method developed using this platform uses a performance model of the PV array to predict its maximum power from irradiance and temperature sensor measurements. The novelty of the method comes from its ability to (automatically) self-parameterize the performance model from measurements acquired by the PV inverter after the PV system has been commissioned, and does not require a dedicated system modelling effort.

The second type of PV plant diagnostic method developed can operate without ambient sensors, and is based on measuring and analyzing parameters of the light I-V curve of the array. Experimental results show that the I-V based diagnostic method performs well in identifying both shading and increased series-resistance losses affecting PV arrays. Moreover, preliminary results were shown on how this method can be used to detect PID in crystalline silicon modules.

The last part of this chapter showed how integrating a partial shading detection method, into the MPPT controller of the PV inverter, can optimize the operation and performance of the PV system.

6.2 FUTURE WORK

The possibility for future work remains and can advance in several directions. The main lines of research areas that could be interesting to be explored are listed as it follows:

Characterization of module power degradation for PID accelerated lifetime testing:

- Use this method to model other PID stress factors such as voltage and humidity with the associated failure mechanisms, and eventually integrated into a multi-stress acceleration model.
- Improve the method to take in account additional real-world factors such as illumination and PID recovery.

Module degradation and failure mode identification based on the light and dark I-V characteristics:

- Improve the method for outdoor operation, it needs to take into consideration the changing ambient conditions as well as stray light.
- Develop an outdoor test setup capable of tracing both the light I-V and dark I-V characteristics of modules, and use it to test and improve the method.

Module degradation and failure diagnosis using electroluminescence imaging:

- Apply the method to analyze the distribution of series resistance, diode voltage, and other diode model parameters, within the module.
- Develop a method for detecting, quantifying, and classifying solar cell microcracks in PV modules.

Diagnostic methods and systems for PV plants:

- Implement the PV plant diagnostic methods in the PV monitoring platform, for long term field testing and validation.
- Improve the fault detection method based on performance modelling by employing a lookup table of performance model parameters, corresponding to different time periods of the year, to remove the effect of seasonal variations.
- Include time as model variable, for predicting PV array ageing effects.
- Improve the PID detection method based on I-V characterization, and validate it on a larger test dataset.
- Integrate it in the PV monitoring platform, and perform long term testing and monitoring of different PV systems with different module designs and configurations.

BIBLIOGRAPHY

1. EPIA, *Global Market Outlook for Photovoltaics 2014-2018*. 2014, European Photovoltaic Industry Association: Brussels.
2. Kost, C, Mayer, J N, Thomsen, J, Hartman, N, Senkpiel, C, Philipps, S, Nold, S, Lude, S, Saad, N, and Schlegl, T, *Levelized Cost of Electricity Renewable Energy Technologies*. 2013, Fraunhofer Institut for Solar Energy Systems ISE: Freiburg, Germany.
3. Masson, G, *Trends 2014 in Phtovoltaic Applications - Survey Report of Selected IEA Countries between 1992 and 2013*. 2014, International Energy Agency. Report IEA-PVPS T1-25:2014.
4. Burger, B, Kiefer, K, Kost, C, Nold, S, Philipps, S, Preu, r, Schindler, R, Schlegel, T, Stryi-Hipp, G, Willeke, G, Wirth, H, Brucker, I, Haberle, A, Schacht, V, and Warmuth, W, *Photovoltaics Report (2014) Updated: 8 September 2014*. 2014, Fraunhofer ISE: Freiburg, Germany.
5. Green, M A, Emery, K, Hishikawa, Y, Warta, W, and Dunlop, E D, Solar cell efficiency tables (version 44). *Progress in Photovoltaics: Research and Applications*, 2014. **22**(7): p. 701-710 DOI: 10.1002/pip.2525.
6. Wohlgemuth, J H. Standards for PV Modules and Components - Recent Developments and Challenges. in *27th European Photovoltaic Solar Energy Conference and Exhibition*. 2012. Frankfurt, Germany DOI: 10.4229/27thEUPVSEC2012-4DP.2.3.
7. Jordan, D C and Kurtz, S R, Photovoltaic Degradation Rates—an Analytical Review. *Progress in Photovoltaics: Research and Applications*, 2013. **21**(1): p. 12-29 DOI: 10.1002/pip.1182.
8. Jordan, D, Wohlgemuth, J, and Kurtz, S, *Technology and Climate Trends in PV Module Degradation*, in *27th European Photovoltaic Solar Energy Conference and Exhibition*. 2012: Frankfurt, Germany. p. 3118 - 3124.
9. Köntges, M, Kurtz, S, Packard, C, Jahn, U, Berger, K A, Kato, K, Friesen, T, Liu, H, and Van Iseghem, M, *Review of Failures of Photovoltaic Modules*. 2014, International Energy Agency. Report IEA-PVPS T13-01:2014.
10. Administration, U S E I, *Levelized Cost and Levelized Avoided Cost of New Generation Resources in the Annual Energy Outlook 2014*. 2014, U.S. Energy Information Administration. p. EIA.
11. Wohlgemuth, J H and Kurtz, S. Reliability testing beyond Qualification as a key component in photovoltaic's progress toward grid parity. in *Reliability Physics Symposium (IRPS), 2011 IEEE International*. 2011. DOI: 10.1109/IRPS.2011.5784534.
12. Park, N C, Jeong, J S, Kang, B J, and Kim, D H, The effect of encapsulant discoloration and delamination on the electrical characteristics of photovoltaic module. *Microelectronics Reliability*, 2013. **53**(9–11): p. 1818-1822 DOI: 10.1016/j.microrel.2013.07.062.

13. Meyer, E L and van Dyk, E E, Assessing the reliability and degradation of photovoltaic module performance parameters. *IEEE Transactions on Reliability*, 2004. **53**(1): p. 83-92 DOI: 10.1109/tr.2004.824831.
14. Laukamp, H, Schoen, T, and Ruoss, D, *Reliability Study of Grid Connected PV Systems, Field Experience and Recommended Design Practice*. 2002, International Energy Agency: Freiburg, Germany. p. 31. Report IEA-PVPS T7-08: 2002.
15. Munoz, M A, Alonso-García, M C, Vela, N, and Chenlo, F, Early degradation of silicon PV modules and guaranty conditions. *Solar Energy*, 2011. **85**(9): p. 2264-2274 DOI: 10.1016/j.solener.2011.06.011.
16. Wohlgemuth, J H, Kempe, M D, and Miller, D C. Discoloration of PV encapsulants. in *Photovoltaic Specialists Conference (PVSC), 2013 IEEE 39th*. 2013. DOI: 10.1109/PVSC.2013.6745147.
17. Piliougine, M, Cañete, C, Moreno, R, Carretero, J, Hirose, J, Ogawa, S, and Sidrach-de-Cardona, M, Comparative analysis of energy produced by photovoltaic modules with anti-soiling coated surface in arid climates. *Applied Energy*, 2013. **112**: p. 626-634 DOI: 10.1016/j.apenergy.2013.01.048.
18. Djordjevic, S, Parlevliet, D, and Jennings, P, Detectable faults on recently installed solar modules in Western Australia. *Renewable Energy*, 2014. **67**: p. 215-221 DOI: 10.1016/j.renene.2013.11.036.
19. Haeberlin, H and Graf, J D, *Gradual reduction of PV generator yield due to pollution*, in *2nd World Conference on Photovoltaic Solar Energy Conversion*. 1998: Vienna, Austria.
20. Woyte, A, Nijs, J, and Belmans, R, Partial shadowing of photovoltaic arrays with different system configurations: literature review and field test results. *Solar Energy*, 2003. **74**(3): p. 217-233 DOI: 10.1016/s0038-092x(03)00155-5.
21. Wendlandt, S, Drobisch, A, Buseth, T, Krauter, S, and Grunow, P. Hot Spot Risk Analysis on Silicon Cell Modules. in *25th European Photovoltaic Solar Energy Conference and Exhibition*. 2010. Valencia, Spain DOI: 10.4229/25thEUPVSEC2010-4AV.3.13.
22. Mäki, A, Valkealahti, S, and Leppäaho, J, Operation of series-connected silicon-based photovoltaic modules under partial shading conditions. *Progress in Photovoltaics: Research and Applications*, 2012. **20**(3): p. 298-309 DOI: 10.1002/pip.1138.
23. Quaschning, V and Hanitsch, R. Influence of shading on electrical parameters of solar cells. in *Photovoltaic Specialists Conference, 1996., Conference Record of the Twenty Fifth IEEE*. 1996. DOI: 10.1109/PVSC.1996.564368.
24. Roman, E, Alonso, R, Ibanez, P, Elorduizapatarietxe, S, and Goitia, D, Intelligent PV Module for Grid-Connected PV Systems. *Industrial Electronics, IEEE Transactions on*, 2006. **53**(4): p. 1066-1073 DOI: 10.1109/TIE.2006.878327.
25. Sera, D, Spataru, S, Mathe, L, Kerekes, T, and Teodorescu, R. Sensorless PV Array Diagnostic Method for Residential PV Systems. in *26th European Photovoltaic Solar Energy Conference and Exhibition*. 2011. Hamburg, Germany DOI: 10.4229/26thEUPVSEC2011-4AV.3.37.

26. Drews, A, de Keizer, A C, Beyer, H G, Lorenz, E, Betcke, J, van Sark, W G J H M, Heydenreich, W, Wiemken, E, Stettler, S, Toggweiler, P, Bofinger, S, Schneider, M, Heilscher, G, and Heinemann, D, Monitoring and remote failure detection of grid-connected PV systems based on satellite observations. *Solar Energy*, 2007. **81**(4): p. 548-564 DOI: 10.1016/j.solener.2006.06.019.
27. Firth, S K, Lomas, K J, and Rees, S J, A simple model of PV system performance and its use in fault detection. *Solar Energy*, 2010. **84**(4): p. 624-635 DOI: 10.1016/j.solener.2009.08.004.
28. Woyte, A, Richter, M, Moser, D, Reich, N, Green, M, Mau, S, and Beyer, H G, *Analytical Monitoring of Grid-connected Photovoltaic Systems*. 2014, International Energy Agency: Brussels, Belgium. Report IEA-PVPS T13-03: 2014.
29. King, D L, Quintana, M A, Kratochvil, J A, Ellibee, D E, and Hansen, B R, Photovoltaic module performance and durability following long-term field exposure. *Progress in Photovoltaics: Research and Applications*, 2000. **8**(2): p. 241-256 DOI: 10.1002/(SICI)1099-159X(200003/04)8:2<241::AID-PIP290>3.0.CO;2-D.
30. Quintana, M A, King, D L, McMahon, T J, and Osterwald, C R. Commonly observed degradation in field-aged photovoltaic modules. in *29th IEEE Photovoltaic Specialists Conference*. 2002. New Orleans, USA DOI: 10.1109/PVSC.2002.1190879.
31. Kato, K, *"PVRessQ!" PV Module Failures Observed in the Field*, in *Photovoltaic Module Reliability Workshop 2012*. 2012, National Renewable Energy Laboratory: Golden, Colorado, USA. p. 13-36.
32. Yang, B B, Sorensen, N R, Burton, P D, Taylor, J M, Kilgo, A C, Robinson, D G, and Granata, J E. Reliability model development for photovoltaic connector lifetime prediction capabilities. in *39th IEEE Photovoltaic Specialists Conference (PVSC)*. 2013. DOI: 10.1109/PVSC.2013.6744115.
33. Chattopadhyay, S, Dubey, R, Kuthanazhi, V, John, J J, Solanki, C S, Kottantharayil, A, Arora, B M, Narasimhan, K L, Kuber, V, Vasi, J, Kumar, A, and Sastry, O S, Visual Degradation in Field-Aged Crystalline Silicon PV Modules in India and Correlation With Electrical Degradation. *Photovoltaics, IEEE Journal of*, 2014. **4**(6): p. 1470-1476 DOI: 10.1109/JPHOTOV.2014.2356717.
34. Bowden, S and Rohatgi, A. Rapid and accurate determination of series resistance and fill factor losses in industrial silicon solar cells. in *17th European Photovoltaic Solar Energy Conference and Exhibition*. 2001. Munich, Germany.
35. Hacke, P and Meier, D L. Analysis of fill factor losses using current-voltage curves obtained under dark and illuminated conditions. in *29th IEEE Photovoltaic Specialists Conference*. 2002. New Orleans, USA DOI: 10.1109/Pvsc.2002.1190559.
36. del Cueto, J A, Method for analyzing series resistance and diode quality factors from field data Part II: Applications to crystalline silicon. *Solar Energy Materials and Solar Cells*, 1999. **59**(4): p. 393-405 DOI: 10.1016/S0927-0248(99)00067-7.

37. Altermatt, P P, Heiser, G, Aberle, A G, Wang, A, Zhao, J, Robinson, S J, Bowden, S, and Green, M A, Spatially resolved analysis and minimization of resistive losses in high-efficiency Si solar cells. *Progress in Photovoltaics: Research and Applications*, 1996. **4**(6): p. 399-414 DOI: 10.1002/(SICI)1099-159X(199611/12)4:6<399::AID-PIP148>3.0.CO;2-4.
38. King, D L, Hansen, B R, Kratochvil, J A, and Quintana, M A. Dark current-voltage measurements on photovoltaic modules as a diagnostic or manufacturing tool. in *26th IEEE Photovoltaic Specialists Conference*. 1997. DOI: 10.1109/PVSC.1997.654286.
39. Pingel, S, Zemen, Y, Frank, O, Geipel, T, and Berghold, J, *Mechanical stability of solar cells within solar panels*, in *24th European Photovoltaic Solar Energy Conference*. 2009, WIP Wirtschaft und Infrastruktur GmbH & Co Planungs KG: Hamburg, Germany. p. 3459 - 3463.
40. Reil, F, Althaus, J, Vaassen, W, Herrmann, W, and Strohkendl, K. The Effect of Transportation Impacts and Dynamic Load Tests on the Mechanical and Electrical Behaviour of Crystalline PV Modules. in *25th European Photovoltaic Solar Energy Conference and Exhibition*. 2010. Valencia, Spain DOI: 10.4229/25thEUPVSEC2010-4AV.3.9.
41. Kajari-Schröder, S, Kunze, I, Eitner, U, and Köntges, M, Spatial and orientational distribution of cracks in crystalline photovoltaic modules generated by mechanical load tests. *Solar Energy Materials and Solar Cells*, 2011. **95**(11): p. 3054-3059 DOI: 10.1016/j.solmat.2011.06.032.
42. Sander, M, Dietrich, S, Pander, M, Schweizer, S, Ebert, M, and Bagdahn, J. Investigations on crack development and crack growth in embedded solar cells. in *Reliability of Photovoltaic Cells, Modules, Components, and Systems Conference*. 2011. San Diego, California DOI: 10.1117/12.893662.
43. Kajari-Schröder, S, Kunze, I, and Köntges, M, Criticality of cracks in PV modules. *Energy Procedia*, 2012. **27**: p. 658-663 DOI: 10.1016/j.egypro.2012.07.125.
44. Köntges, M, Kunze, I, Kajari-Schröder, S, Breitenmoser, X, and Bjørneklett, B, The risk of power loss in crystalline silicon based photovoltaic modules due to micro-cracks. *Solar Energy Materials and Solar Cells*, 2011. **95**(4): p. 1131-1137 DOI: 10.1016/j.solmat.2010.10.034.
45. Buerhop-Lutz, C, Schlegel, D, Vodermayer, C, and Nieß, M. Quality Control of PV-Modules in the Field Using Infrared-Thermography. in *26th European Photovoltaic Solar Energy Conference and Exhibition*. 2011. Hamburg, Germany DOI: 10.4229/26thEUPVSEC2011-5AO.5.2.
46. Köntges, M, Kajari-Schröder, S, Kunze, I, and Jahn, U. Crack Statistic of Crystalline Silicon Photovoltaic Modules. in *26th European Photovoltaic Solar Energy Conference and Exhibition*. 2011. Hamburg, Germany DOI: 10.4229/26thEUPVSEC2011-4EO.3.6.
47. Ebner, R, Zamini, S, and Újvári, G, *Defect analysis in different photovoltaic modules using electroluminescence (EL) and infrared (IR)-thermography*, in *25th European Photovoltaic Solar Energy Conference and Exhibition*. 2010, WIP Wirtschaft und Infrastruktur GmbH & Co Planungs KG: Valencia, Spain. p. 333 - 336.

48. van Mölken, J I, Yusufoğlu, U A, Safiei, A, Windgassen, H, Khandelwal, R, Pletzer, T M, and Kurz, H, Impact of Micro-Cracks on the Degradation of Solar Cell Performance Based On Two-Diode Model Parameters. *Energy Procedia*, 2012. **27**: p. 167-172 DOI: 10.1016/j.egypro.2012.07.046.
49. Breitenstein, O, Rakotoniaina, J P, Al Rifai, M H, and Werner, M, Shunt types in crystalline silicon solar cells. *Progress in Photovoltaics: Research and Applications*, 2004. **12**(7): p. 529-538 DOI: 10.1002/pip.544.
50. del Cueto, J A and McMahon, T J, Analysis of leakage currents in photovoltaic modules under high-voltage bias in the field. *Progress in Photovoltaics: Research and Applications*, 2002. **10**(1): p. 15-28 DOI: 10.1002/pip.401.
51. Swanson, R, Cudzinovic, M, DeCeuster, D, Desai, V, Jürgens, J, Kaminar, N, Mulligan, W, Rodrigues-Barbarosa, L, Rose, D, and Smith, D. The surface polarization effect in high-efficiency silicon solar cells. in *15th International Photovoltaic Science & Engineering Conference,*. 2005. Shanghai, China.
52. Pingel, S, Frank, O, Winkler, M, Daryan, S, Geipel, T, Hoehne, H, and Berghold, J. Potential induced degradation of solar cells and panels. in *35th IEEE Photovoltaic Specialists Conference*. 2010. Honolulu, Hawaii DOI: 10.1109/PVSC.2010.5616823.
53. Berghold, J, Koch, S, Böttcher, A, Ukar, A, Leers, M, and Grunow, P, *Potential-induced degradation (PID) and its correlation with experience in the field*, in *Photovoltaics International*. 2013, Solar Media Ltd.: London. p. 87-93.
54. Hacke, P, Kempe, M, Terwilliger, K, Glick, S, Call, N, Johnston, S, Kurtz, S, Bennett, I, and Kloos, M. Characterization of Multicrystalline Silicon Modules with System Bias Voltage Applied in Damp Heat. in *25th European Photovoltaic Solar Energy Conference and Exhibition*. 2010. Valencia, Spain DOI: 10.4229/25thEUPVSEC2010-4BO.9.6.
55. Schutze, M, Junghanel, M, Koentopp, M B, Cwikla, S, Friedrich, S, Muller, J W, and Wawer, P. Laboratory study of potential induced degradation of silicon photovoltaic modules. in *Photovoltaic Specialists Conference (PVSC), 2011 37th IEEE*. 2011. DOI: 10.1109/PVSC.2011.6186080.
56. Hacke, P, Terwilliger, K, Smith, R, Glick, S, Pankow, J, Kempe, M, Bennett, S K I, and Kloos, M, *System voltage potential-induced degradation mechanisms in PV modules and methods for test*, in *37th IEEE Photovoltaic Specialists Conference (PVSC)*. 2011. p. 000814-000820.
57. Hacke, P, Smith, R, Terwilliger, K, Perrin, G, Sekulic, B, and Kurtz, S, Development of an IEC test for crystalline silicon modules to qualify their resistance to system voltage stress. *Progress in Photovoltaics: Research and Applications*, 2014. **22**(7): p. 775-783 DOI: 10.1002/pip.2434.
58. Osterwald, C R, McMahon, T J, and del Cueto, J A, Electrochemical corrosion of SnO2:F transparent conducting layers in thin-film photovoltaic modules. *Solar Energy Materials and Solar Cells*, 2003. **79**(1): p. 21-33 DOI: 10.1016/S0927-0248(02)00363-X.
59. Hoffmann, S and Koehl, M, Effect of humidity and temperature on the potential-induced degradation. *Progress in Photovoltaics: Research and Applications*, 2014. **22**(2): p. 173-179 DOI: 10.1002/pip.2238.

60. Hacke, P, Smith, R, Terwilliger, K, Glick, S, Jordan, D, Johnston, S, Kempe, M, and Kurtz, S, Testing and Analysis for Lifetime Prediction of Crystalline Silicon PV Modules Undergoing Degradation by System Voltage Stress. *IEEE Journal of Photovoltaics*, 2013. **3**(1): p. 246-253 DOI: 10.1109/Jphotov.2012.2222351.
61. Lausch, D, Naumann, V, Breitenstein, O, Bauer, J, Graff, A, Bagdahn, J, and Hagendorf, C, Potential-Induced Degradation (PID): Introduction of a Novel Test Approach and Explanation of Increased Depletion Region Recombination. *Photovoltaics, IEEE Journal of*, 2014. **4**(3): p. 834-840 DOI: 10.1109/JPHOTOV.2014.2300238.
62. Mathiak, G, Schweiger, M, and Herrmann, W. Potential-Induced Degradation - Comparison of Different Test Methods and Low Irradiance Performance Measurements. in *27th European Photovoltaic Solar Energy Conference and Exhibition*. 2012. Frankfurt, Germany DOI: 10.4229/27thEUPVSEC2012-4DO.6.3.
63. AG, S S T, *SMA: Technical Information on PID*. Undated, SMA Solar Technology AG: Niestetal, Germany. p. 1-4. Report PID-TI-UEN113410.
64. Schwark, M, Berger, K, Ebner, R, Ujvari, G, Hirschl, C, Neumaier, L, and Muhleisen, W. Investigation of potential induced degradation (PID) of solar modules from different manufacturers. in *Industrial Electronics Society, IECON 2013 - 39th Annual Conference of the IEEE*. 2013. DOI: 10.1109/IECON.2013.6700486.
65. Kurtz, S, Wohlgemuth, J, Kempe, M, Bosco, N, Hacke, P, Jordan, D, Miller, D C, Silverman, T J, Phillips, N, and Earnest, T, *Photovoltaic Module Qualification Plus Testing*. 2013, National Renewable Energy Laboratory: Golden, Colorado, USA.
66. Commission, I E. *IEC/TS 62804 Ed. 1.0 Test methods for detection of potential-induced degradation of crystalline silicon photovoltaic (PV) modules*. 2014 [cited 2014 29 October]; Available from: http://www.iec.ch/.
67. Hacke, P, *Testing modules for potential-induced degradation–a status update of IEC 62804*, in *PV Module Reliability Workshop*. 2014, NREL: Golden, Colorado, USA.
68. Taubitz, C, Schutze, M, and Köntopp, M B, *Towards a Kinetic Model of Potential-Induced Shunting*, in *27th European Photovoltaic Solar Energy Conference and Exhibition*. 2012: Frankfurt, Germany. p. 3172 - 3176.
69. Lechner, P, Hummel, S, and Geyer, D. Test Method for a More Realistic Simulation of PID Field-Stress. in *29th European PV Solar Energy Conference and Exhibition*. 2014. Amsterdam, The Netherlands DOI: 10.4229/EUPVSEC20142014-5CO.14.3.
70. Hacke, P, Terwilliger, K, and Kurtz, S, *In-Situ Measurement of Crystalline Silicon Modules Undergoing Potential-Induced Degradation in Damp Heat Stress Testing for Estimation of Low-Light Power Performance*. 2013, National Renewable Energy Laboratory (NREL), Golden, CO. p. 1-10. Report NREL/TP-5200-60044, DOI: 10.2172/1090973.
71. Buerhop-Lutz, C and Scheuerpflug, H. Field Inspection of PV-Modules Using Aerial, Drone-Mounted Thermography. in *29th European Photovoltaic Solar*

Energy Conference and Exhibition. 2014. Amsterdam, The Netherlands DOI: 10.4229/EUPVSEC20142014-5BV.2.53.

72. Sera, D and Teodorescu, R. Robust series resistance estimation for diagnostics of photovoltaic modules. in *Industrial Electronics, 2009. IECON '09. 35th Annual Conference of IEEE*. 2009. DOI: 10.1109/IECON.2009.5415022.
73. De Soto, W, Klein, S A, and Beckman, W A, Improvement and validation of a model for photovoltaic array performance. *Solar Energy*, 2006. **80**(1): p. 78-88 DOI: 10.1016/j.solener.2005.06.010.
74. Stoicescu, L, Reuter, L, and Werner, J, *DaySy: Daylight Luminescence for PV Systems: How to Check 400kWpeak Per Day With Electroluminescence*, in *2014 Photovoltaic Module Reliability Workshop*. 2014: Golden, Colorado.
75. Commission, I E. *PNW/TS 82-901 Ed. 1.0 Photovoltaic devices - Part 13: Electroluminescence of photovoltaic modules (proposed future IEC TS 60904-13*. 2014 [cited 2014 29 October]; Available from: http://www.iec.ch/.
76. Tsai, D-M, Wu, S-C, and Li, W-C, Defect detection of solar cells in electroluminescence images using Fourier image reconstruction. *Solar Energy Materials and Solar Cells*, 2012. **99**: p. 250-262 DOI: 10.1016/j.solmat.2011.12.007.
77. Breitenstein, O, Khanna, A, Augarten, Y, Bauer, J, Wagner, J M, and Iwig, K, Quantitative evaluation of electroluminescence images of solar cells. *physica status solidi (RRL) – Rapid Research Letters*, 2010. **4**(1-2): p. 7-9 DOI: 10.1002/pssr.200903304.
78. Anwar, S and Abdullah, M, Micro-crack detection of multicrystalline solar cells featuring an improved anisotropic diffusion filter and image segmentation technique. *EURASIP Journal on Image and Video Processing*, 2014. **2014**(1): p. 1-17 DOI: 10.1186/1687-5281-2014-15.
79. Spataru, S, Sera, D, Kerekes, T, and Teodorescu, T, *Photovoltaic Array Condition Monitoring Based on Online Regression of Performance Model*, in *39th IEEE Photovoltaic Specialists Conference* 2013, IEEE: Tampa, Florida. p. 0815 - 0820.
80. Gokmen, N, Karatepe, E, Celik, B, and Silvestre, S, Simple diagnostic approach for determining of faulted PV modules in string based PV arrays. *Solar Energy*, 2012. **86**(11): p. 3364-3377 DOI: 10.1016/j.solener.2012.09.007.
81. Silvestre, S, Chouder, A, and Karatepe, E, Automatic fault detection in grid connected PV systems. *Solar Energy*, 2013. **94**: p. 119-127 DOI: 10.1016/j.solener.2013.05.001.
82. Chouder, A and Silvestre, S, Automatic supervision and fault detection of PV systems based on power losses analysis. *Energy Conversion and Management*, 2010. **51**(10): p. 1929-1937 DOI: 10.1016/j.enconman.2010.02.025.
83. Forero, N, Hernandez, J, and Gordillo, G, Development of a monitoring system for a PV solar plant. *Energy Conversion and Management*, 2006. **47**(15-16): p. 2329-2336 DOI: 10.1016/j.enconman.2005.11.012.
84. Kohno, T, Fujimori, M, Osabe, T, Shimada, H, Morikawa, K, and Miyazaki, S T N. Experimental Verification of Fault-Diagnosis Architecture in a Large-Scale Photovoltaic Power Plant. in *28th European Photovoltaic Solar Energy*

Conference and Exhibition. 2013. Paris, France DOI: 10.4229/28thEUPVSEC2013-5CO.6.4.

85. Byung-Kwan, K, Seung-Tak, K, Sun-Ho, B, and Jung-Wook, P, Diagnosis of Output Power Lowering in a PV Array by Using the Kalman-Filter Algorithm. *Energy Conversion, IEEE Transactions on*, 2012. **27**(4): p. 885-894 DOI: 10.1109/TEC.2012.2217144.
86. Ducange, P, Fazzolari, M, Lazzerini, B, and Marcelloni, F. An intelligent system for detecting faults in photovoltaic fields. in *11th International Conference on Intelligent Systems Design and Applications (ISDA)*. 2011. Cordoba DOI: 10.1109/ISDA.2011.6121846.
87. Vergura, S, Acciani, G, Amoruso, V, Patrono, G E, and Vacca, F, Descriptive and Inferential Statistics for Supervising and Monitoring the Operation of PV Plants. *IEEE Transactions on Industrial Electronics*, 2009. **56**(11): p. 4456-4464 DOI: 10.1109/tie.2008.927404.
88. Takashima, T, Yamaguchi, J, and Ishida, M. Fault detection by signal response in PV module strings. in *33rd IEEE Photovoltaic Specialists Conference*. 2008. DOI: 10.1109/PVSC.2008.4922843.
89. Johnson, J, Kuszmaul, S, Bower, W, and Schoenwald, D. Using PV Module and Line Frequency Response Data to Create Robust Arc Fault Detectors. in *26th European Photovoltaic Solar Energy Conference and Exhibition*. 2011. Hamburg, Germany DOI: 10.4229/26thEUPVSEC2011-4AV.3.24.
90. Sera, D, Teodorescu, R, and Rodriguez, P. Photovoltaic module diagnostics by series resistance monitoring and temperature and rated power estimation. in *34th Annual Conference of IEEE Industrial Electronics (IECON)*. 2008. DOI: 10.1109/IECON.2008.4758297.
91. Tina, G P, Cosentino, F, and Ventura, F, *Monitoring and diagnostics of photovoltaic power plants*, in *World Renewable Energy Congress*. 2014: London, United Kingdom.
92. Miwa, M, Yamanaka, S, Kawamura, H, Ohno, H, and Kawamura, H. Diagnosis of a Power Output Lowering of PV Array with a (-dI/dV)-V Characteristic. in *4th IEEE World Conference on Photovoltaic Energy Conversion*. 2006. Waikoloa DOI: 10.1109/WCPEC.2006.279703.
93. Kjær, S B, Oprea, O, and Borup, U, *Adaptive Sweep for PV Applications*, in *26th European Photovoltaic Solar Energy Conference and Exhibition*. 2011: Hamburg, Germany. p. 3708 - 3710.
94. Decker, B and Jahn, U, Performance of 170 grid connected PV plants in Northern Germany—Analysis of yields and optimization potentials. *Solar Energy*, 1997. **59**(4–6): p. 127-133 DOI: 10.1016/S0038-092X(96)00132-6.
95. Hohm, D P and Ropp, M E, Comparative study of Maximum Power Point Tracking algorithms using an experimental, programmable, maximum power point tracking test bed, in *Conference Record of the Twenty-Eighth IEEE Photovoltaic Specialists Conference - 2000*. 2000, IEEE: New York. p. 1699-1702.
96. Hussein, K H, Muta, I, Hoshino, T, and Osakada, M, Maximum Photovoltaic Power Tracking - an Algorithm for Rapidly Changing Atmospheric

Conditions. *IEE Proceedings-Generation Transmission and Distribution*, 1995. **142**(1): p. 59-64 DOI: 10.1049/ip-gtd:19951577.

97. Esram, T and Chapman, P L, Comparison of photovoltaic array maximum power point tracking techniques. *IEEE Transactions on Energy Conversion*, 2007. **22**(2): p. 439-449 DOI: 10.1109/tec.2006.874230.

98. Kobayashi, K, Takano, I, and Sawada, Y, A study of a two stage maximum power point tracking control of a photovoltaic system under partially shaded insolation conditions. *Solar Energy Materials and Solar Cells*, 2006. **90**(18–19): p. 2975-2988 DOI: 10.1016/j.solmat.2006.06.050.

99. Patel, H and Agarwal, V, Maximum Power Point Tracking Scheme for PV Systems Operating Under Partially Shaded Conditions. *Industrial Electronics, IEEE Transactions on*, 2008. **55**(4): p. 1689-1698 DOI: 10.1109/TIE.2008.917118.

100. Young-Hyok, J, Doo-Yong, J, Jun-Gu, K, Jae-Hyung, K, Tae-Won, L, and Chung-Yuen, W, A Real Maximum Power Point Tracking Method for Mismatching Compensation in PV Array Under Partially Shaded Conditions. *Power Electronics, IEEE Transactions on*, 2011. **26**(4): p. 1001-1009 DOI: 10.1109/TPEL.2010.2089537.

101. Hishikawa, Y, Imura, Y, and Oshiro, T. Irradiance-dependence and translation of the I-V characteristics of crystalline silicon solar cells. in *28th IEEE Photovoltaic Specialists Conference*. 2000. Anchorage, Alaska DOI: 10.1109/PVSC.2000.916169.

102. Lindholm, F A, Fossum, J G, and Burgess, E L, Application of the superposition principle to solar-cell analysis. *IEEE Transactions on Electron Devices*, 1979. **26**(3): p. 165-171 DOI: 10.1109/T-ED.1979.19400.

103. Wolf, M and Rauschenbach, H, Series resistance effects on solar cell measurements. *Advanced Energy Conversion*, 1963. **3**(2): p. 455-479 DOI: 10.1016/0365-1789(63)90063-8.

104. Robinson, S J, Aberle, A G, and Green, M A, Departures from the principle of superposition in silicon solar cells. *Journal of Applied Physics*, 1994. **76**(12): p. 7920-7930 DOI: 10.1063/1.357902.

105. Robinson, S J, Wenham, S R, Altermatt, P P, Aberle, A G, Heiser, G, and Green, M A, Recombination rate saturation mechanisms at oxidized surfaces of high-efficiency silicon solar cells. *Journal of Applied Physics*, 1995. **78**(7): p. 4740-4754 DOI: 10.1063/1.359821.

106. Tarr, N G and Pulfrey, D L, An investigation of dark current and photocurrent superposition in photovoltaic devices. *Solid-State Electronics*, 1979. **22**(3): p. 265-270 DOI: 10.1016/0038-1101(79)90032-7.

107. Nagel, H, Metz, A, and Wangemann, K. Crystalline Si solar cells and modules featuring excellent stability against potential-induced degradation. in *26th European Photovoltaic Solar Energy Conference and Exhibition*. 2011. Hamburg, Germany DOI: 10.4229/26thEUPVSEC2011-4CO.5.6.

108. Nelson, W, Accelerated Degradation, in *Accelerated Testing*. 2008, John Wiley & Sons, Inc. p. 521-548.

109. Hacke, P, Smith, R, Terwilliger, K, Glick, S, Jordan, D, Johnston, S, Kempe, M, and Kurtz, S. Acceleration factor determination for potential-induced

degradation in crystalline silicon PV modules. in *2013 IEEE International Reliability Physics Symposium (IRPS)*. 2013. Monterey, California DOI: 10.1109/IRPS.2013.6532009.

110. Escobar, L A and Meeker, W Q, A review of accelerated test models. *Statistical Science*, 2006. **21**(4): p. 552-577 DOI: 10.1214/088342306000000321.
111. Meeker, W Q and Escobar, L A, *Accelerated test models*. Statistical methods for reliability data. John Wiley & Sons: New York, 1998.
112. Aberle, A G, Wenham, S R, and Green, M A. A new method for accurate measurements of the lumped series resistance of solar cells. in *23rd IEEE Photovoltaic Specialists Conference*. 1993. Louisville, Kentucky DOI: 10.1109/PVSC.1993.347065.
113. Werner, J, Schottky barrier and pn-junctionI/V plots — Small signal evaluation. *Applied Physics A*, 1988. **47**(3): p. 291-300 DOI: 10.1007/BF00615935.
114. Otsu, N, A Threshold Selection Method from Gray-Level Histograms. *Systems, Man and Cybernetics, IEEE Transactions on*, 1979. **9**(1): p. 62-66 DOI: 10.1109/TSMC.1979.4310076.
115. Shapiro, L G and Stockman, G C, *Computer Vision*. Prentice Hall, 2001.
116. Fuyuki, T and Kitiyanan, A, Photographic diagnosis of crystalline silicon solar cells utilizing electroluminescence. *Applied Physics A*, 2009. **96**(1): p. 189-196 DOI: 10.1007/s00339-008-4986-0.
117. King, D L, Boyson, W E, and Kratochvil, J A, *Photovoltaic Array Performance Model*. 2004, Sandia National Laboratories: Albuquerque, New Mexico 87185-0752.
118. Fanney, A H, Davis, M W, Dougherty, B P, King, D L, Boyson, W E, and Kratochvil, J A, Comparison of photovoltaic module performance measurements. *Journal of Solar Energy Engineering*, 2006. **128**(2): p. 152-159 DOI: 10.1115/1.2192559.
119. Hansen, C W, Riley, D M, and Jaramillo, M. Calibration of the Sandia Array Performance Model using indoor measurements. in *Photovoltaic Specialists Conference (PVSC), 2012 38th IEEE*. 2012. DOI: 10.1109/PVSC.2012.6318229.
120. Kuncheva, L I, How good are fuzzy If-Then classifiers? *Systems, Man, and Cybernetics, Part B: Cybernetics, IEEE Transactions on*, 2000. **30**(4): p. 501-509 DOI: 10.1109/3477.865167.
121. Abe, S, Thawonmas, R, and Kayama, M, A fuzzy classifier with ellipsoidal regions for diagnosis problems. *Systems, Man, and Cybernetics, Part C: Applications and Reviews, IEEE Transactions on*, 1999. **29**(1): p. 140-148 DOI: 10.1109/5326.740676.
122. Fawcett, T, An introduction to ROC analysis. *Pattern Recognition Letters*, 2006. **27**(8): p. 861-874 DOI: 10.1016/j.patrec.2005.10.010.

APPENDIX A

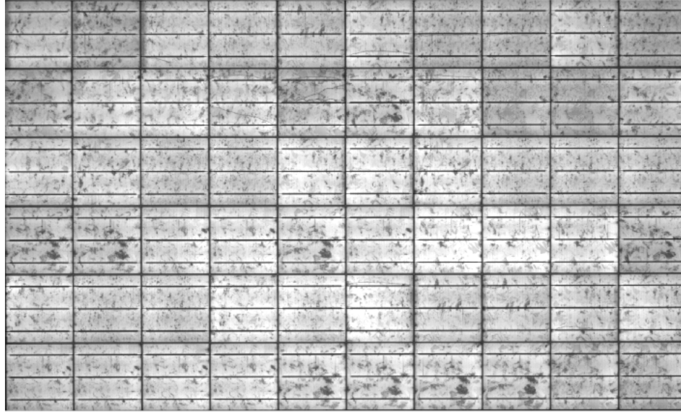

Figure A.1: Electroluminescence image of a crystalline silicon PV module measured at STC I_{mp} bias, taken before the module has sustained any mechanical damage.

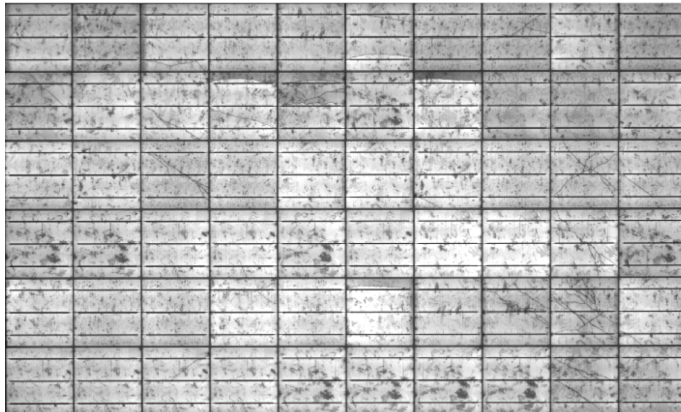

Figure A.2: Electroluminescence image of a crystalline silicon PV module measured at STC I_{mp} bias, taken after the first round of mechanical damage. The module's STC P_{max} degraded down to 99.7% of the initial value.

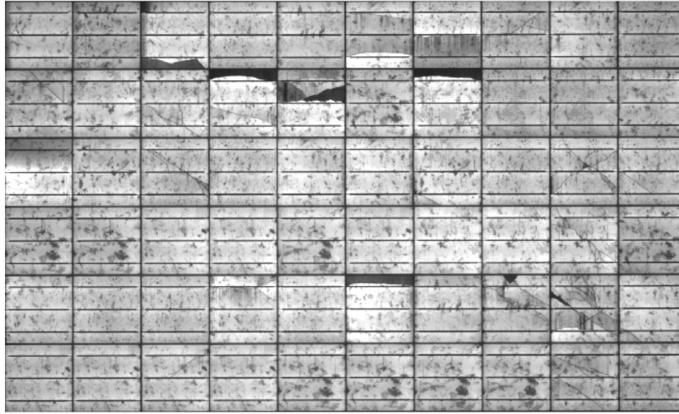

Figure A.3: Electroluminescence image of a crystalline silicon PV module measured at STC I_{mp} bias, taken after the second round of mechanical damage. The module's STC P_{max} degraded down to 96.8% of the initial value.

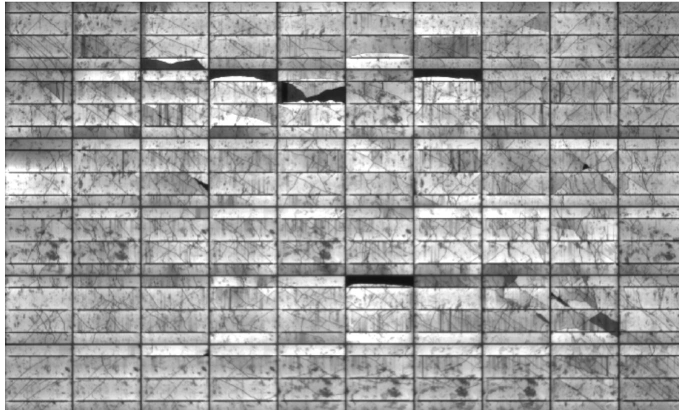

Figure A.4: Electroluminescence image of a crystalline silicon PV module measured at STC I_{mp} bias, taken after the fourth round of mechanical damage. The module's STC P_{max} degraded down to 93.7% of the initial value.

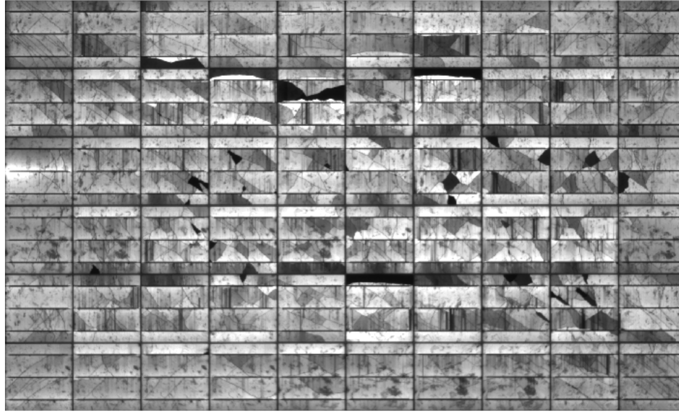

Figure A.5: Electroluminescence image of a crystalline silicon PV module measured at STC I_{mp} bias, taken after the final round of mechanical damage. The module's STC P_{max} degraded down to 89.6% of the initial value.

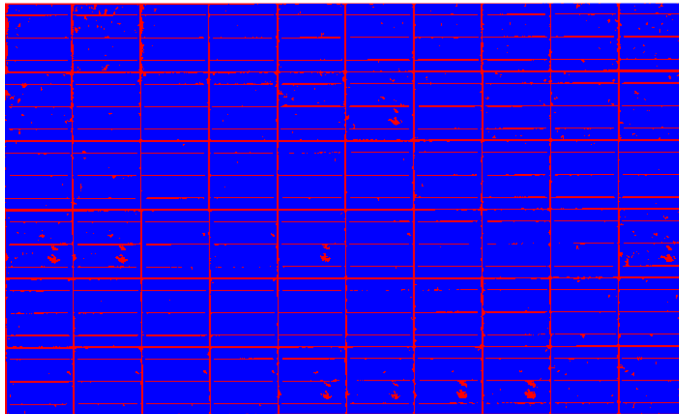

Figure A.6: Module map of active (blue - 89.4%) and inactive (red – 10.6%) areas, calculated by thresholding (at 0.34 ELI) the electroluminescence image of the PV module, taken before the module has sustained any mechanical damage.

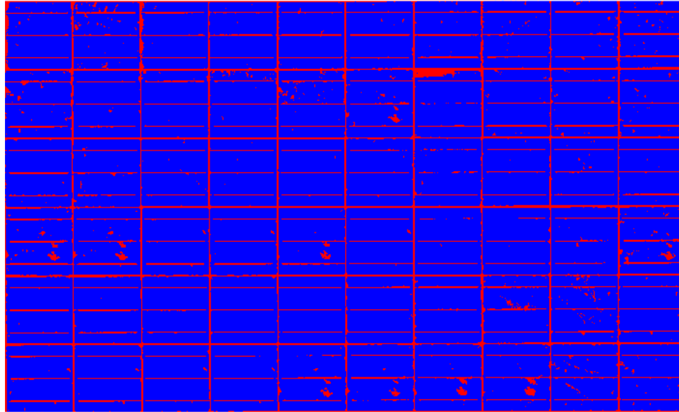

Figure A.7: Module map of active (blue - 89%) and inactive (red – 11%) areas, calculated by thresholding (at 0.34 ELI) the electroluminescence image of the PV module, taken after the first round of mechanical damage (STC P_{max}=99.7% of the initial value).

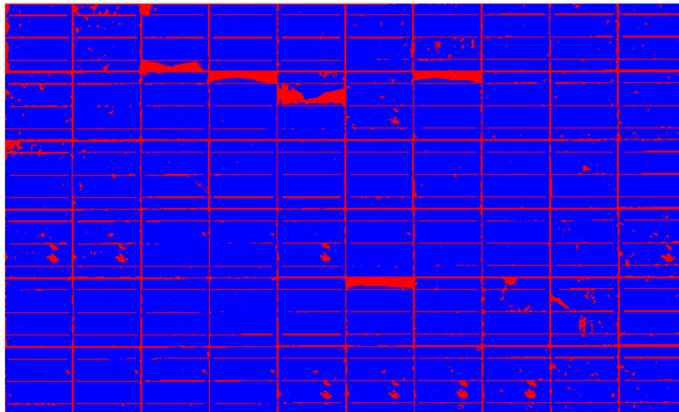

Figure A.8: Module map of active (blue - 88.1%) and inactive (red – 11.9%) areas, calculated by thresholding (at 0.34 ELI) the electroluminescence image of the PV module, taken after the second round of mechanical damage (STC P_{max}=96.8% of the initial value).

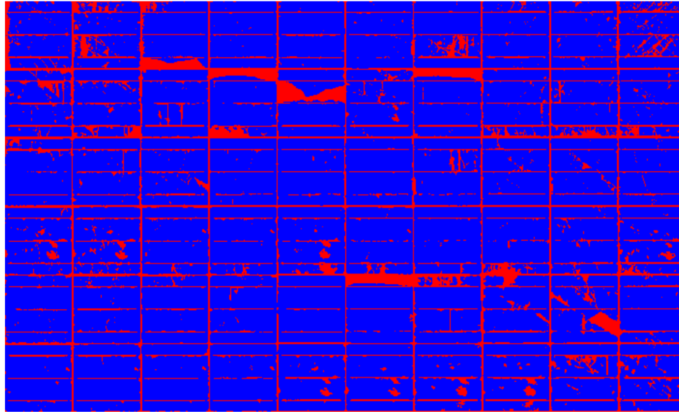

Figure A.9: Module map of active (blue - 84.8%) and inactive (red – 15.2%) areas, calculated by thresholding (at 0.34 ELI) the electroluminescence image of the PV module, taken after the third round of mechanical damage (STC P_{max}=93.7% of the initial value).

APPENDIX B

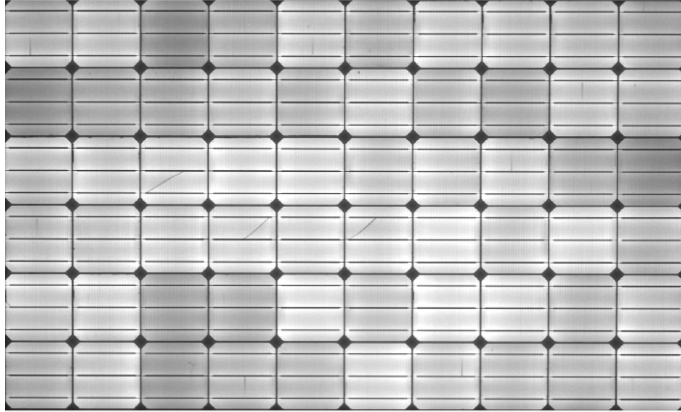

Figure B.1: Electroluminescence image of a crystalline silicon PV module measured at STC I_{mp} bias, taken before the module has sustained PID.

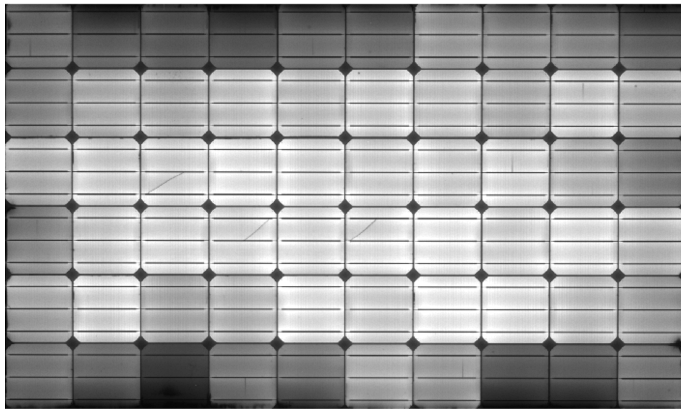

Figure B.2: Electroluminescence image of a crystalline silicon PV module measured at STC I_{mp} bias, taken after the modules sustained PID and its STC P_{max} degraded down to 76.8% of the initial value.

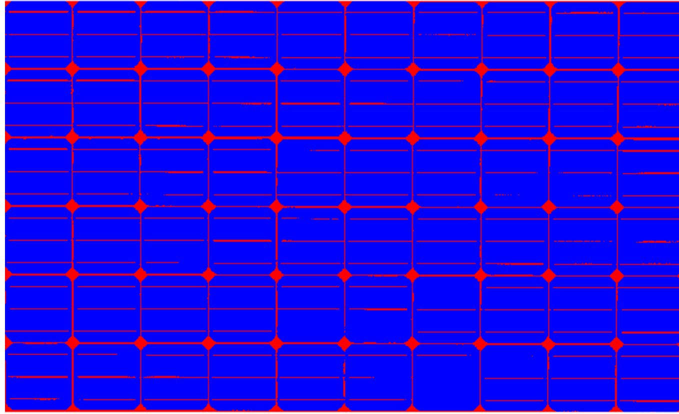

Figure B.3: Module map of active (blue – 89.8%) and inactive (red – 10.2%) areas, calculated by thresholding (at 0.3 ELI) the electroluminescence image of the PV module, taken before the module has sustained any PID.

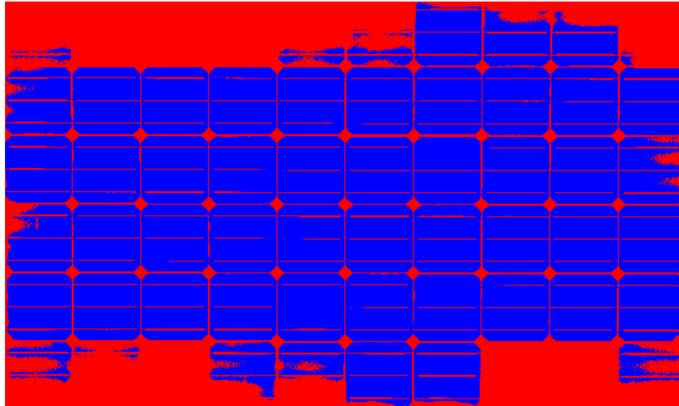

Figure B.4: Module map of active (blue - 68.7%) and inactive (red – 31.3%) areas, calculated by thresholding (at 0.3 ELI) the electroluminescence image of the PV module, taken after the module has sustained PID (STC P_{max}=76.8% of the initial value).

APPENDIX C

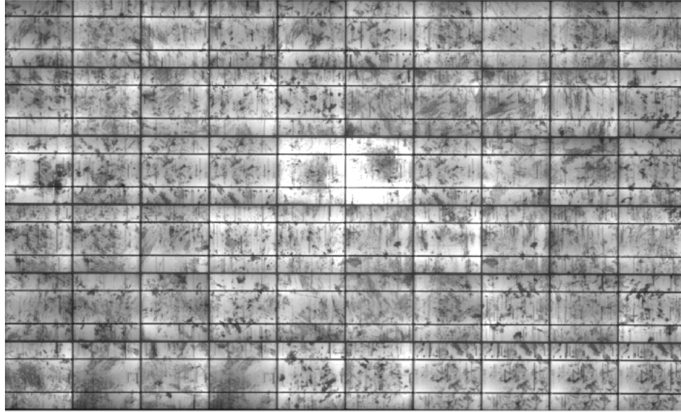

Figure C.1: Electroluminescence image of a multicrystalline silicon PV module measured at STC I_{mp} bias, taken before the module has sustained damage to its cell interconnects

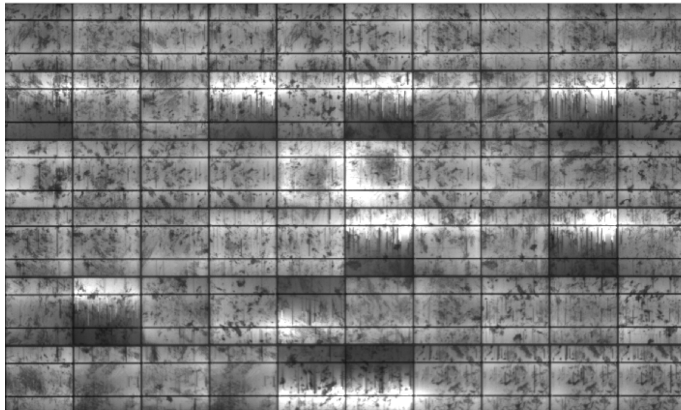

Figure C.2: Electroluminescence image of a multicrystalline silicon PV module measured at STC I_{mp} bias, taken after the modules sustained damage to its cell interconnects, and its STC P_{max} degraded down to 96.9% of the initial value.

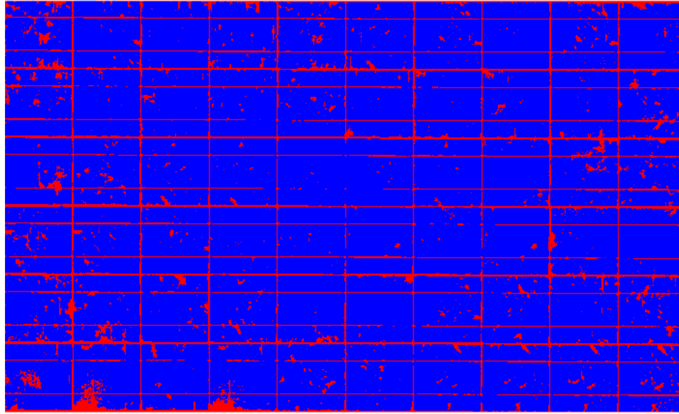

Figure C.3: Module map of active (blue – 88.4%) and inactive (red – 11.6%) areas, calculated by thresholding (at 0.24 ELI) the electroluminescence image of the PV module, taken before the module has sustained any damage.

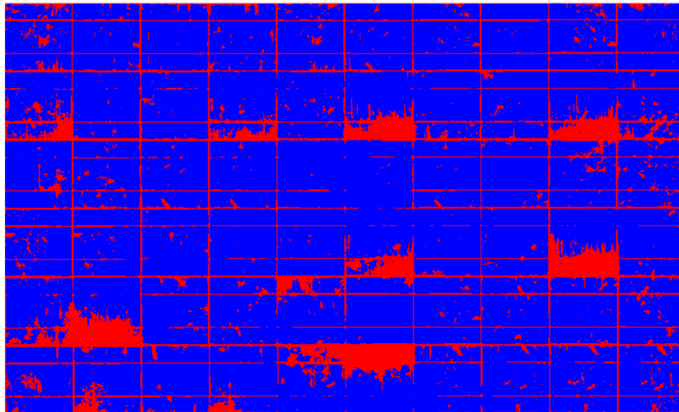

Figure C.4: Module map of active (blue – 84.4%) and inactive (red – 15.6%) areas, calculated by thresholding (at 0.24 ELI) the electroluminescence image of the PV module, taken after the module has sustained damage to its cell interconnects (STC P_{max}=76.8% of the initial value).